Transmission scattering interferometry : from label-free virus detection and affinity measurements to sub-cellular tomography

Samer Alhaddad

To cite this version:

Samer Alhaddad. Transmission scattering interferometry : from label-free virus detection and affinity measurements to sub-cellular tomography. Optics [physics.optics]. Université Paris sciences et lettres, 2022. English. NNT : 2022UPSLS034 . tel-03982658

HAL Id: tel-03982658
https://pastel.hal.science/tel-03982658

Submitted on 10 Feb 2023

PSL
UNIVERSITÉ PARIS

THÈSE DE DOCTORAT
DE L'UNIVERSITÉ PSL

Préparée à l'ESPCI Paris

Transmission scattering interferometry: from label-free virus detection and affinity measurements to sub-cellular tomography

Interférométrie de diffusion par transmission : de la détection de virus sans marquage et mesures d'affinité à la tomographie sub-cellulaire

Composition du jury :

Florence GAZEAU	
Directrice de recherche CNRS, Université Paris Cité, LMSC, Paris	*Présidente du jury*
François MARQUIER	
Professeur, ENS Paris-Saclay,LuMIn, Gif-sur-Yvette	*Rapporteur*
Cyril FAVARD	
Ingénieur de recherche CNRS, IRIM, Montpellier	*Rapporteur*
Pascale BOULANGER	
Directrice de recherche CNRS, I2BC, Gif-sur-Yvette	*Examinatrice*
Vincent CROQUETTE	
Professeur ENS, LPENS, Paris	*Examinateur*
Gilles RUBINSTENN	
Fondateur et CEO ReST Therapeutics, ReST Therapeutics, Montpellier	*Examinateur*
Samuel GRESILLON	
Maître de conférences Sorbonne Université, Institut Langevin, Paris	*Directeur de thèse*
Ignacio IZEDDIN	
Maître de conférences ESPCI, Institut Langevin, Paris	*Co-directeur de thèse*
Claude BOCCARA	
Professeur ESPCI, Institut Langevin, Paris	*Co-directeur de thèse*
Martine BOCCARA	
Professeure ENS, MNHN, Paris	*Co-encadrante de thèse*

Préparée par
Samer ALHADDAD
Le 02/06/2022

École doctorale n°564
Physique en Île-de-France

Spécialité
Physique

ESPCI PARIS | PSL

Acknowledgement

For the PhD journey, I was really fortunate to be surrounded by very supportive people and I would like to express my sincere appreciation and gratitude to accomplish this thesis. This thesis would not have been possible without the help of my supervisors Ignacio, Martine and Claude.

I am deeply grateful to Claude for your incessant help, support and spending so much time discussing my questions and results. I enjoyed every moment of our nearly every morning discussions, these discussions were enormously motivational for me, I definitely learned a lot in science and more importantly I learned how to tackle problems in different ways to make it simpler. Your scientific intuition is very inspirational in addition to your human side. I am deeply grateful to you Martine for your involvement during these three years. You always had new biological questions and new samples to image. I admired your motivation for new ideas and new biological questions. I lost count on the number of times you read the preprint manuscript of antibodies-viruses interaction and I am really glad. I am really thankful to you Ignacio for your advices and discussions especially in single particle tracking analysis. Thanks for your rigorous observations for the presentation of my work during these three years.

I would like to express my appreciation to my honorable jury members for their valuable time to review my thesis and participate in the thesis defense. I would like to thank especially Francois Marquier and Cyril Favard for their invaluable suggestions and comments.

I would like to express my gratitude to the director of the Institute Arnaud Tourin for welcoming me for the last few years. I am also grateful to the support team at the institute, I appreciate your help with never ending paper work and technical support.

I would like to deeply thank Olivier, I am glad for your help in different approaches of my project. I am especially grateful for your support and encouragement all these years. I learned a lot from your expertise. You always have new ideas, I especially admire your collaborative and team-work approach. I also would like to thank Clement for your help and for answering my late hour questions, I really enjoyed our discussions. Slava, your motivation is very inspirational, I enjoyed every step of our ‘fast and dirty’ approach to build the ‘ultimate eye diagnosis set-up’. With Yao, we shared lots of laughs. Good luck with your project Yao, I can’t wait till your defense. I would like to thank the members of the OCT team for the fruitful discussions and great ambiance. I would like also to thank my officemates Cecile and Camilo, we supported each other’s and shared a lot of memories and candies during the past three years. Many thanks to for my new officemates who welcomed me the last few months in a great atmosphere, Loubnan, Max, Clement, Sylvio, Louise, Romain, Julia, Eve, Zofia and Mateo.

These three years in the lab wouldn’t have been the same without the support of Patricia, Jad, Anwesh, Ghuyu, Siyu, Houda, Dimitri, Jana, Samuel, Hussam and Ines. I would like to thank all the members of Institut Langevin, you were always very supportive, ready to help and share your ideas. I would like to thank my friends for their continuous support and cheering me up in hard moments despite not understanding what I was doing.

I am grateful to my family, my parents especially for their encouragement me despite the distance, my brother Maher and sister Hanady for being always supportive in the worst and best moments during these years. Last, Ghewa you were present in every step of this work, you celebrated my small achievements and cheered me up in my worst moments, I am glad you are here.

Contents

General introduction

One of the primary objectives of microscopy is to visualize small structures and follow their dynamics at small-length scales. Many researchers and groups have put their efforts into developing and optimizing new microscopy techniques to reveal the morphology and understand biological behavior. The popularity of light microscopy increased progressively due to its noninvasive nature, the potential for high throughput, and relatively simple integration with other technologies. However, these capabilities come at the expense of low sensitivity and resolution compared to other methods such as electron microscopy and atomic force microscopy techniques.

Arguably, light microscopy reached its limit of sensitivity more than 30 years ago with the detection of individual ions, and molecules using absorption and fluorescence signals as contrast mechanisms [1, 2]. These experiments have been conducted at a cryogenic temperature to maximize the interaction between light and particle of interest. In fact, the main advantage of fluorescence methods is the ability to detect particles of interest only and reject light scattered from the background. In linear microscopy, light emitted from the fluorescent label has a longer wavelength than the excitation one, allowing light collection from the labeled target molecule only. Moreover, this field kept improving simultaneously with the emergence of switchable fluorescent labels to reach spatial resolution approaching the molecular scale using super-resolution microscopy techniques [3, 4]. The advent of single-molecule approaches has brought about a revolution in the last few decades across life sciences and condensed matter physics due to the ability to investigate phenomena at the molecular scale that are hidden by ensemble-averaging. Nowadays, single-molecule fluorescence has become a standard tool to follow heterogeneous systems' dynamics.

At the same time, the use of fluorescent contrast limits the applicability of the most sensitive studies to species that are either highly fluorescent themselves or are made fluorescent by the introduction of external tags, which demands a specific manipulation by the user. In addition, photochemical and photophysical processes limit signal intensities and the degree to which quantitative signals are critical. These limitations have driven the development of label-free microscopy methods. The concept of separating illumination from detection was first reported at the beginning of the 20th century. This concept is known as darkfield microscopy methods. Originated from phase-contrast microscopy developed by Zernike in1935, many groups have developed techniques that use interference to amplify scattered or absorbed signals of interest. These techniques' primary advantage is their universal applicability for every sample having a slight refractive index difference compared to its surrounding refractive index. Therefore, interferometric microscopy techniques are a particularly attractive field for developing label-free methods adapted for detecting molecules and monitoring reactions on a cellular level [5]. All microscopists share similar concerns, mainly limitations due to the numerical aperture, shot noise level, aberrations, multiple scattering perturbations, etc. All these degrade the image quality; so many groups tackled these problems and developed new innovative ways to overcome these limitations and to retrieve the information needed with a higher quality of images. Different label-free microscopy approaches are currently being developed and studied at Langevin Institute. The common goal of these techniques is to retrieve high-quality images directly or by enhancing the image quality in post-processing, e.g., using matrix approaches or by reconstructing the beam at different depths using holography. Among these approaches, Full-Field Optical Coherence Tomography proved its potential in optical sectioning in thick biological samples with a cellular resolution. These techniques are currently used to study fixed, ex vivo, and in vivo samples.

In this manuscript, our aim is to improve and broaden the field of an interferometric label-free method to detect nanoparticles such as virus in liquids as well as to introduce a new tomographic approach for investigating the structure and dynamics of biological samples.

More precisely, this manuscript is divided into five chapters.

The first chapter presents a few methods of detecting nanoobjects known as "Label-free." We present the advantages of the use of interferometric scattering microscopy and compare it to darkfield and fluorescence methods. Then we describe the state of the art of different configurations of interferometric microscopy setups working in transmission, reflection, and other configurations. We mention the differences between the uses of distinct kinds of light sources (coherent/ incoherent light). At the end of this chapter, we discuss the limitations and challenges of interferometric scattering microscopy approaches along with the recent performances when studying biological samples.

The second chapter introduces the optical setup that I have used to study the diffusion of small nanoparticles in liquid solution. It is a simple arrangement in which a high-power LED light source is employed to illuminate the sample solution containing the nanoparticles of interest in a transmission configuration. We have detected and tracked single particles with such a simple setup by adapting a single particle tracking (SPT) algorithm developed initially for fluorescence application. Therefore, using SPT algorithms, we have been able to detect and track the movement of small particles in solution (SiO_2 of 50nm in diameter). Here, when using calibrated nanobeads of different sizes, we measured the dependency of the interferometric signal and the estimated diffusion coefficients of the nanoparticles of interest, depending on the size of the particles. Appendix A describes a new setup that enabled us to validate by fluorescent labeling the results obtained with an interferometric setup (article submitted for publication).

The third chapter gathers the results when imaging single viruses in aquatic solutions using the optical setup, tracking algorithm, and analysis presented in the second chapter. We have studied different types of viruses, bacteriophages, and enveloped mammal viruses ranging between 60 and 200nm. First, we are interested in the diffusivity characteristics of these viruses. Next, by analyzing the interferometric signal and the diffusion properties of the particles, we distinguish between two different populations of viruses having similar sizes but with different internal structures (full and empty capsids of T5). In the final part of this chapter, we were interested in studying interactions between viruses and specific antibodies. We simply added antibodies to the sample solution containing the viruses, and we monitored the interaction signature to modify the interferometric signal and diffusion properties. We went a step further and used a new approach to estimate an equilibrium association constant attributed to the affinity of antibodies on the one hand, and we can estimate the rate equation of the reaction. This approach has also been used with non-purified serum-containing different types of antibodies in the solutions.

The fourth chapter gathers experimental data, a simple numerical simulation in the near field and a naïve analytical model of the interferometric signal. We have surprisingly found that the interferometric signal is not limited by the numerical aperture (NA) of the objective lens in use. We, therefore, compare the interferometric signal when varying the numerical aperture. These measurements show that the NA is not fully utilized (as in fluorescence); we explain this phenomenon by a simple theoretical model involving the destructive interference due to the Gouy phase shift and that associated with the curvature of the wave when we move away from focus. In addition, with FDTD simulations, we investigated the perturbation of the electric field in the near field. The second part of this chapter aims to detect smaller viruses. Since the intensity delivered by the LED limits us from increasing the interferometric contrast, we introduce a laser illumination to attenuate the illumination beam in the back focal plane of the objective lens. The challenge of using LASER sources is the unwanted noise caused by speckle interferences. We added a high-frequency (higher than 1 MHz) deformable membrane mirror to a square optical fiber to homogenize the incident beam. This illumination approach allows for attenuating the reference beam, increasing the interferometric contrast and therefore detecting smaller viruses (MS2, AAV) in a wide-field illumination.

In the fifth and last chapter, we explore a new promising method of full-field interferometric microscopy operating by transmission to image solid or semi-solid objects and revealing both the structures of the objects observed and the intracellular dynamics. The method consists of using the Gouy phase shift near the focus to acquire two phase-shifted images and, therefore, by subtracting these two images. In other words, we can reject the out-of-focus background to easily obtain optical sectioning. This method has been used to obtain tomographic images of environmental samples such as algae, corneas grafts, and cells as well as to study the internal dynamics of cells. Not to mention that we could investigate the internal dynamics of living cells.

The last part of the manuscript consists of a general conclusion and presents this work's perspectives.

Bibliography

[1] William E Moerner and Lothar Kador. Optical detection and spectroscopy of single molecules in a solid. *Physical review letters*, 62(21):2535, 1989. 1

[2] Michel Orrit and J Bernard. Single pentacene molecules detected by fluorescence excitation in a p-terphenyl crystal. *Physical review letters*, 65(21):2716, 1990. 1

[3] Robert M Dickson, Andrew B Cubitt, Roger Y Tsien, and William E Moerner. On/off blinking and switching behaviour of single molecules of green fluorescent protein. *Nature*, 388(6640):355–358, 1997. 1

[4] Klaus C Gwosch, Jasmin K Pape, Francisco Balzarotti, Philipp Hoess, Jan Ellenberg, Jonas Ries, and Stefan W Hell. Minflux nanoscopy delivers 3d multicolor nanometer resolution in cells. *Nature methods*, 17(2):217–224, 2020. 1

[5] Lee Priest, Jack S Peters, and Philipp Kukura. Scattering-based light microscopy: From metal nanoparticles to single proteins. *Chemical Reviews*, 121(19):11937–11970, 2021. 2

Chapter 1

From nanoparticle detection to label-free optical microscopy

Contents

1.1 Extinction term and cross section

The primary objective of microscopy is to visualize structures and spatial and temporal dynamics at small length scales by revealing the optical properties of macro molecules, cells, small organisms, tissue and more generally natural and artificial materials. The use of visible light illumination microscopy has a particular interest because it is usually noninvasive. Moreover, the non-invasiveness approach makes optical microscopy appealing to study ex-vivo or in-vivo biological samples. However, the resolution of any far-field optical system is still mainly limited by the achievable numerical aperture of the imaging system in terms of resolution. While for the sensitivity of label-free optical systems, it results from the optical properties and size of the sample as well as the illumination properties of the incident beam. When visualizing ultimate small features, three main challenges appear: resolution, specificity, and sensitivity. In this chapter, we are mainly interested in describing the sensitivity of label-free optical detections of subwavelength samples. The sensitivity of a label-free optical system is defined by its ability to detect an optical signal and the capability of distinguishing signals from the background noise. In other words, the mechanism that induces the contrast in imaging microscopy. In label-free microscopy, it is based on the extinction measurements of the specimen, which combine absorption and the scattering cross section of a specimen. Using the Optical Theorem definition, the energy taken out of a plane wave with a well-defined wave vector k is either due to absorption, transfer of energy to other channels, or scattering into other k-vectors.

Light-matter interaction can be described by elastic and inelastic interaction. Light scattering models can be divided into three different regimes when using visible optical microscopy to study biological specimens: Rayleigh, Mie, and Geometric scattering regimes. The distinction between these three regimes depends mainly on the size of the particle of interest. Models of light scattering can be divided into three domains based on a dimensionless size parameter, α :

$$\alpha = \pi D_p / \lambda \tag{1.1}$$

where πD_p is the circumference of a particle and λ represents the wavelength of incident light beam in the medium. Based on the value of α, three domains can be distinguished:

$\alpha << 1$: Rayleigh scattering (small particles compared to the illumination wavelength)
$\alpha \approx 1$: Mie scattering (spherical particles compared in size to the wavelength)
$\alpha >> 1$: geometric scattering (particles much bigger than the wavelength)

Rayleigh regime is generally found for particles of a diameter below 1/10 lambda; at this scale, the particle's geometry does not significantly influence the radiation pattern, and the scattering is homogeneous and isotropic in the backward and forward directions. The bigger the particles get, the more forward direction radiation (α =1) is favored. The forward scattering overweighs the back-propagation for bigger particles, and the radiation pattern is limited in a narrower propagation space, as shown in figure 1.1.

Therefore, in practice, the light scattered from a subwavelength biological sample or by the subwavelength cell structures depends on their size. However, if interested in very small nanoparticles, working in a reflection or transmission is alike because of the similarity between forward and backward radiation patterns. Nevertheless, working in transmission can be more advantageous in terms of scattered light to study bigger particles or biological samples.

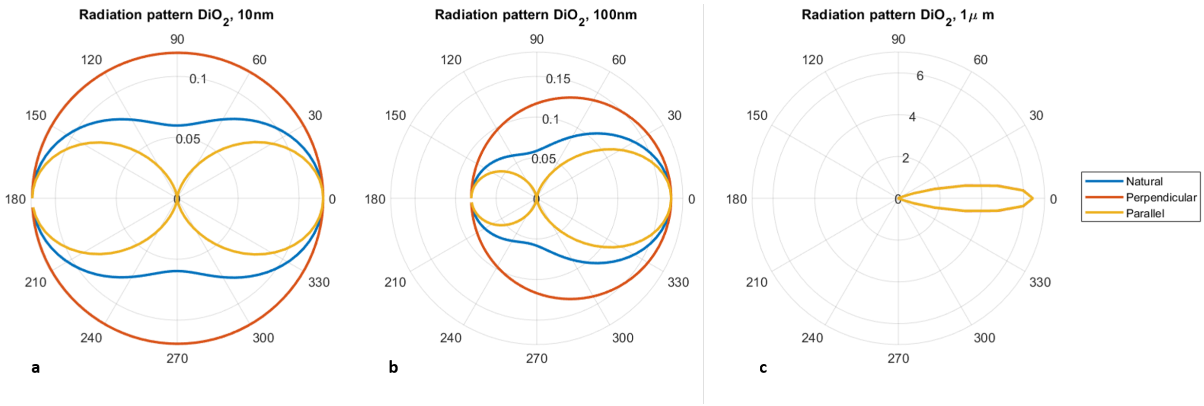

Figure 1.1: **Polar graph of the scattering pattern**. Light is incident from the left on a sphere located at the center of the polar plot, **a**, **b**, and **c** present the radiation pattern of SiO_2 particles of 10, 100 and 1000 nm , respectively in diameter, for particles immersed in water and an illumination wavelength of 455nm . Natural, perpendicular and parallel polarization are presented for each size of the particle using Mie online calculator[1].

Usually, the Rayleigh regime describes the behavior of small sub-wavelength nanoparticles when illuminated by visible light by considering the scattering (equ1.2) and the absorption behavior of particles (equ1.3) of interest. These two terms depend on the complex polarizability of the particle α_p (equ1.4).

$$\sigma_{scat} = \frac{8}{3}\pi^2|\alpha_p|^2|\lambda|^{-4} \tag{1.2}$$

$$\sigma_{abs} = \frac{2\pi}{\lambda}Im(\alpha_p) \tag{1.3}$$

$$\alpha_p = 3\epsilon_m V\left(\frac{\epsilon_p - \epsilon_m}{\epsilon_p + 2\epsilon_m}\right) \tag{1.4}$$

Where λ represents the illumination wavelength, ϵ_p and ϵ_m denote the permittivity of the particle and of the embedding medium, respectively.

Here, we note that the wavelength-dependent complex quantities ϵ_p and ϵ_m determine the balance between absorption and scattering contributions. Therefore, the extinction electric field radiated by the particle is α proportional to the incident electric field E_i (equ1.5).

$$E_s = \alpha_p E_i \tag{1.5}$$

Here, we can see that the scattered electric field scales with the third power of the particle's radius and depends on the permittivity difference between the particle and the surrounding medium. Therefore, the cross-section area, of the particle, σ can estimate the interaction area between the illumination light and particle of interest, this interaction is favored by increasing the cross-section to the beam area (A) ratio. This ratio could increase by focusing the illumination light density on the sample of interest. The extinction cross-section of a single dipole amounts to $\frac{3\lambda^2}{2\pi}$ [2]. Spatial coherent laser light can be focused on an area of $\left(\frac{\lambda}{2}\right)^2$. Despite its inefficiency for detecting small nanoparticles at room temperature (because of their small cross-sections), optical microscopy techniques have been successfully used to detect very small particles. Light-matter interaction has shown to observe individual ions trapping in vacuum [3], even more, to detect a single molecule via extinction contrast when working at cryogenic temperatures[4].

In terms of order of magnitude, if a single dye molecule having a cross-section of the order of $5 * 10^{-16} cm^2$ is placed on the focus of a high NA objective lens having an illumination cross-section of the order of $5 * 10^{-10} cm^2$. Although that molecule extinction cross section is a million time smaller than the incident illumination cross section, the detection of such weak signal has been proved to be possible. Here, the sensitivity limitations are the detector noise and the straight light coming from the incident light only. The pure extinction term consists of a minimal signal of interest compared to the incident light representing a huge background offset. Darkfield microscopy techniques provide a solution to get rid of the background offset. However, these techniques rely on the rejection of the illumination light, usually by blocking the numerical aperture of the incident beam or using other methods based on total internal reflexion [5]. Therefore, scattering-based detection became an attractive field to study the nanoscale domain thanks to the unlimited supply of photons due to potent light sources.

Despite the fact that the amplitude of the extinction field introduced by a small particle is relatively weak, the measurement of such an entity gets more complicated when measuring the intensity (proportional to the squared amplitude of the electric field) of the signal. Here, the interferometric amplification of the signal introduces a noticeable advantage.

1.2 Interference based microscopy

An interferometric detection scheme can partially address the drastic drop in scattering signal with particle volume. When measuring pure scattering the intensity scales with a square dependence of the scattered field. However, the interferometric signal scales linearly with the scattered field. This concept was discovered long ago and was reported by F.Zernike when introducing the phase-contrast microscopy technique [6]. Later, Zeiss developed a differential interferometric contrast objective lens; here, it consists of increasing the contrast by attenuating the reference illumination in the back focal plane of the objective lens [7].

Different configurations of interferometric scattering set-ups have been used in reflection and transmission. The principle of scattering interferometry is to use the incident illuminating light as a reference instead of rejecting it. Regardless of the approach used, the power intensity irradiating the detector P_d can be expressed as:

$$P_d \propto |E_r + E_s|^2 \tag{1.6}$$

E_r and E_s represent the reference and the scattered electric field, respectively. The detected power consists of an intensity that refers to a number of photons N detected during the measurement time. Therefore equ1.6 can be presented as:

$$\mathrm{N} = \mu\left(\mathrm{N}_i(\zeta^2 + |s|^2 + 2\zeta s\cos(\delta\phi))\right) \tag{1.7}$$

Where μ is the efficiency of the detector used. ζ represents the portion of amplitude background. s represents the complex scattering amplitude, $\delta\phi$ the phase difference between the scattered and reference electric fields and N_i , the incident number of photons.

Equ 1.7 shows the emergence of three terms: a reference terms that is usually the background level, a (very low) pure scattering signal, and an interference term that combines the reference and the scattered signal of interest. A phase term modulates the interference term. Here, note that the interference between the scattered and reference fields occurs if the path difference between both fields is smaller than the coherence length of the source used.

In practice, the most common case is one of the weak scatterers where ζ»s and therefore the pure scattering term can be neglected, and the detected power on the camera can written as:

$$\mathrm{N} = \mu\left(\mathrm{N}_i(\zeta^2 + 2\zeta s\cos(\delta\phi))\right) \tag{1.8}$$

The ratio of detected photons in the presence of a sample to the number of detected photons coming from the reference only represents the contrast as:

$$contrast = 2\frac{|s|\cos\delta\phi}{\zeta} \tag{1.9}$$

Therefore, the contrast of the dynamic interferometric signal of interest is maximized for $cos\delta\phi = 1$, therefore:

$$contrast = 2\frac{|s|}{\zeta} \tag{1.10}$$

The contrast equation shows the dependency of the scattering terms(depends directly on the complex polarizability of the sample) and the phase difference between the incident field and the scattered field. In addition, here we can see that the contrast can be tuned by controlling the reference amplitude.

The signal of interest S depends on the number of photons, $\mathrm{S} = contrast * \sqrt{\mathrm{N}}$, where N is the number of photons. The camera noise when working near to the saturation level is attributed to the shot noise level depends on the square root of number of detected photons$noise = \sqrt{\mathrm{N}}$. Thus, the signal to noise ratio of the optical set-up when shot noise limited is expressed as:

$$\mathrm{SNR} \propto contrast\sqrt{\mathrm{N}} \tag{1.11}$$

To sum up, the interferometric contrast of interferometric scattering microscopy systems depends on the incident power illuminating the sample as well as the portion of incident light that reaches the detector. In terms of sensitivity, the SNR scales inversely proportional to the number of photons which explains the need of high full well capacity detectors.

1.3 Single particle tracking and analogy with single molecule fluorescence microscopy

Despite the weak light scattering level of small particles that scales with the amplitude of the incident electric field, interferometric scattering microscopy can be a reliable tool for detecting small molecules thanks to the (unlimited) power of incident light. Therefore, these techniques present a new path to overcome some limitations of single-molecule fluorescence microscopy.

Ground-breaking studies of single-molecule microscopy at room temperature are based on fluorescence microscopy. The primary advantage of fluorescence techniques is the ability to label a molecule of interest with a dye molecule, a fluorescent protein, or a semiconductor quantum dot. In linear fluorescence microscopy, light used to excite the fluorescent labels has a shorter wavelength than the fluorescence one due to Stokes shift determined by the fluorophore's electronic and vibrational structure [8]. Usually, the longer wavelength of the signal of interest emitted by the fluorescent labels can be retrieved using dichroic filters.

The noticeable advantage of fluorescence is hence the rejection of background. Fluorescence microscopy approaches have been widely used for single molecules detection in complex biological samples [9]. For instance, these approaches have been used to study labeled fixed samples with a nanometric precision, known as single-molecule localization microscopy. they have been also employed to follow the dynamics of labeled proteins in biological samples using a single-particle tracking approach. The concept is to track the position of a single emitter to follow its spatial and temporal variation progressively. In practice, for conventional fluorescence microscopy, the optical image of a subdiffraction species returns the point spread function (PSF) of the microscope centered on the object's location. The PSF is imposed by the numerical aperture of the optical system and the wavelength emitted from the fluorophores. Hence, determining the position of the PSF's gravity center with the best precision represents the goal of this kind of measurements.Despite that, usually, fluorescence microscopy is used with wide-field excitation; we show in fig1.2 a comparison between the extinction and fluorescence response of a single dye molecule when using a confocal illumination. Such configuration promotes the interaction between the incoming beam and the particle of interest.

Single-molecule fluorescence microscopy is characterized by its high accuracy thanks to its high achievable precision in positioning. The precision can be approximated to $\sigma N^{-0.5}$ when working on a shot noise level limit, σ is the gaussian fit of the PSF spot. Where σ is the standard deviation of the PSF and N represents the number of detected photons. In terms of order of magnitude, a standard detector that collects about 10^4 photons presents a few nanometers in terms of positioning accuracy for a high numerical aperture microscope objective[11].

Fluorescence provides a crucial advantage represented by the ability to detect molecules on low background. It presents some limitations and several restrictions. We would like to note that the labeling process with the corresponding fluorescent label can be a non-trivial task, where the adapted label should be used depending on the sample of interest and the optical set-up. The fluorophore's photophysical and chemical properties restrict the total yield in

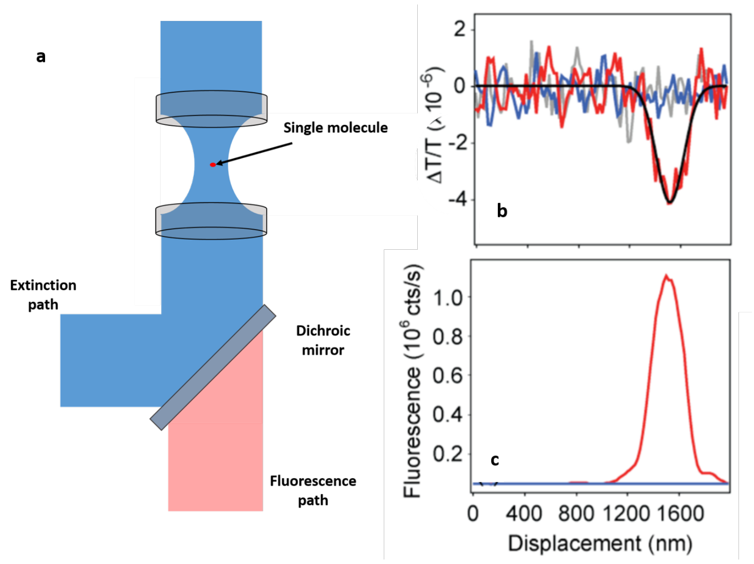

Figure 1.2: **Single-molecule optical microscopy**, **a** schematic representation of the optical set-up in which the incoming light is focused using a high numerical aperture objective lens on a single dye molecule. The collected light using high NA is seperated using a dichroic mirror into extinction and fluorescence paths. **b** and **c** represent respectively the extinction and fluorescence signal magnitude of a single terrylene diimide, the images are adapted from [10].

the number of photons[12]. Therefore, the limitation of photoemission is caused by photobleaching (the dye or fluorophore molecule is permanently unable to fluoresce because of the modification of its chemical properties) and photo blinking (the fluorescent label alters randomly between an ON and OFF state even for a continuous illumination) limitations that become more likely at high illumination intensities and results in the destruction of the fluorophore, hence preventing long measurements. The use of non-blinking quantum dots, NV-centres in nanodiamonds, and carbon nanofibers [13] can be a solution when their use is possible (despite the fact that all fluorescent emitters can reach an optical saturation). These limitations induce some practical complexity by limiting the acquisition time and speed. In addition, the labeling process can introduce some artifacts to the interpretation of the behavior of the sample.

Despite that a nm precision in the localization precision is possible using fluorescence based microscopy methods, it is costly in terms of the exposure time of the detector and, therefore, the acquisition rate. Even though the acquisition rate is not critical for fixed samples, it can be crucial for high-speed imaging dynamics on a molecular level. A trade has to be found to reveal fast dynamics. Here, interferometric scattering microscopy provides a label-free technique to study fast dynamics in a system for unlimited incident light source power [14].

1.4 Interferometric scattering microscopy: optical set-up configuration

Interferometric scattering microscopy has been employed in different contexts. The most employed techniques are based on a common path interferometer in which the reference and the scattered light follow a common path approach. Such configuration can be robust against mechanical instabilities and can be easily employed in a simple optical set-up design. Interferometric scattering microscopy techniques have been widely employed in studying biological samples mainly.

A simple conventional bright-field configuration can detect small nanoparticles such as viruses and vesicles with a suitable sensitivity [15]. Common path interferometric full-field microscopy detection presents a main advantage since it operates in a wide field mode similar to epi-fluorescence microscopy in which a collimated beam is used to illuminate the sample. Note that a common path interferometer is found in most conventional microscopy techniques working in transmission or reflection. Nevertheless, standard bright-field arrangements are not used for sensitive extinction imaging because the detector simply does not have the required dynamic range to process a small signal on a significant offset background, or the incident light sources are not powerful enough to study fast dynamics with short exposure time.

There are several ways for the implementation of interferometric microscopy techniques, each technique has its unique benefits and disadvantages.

1.4.1 Set-up working in reflection

The configuration of the optical set-up in reflection presents an attractive way to detect weak scatterers, this approach has been developed and employed in Sandoghdar as well as Kukura's group. It has a significant advantage compared to the set-ups working in transmission thanks to the use of the coverslip reflection to attenuate the reference beam whereas the scattered beam is not damped. Due to the interference glass water, about 0.4-0.5% of the incident light will be reflected in the objective lens, while most incident light passes through the sample. For small particles (less than 50nm), the scattered light from small particles is often isotropic. As a result, the relative amplitudes of scattered and reflected light fields are closer, increasing the scatterer's signal contrast. Therefore, the principle of the technique relies on the illumination and subsequent collection of the light that returns from the sample. The separation between the illumination and detection path is done using a beam splitter. This technique has several deviations based on the illumination and detection employed.

Confocal configuration

In its first implementation, Lindfors et al employed interferometric scattering microscopy using conventional confocal microscopy working in reflection [16]. The concept of focusing the illumination light on the sample increases the sample cross-section to the beam cross-section ratio to favor the scattering detection, a schematic representation is shown in fig1.3 a. Nonetheless, a pinhole limits the light beam collected by the detector. The detection of small nanoparticles of gold (< 5nm in diameter) has been reported using this configuration. The sample has been scanned along the XY direction to retrieve the spatial information. Yet, the acquisition rate is not critical when the nanoparticles are fixed on the coverslip. However, fast rate acquisition can be crucial when conducting dynamic measurements in biological samples.

Here, replacing the confocal illumination with a Koehler illumination or high-speed scanning beam using a camera-based detector can be an advantage for high throughput imaging. In addition, replacing a point detector with a wide field detector can make this set-up more efficient in practicality and performance.

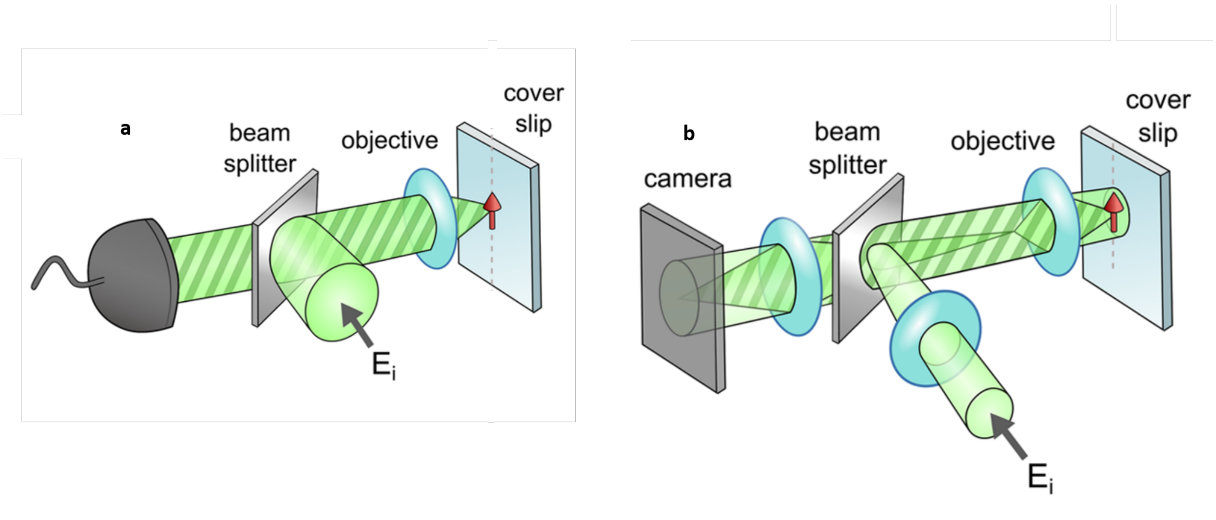

Figure 1.3: **Schemes of interometric scattering microscopy in reflexion**, E$_i$ represents the incident electric field and the red arrow designates the sample, **a** schematic representation of a confocal illumination and **b** shows a schematic representation of a wide field illumnation.[17]

Wide-field imaging

Wide-field imaging relies on detecting the reference light (or a part of it) and light coming from the sample on the same 2D detector instead of scanning a point detector, as shown in fig1.3 c. Therefore, a Koehler illumination is known to generate an even and homogeneous sample illumination. In other words, the illumination beam is focused in the back focal plane of the objective lens, and the collected light consists of the scattered and reference light beam partially reflected from the glass water interface. Light collected by the objective is directed to a beam splitter, and in the detection arm, light is focused using a tube lens on a 2D camera detector.

As we mentioned earlier in this chapter, interferometric scattering microscopy techniques are demanding in terms of power. Thus, the use laser sources can be an attractive option for its high power directive beam. For a Koehler interferometric scattering microscopy, the quality of the image depends mainly on the mode stability, the Gaussian-like mode character, and the coherence length of the source. The first two characteristics can be adjusted using spatial filtering such as injecting the laser in a single mode fiber using an iris diaphragm.

In brief, for interferometric scattering microscopy requires the coherence length of the incident light beam should be longer than the optical path difference between the reference and the scattered field. The coherence length determines the distance for which the two fields interfere with each other. Nevertheless, an unwanted issue can appear because of the long coherence length. Some image artifacts and speckle patterns can degrade and corrupt the image quality[18]. The characteristics of these patterns and the image's deformation ratio depend mainly on the way the illumination source is focused in the back focal plane of the objective lens. The quality of the image hence is degraded because of the instabilities of the unwanted interference. Eventually, if the speckle pattern is stable, the interest signal can still be retrieved by simply removing the fixed background. However, in practice, it is complicated to have a stable fix unwanted speckle pattern in interferometric microscopy and get more complicated to image a wide field of view about 100s μm^2 even for fast acquisition rate interferometric microscopy (1000 fps).

Scanning Wide-field imaging

A trick has been used to minimize the coherent artifact effect (speckle) when using a laser illumination. The idea consists of underfilling the back focal plane of an objective lens with a collimated beam and therefore creating a like pencil beam shape. The benefit of such illumination consists of decreasing the size of the reflected beam and therefore decreasing the area of reflection from the interface, which induces a high signal of interest contrast. Another concept uses a like confocal beam illumination with a wide field detection approach [19]. Here, rather than scanning the sample using a single detector, a focused beam is periodically scanned across the sample at a higher rate than the camera's exposure time . In practice, to reach such a scanning rate, two acousto-optic deflectors positioned in orthogonal directions are needed to perform this kind of illumination. Hence, thanks to the averaging due to the scanning beam, unwanted speckle interferences are attenuated without affecting the signal of interest. Yet, the maximum acquisition rate will be limited by the scanning rate of the AO deflectors that require a certain amount of cycles to illuminate the sample in a homogeneous way, as presented in fig1.4a.

Interferometric reflectance microscopy

So far, all the method consists of an epi-fluorescence like microscope working in reflection. A different configuration has been employed where the particles are fixed on a transparent substrate deposited on a silicon wafer. This method is known as Single-particle interferometric reflectance [20], a schematic representation is shown in fig1.4b. This configuration is equivalent to a folded version of a set-up working in a transmission configuration. Therefore, scanning an image plane can retrieve the signal of interest. Here, the optical path difference between the reference and the particle of interest is controlled by the thickness of the transparent substrate. All these different configurations have some advantages compared to the other in terms of temporal or spatial resolution, sensitivity, and complexity.

These methods rely on detecting the interference of reference light representing a portion of light reflected and light scattered from the sample of interest. Here, we would like to note again that to detect interference, the optical path difference between the reference field and

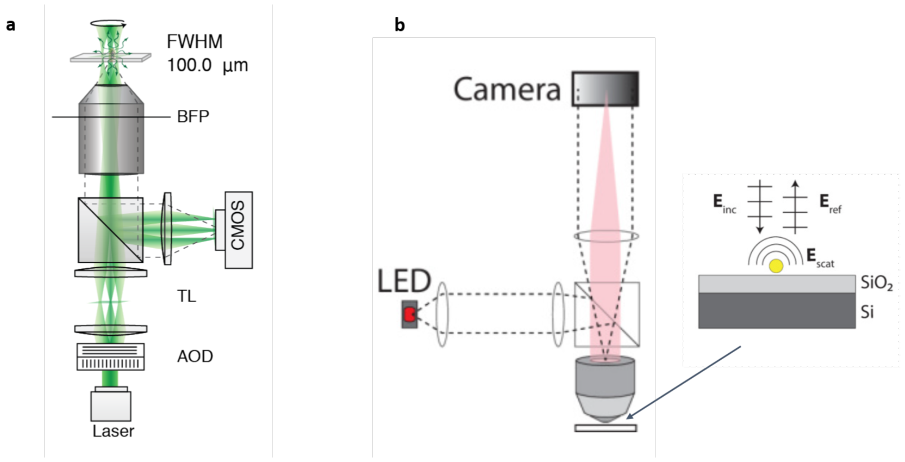

Figure 1.4: **Schemes of scanning wide-field interferometric scattering microscopy and interferometric reflectance imaging**, **a** schematic representation of a like-confocal illumination using acousto optic deflector to scan the sample of interest [17] and **b** shows a schematic representation of a wide field illumnation, in which an SiO_2 nanaoparticle is scanned by moving the position of the objective lens .[20]

the scattered field should be smaller than the coherence length of the light source. Hence, this condition restricts the ability to image deep in the solution, at a far distance from the coverslip. Therefore, the use of a set-up working in transmission can be advantageous to image a sample without being restricted to small distances from the coverslip.

1.4.2 Set-up working in transmission

The use of an interferometric scattering microscopy setup in transmission has the advantage of imaging deep in the sample solution, since both, the scattered and the reference beam follow the same optical path (not limited to small distances near the coverslip). Nevertheless, light transmitted through the sample and collected by the objective lens represents the reference signal that will interfere with the scattered signal. Consequently, when working at the same saturation level of an identical detector, the interferometric contrast for small nanoparticles is smaller in transmission than in reflection configuration.

Huang et al. introduced COherence BRIght field microscopy (COBRI) in 2017. It consists of an interferometric scattering approach working in transmission. It has proved to have a similar sensitivity to the reflection configuration when attenuating the reference in the back focal plane. Briefly, the illumination configuration used is like confocal illumination scanning the sample plane at a high-speed rate. For the detection, a 2D camera is used. Eventually, acousto optic modulators scan a few μm^2 field of view at a high acquisition speed rate of the camera [21]. This method also proves that imaging deep in a solution can be possible in the nonexistence of a reference surface despite the enhanced precision of the axial precision of the configuration working in reflection [22].

Full-field interferometry techniques have also been employed in a transmission configuration. The concept uses the conventional microscope working in transmission using a high-power LED source, an incoherent light source to reduce the unwanted interferences, and an adapted CMOS camera characterized with a high full well capacity [15]. This method proved its ability to detect small viruses and nanoparticles using a simple optical set-up.

To sum up, here we presented the principle of function of interferometric microscopy techniques in different configurations. These methods have been used to study mainly static and dynamic behavior biological samples. Each method can have some benefits in terms of sensitivity, speed rate, field of view, and simplicity.

1.5 Single particle tracking (SPT)

The ultra-sensitive ability of interferometric scattering microscopy and the capability of very high acquisition rates prompt the use of a single particle tracking algorithm to follow the spatial dynamics of very small scatterers.

In its most common implementation, the use of SPT is widely known in fluorescence microscopy, in which the object of interest is typically labeled with an organic or non-organic fluorophore. The concept relies on following the spatial position of each fluorophore in the sample as a function of time. As presented previously, the center of the PSF is attributed to the position of the fluorescent label. A common way to retrieve the center of the spot is to use a 2D Gaussian fitting. Let us mention that the modification of the axial position of the fluorophore induce a defocus presented by a decrease of the intensity detected signal and a loss in terms of resolution (larger PSF). This process is repeated for all the acquired frames individually, and the next step is based on linking candidate spots to retrieve the acquired trajectories. In addition to the variation of the emitter's position around the focal plane of the objective lens, the photochemical characteristics of fluorophores can also induce gaps in the trajectories. That results in a lessening of the statistical data [23]. We would like to mention that some limitations can be addressed by simply modifying the observation duration per trajectory.

Interferometric scattering microscopy can overcome some limitations mainly the one induced by the properties of the fluorescent labels. Regardless of the illumination power, the scatterers do not saturate, photobleach or photoblink compared to fluorescence. We show fluorescence and interferometric images of SV40 viruses in fig 1.5. In addition, differences are found in the interferometric PSF (iPSF) shape and mainly in the axial PSF when the object of interest moves in a 3D way in the sample. Interferometric PSF represents an implicit way of measuring an amplitude affected by a phase term producing constructive and destructive interferences that depend on the axial position of the object. The other difference can be seen in the sensitivity of the detection signal of interest from the background. Interferometric PSF is presented by a variation of the signal of interest regarding the background offset that does not contain information of interest. Therefore, the localization accuracy is estimated from the number of interferometric signals consisting of the signal of interest over the static background. As presented in fig 1.5, we can see a negative value due to destructive interferences for dielectric particles.

Hence, for a limited power of the incident light, one has to accept slightly lower than theoretically achievable localization precision by acquiring fast images or sacrificing some temporal

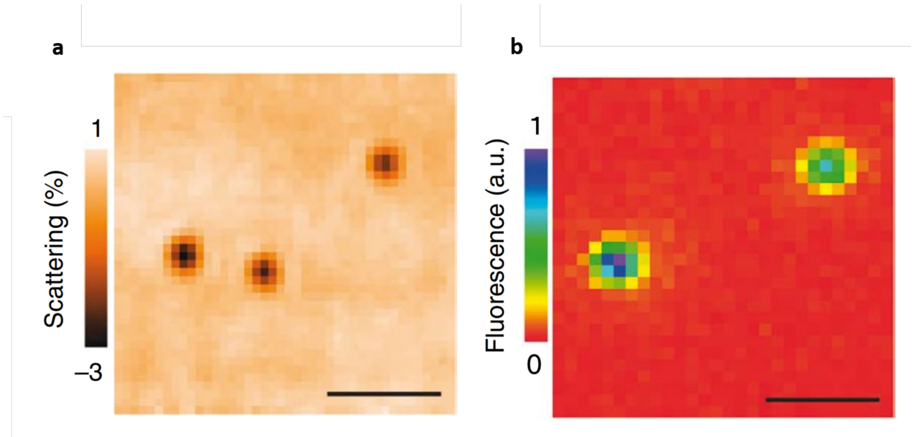

Figure 1.5: **Point of spread function comparison**, **a** interferometric scattering PSF of SV40 virus moving on a lipidic membrane and **b** fluorescence PSF due to a quantum dot label of the virus membrane, scale bar=1μm, images adapted from [24]

resolution for spatial precision even if the nominal localization precision is high at very low exposure times. These abilities make interferometric scattering microscopy techniques suitable to image label-free biological samples dynamics.

1.6 Performance and applications

About two decades ago, small gold nanoparticles were detected using interferometric scattering microscopy in a reflection configuration [16]. This proof of concept was achieved by the group of Sandoghdar using a point detector. This concept has been proved to work in transmission with a high sensitivity similar to the reflection using confocal illumination and a camera based detector [21]. The use of a camera-based detector simplified the use of the optical set-up. In these experiments, the nanoparticles of interest are fixed directly on a coverslip, reducing the effect of artifact due to unwanted interferences. Here, the fixed background can be subtracted using a simple temporal median or means intensity. Therefore, the detection of the signal of interest is achievable over a fixed background for the appropriate exposure time of the camera. However, a short exposure time is essential for studying dynamics in biological samples.

In practice, when working with biological samples, spatial and temporal fluctuations appears in the background signal making the distinction between the fluctuations of the signal of interest and the unwanted fluctuations coming from the background more complicated. Different approaches have been used to remove unwanted background. In dynamic studies, the background can be appropriately eliminated if the particle of interest appears on the sample or moves within it faster than the changes in the background. It, therefore, consists of applying a rolling average to remove the stationary part of the image. For situations where the background possesses high spatio-temporal dynamics, as is the case for live biological specimens, more complicated image processing is usually used [25]. Finally, we want to mention that in a configuration working in transmission, the background speckle can be reduced since the reference and scattered beam experience smaller phase difference due the presence of the objective lens only.

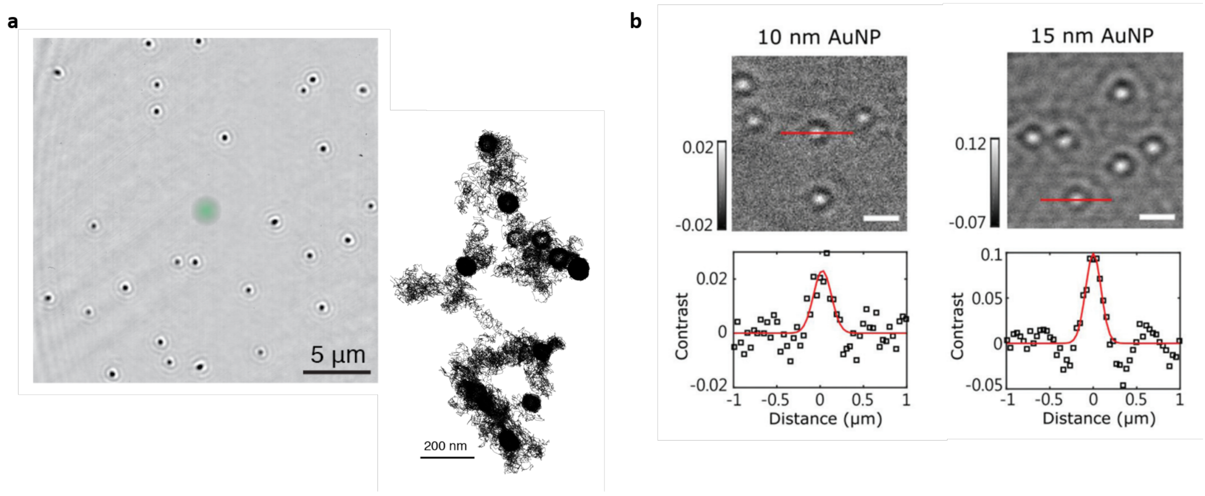

Figure 1.6: **Gold nanoparticles in interferometric scattering microscopy**, **a** interferometric scattering image of a conjugated 40 nm AuNP on a supported lipid bilayer and trajectory a single particle resulting from SPT, adapted from [17]. Image **b** represents AuNP in transmission configuration and their corresponding interferometric intensity profiles adapted from [26], scale bar= $1\mu m$

In early studies, interferometric scattering microscopy techniques have been used to study viruses supported by lipid bilayers [24]. Later, interferometric scattering microscopy was used to study the diffusion properties of lipidic layer [14]. Here small gold nanoparticles (GNP) were used as a label contrast to study the diffusion properties of a bilipidic layer, as shown in fig 1.6 a. GNP of 2nm has been used to label molecules of interest and therefore reduce the impact of bead on the interpretation of biological samples. Yet semiconductor colloids such as nanocrystal quantum dots are employed to extend the sensitivity beyond the one of GNP [27]. We note that dye molecules, quantum dots, and metal nanoparticles have spectral resonances. Therefore, having an imaginary absorption component in complex polarizability or a high refractive index can be used to label biological samples consisting of dielectric, non-resonant material efficiently.

Viruses and virus-like particles samples represent the perfect application for these techniques. Where the polarizability of the particles depends on the size of the object and the difference of refractive index between the particle and its surrounding medium, some configurations of imaging sensing and imaging single virus particles have been employed by monitoring the particles of interest binding near to the coverslip [24, 28]. Other methods consist of monitoring viruses directly in the solution sample [15] . An important fact is that the interferometric contrast allows estimating a refractive index if the particles have a similar size. the ability of monitoring the estiating the refractive index variation consists is particularly interesting to follow capsids formation. This application is partuclarly interesting for measuring DNA loads of particles in capsids during their formation [29].

Furthermore, the sensibility of the interferometric scattering methods have proved their capabilities of detecting a single protein. Roughly, a protein is 1000 times smaller than an average size virus. In 2014, it was reported by Ortega Arroyo, J et al. for the first time the detection of a single protein [19], the first label-free detection, imaging, and tracking of single proteins, illustrated by myosin 5 molecules walking along actin (proteins down to 66 kDa).

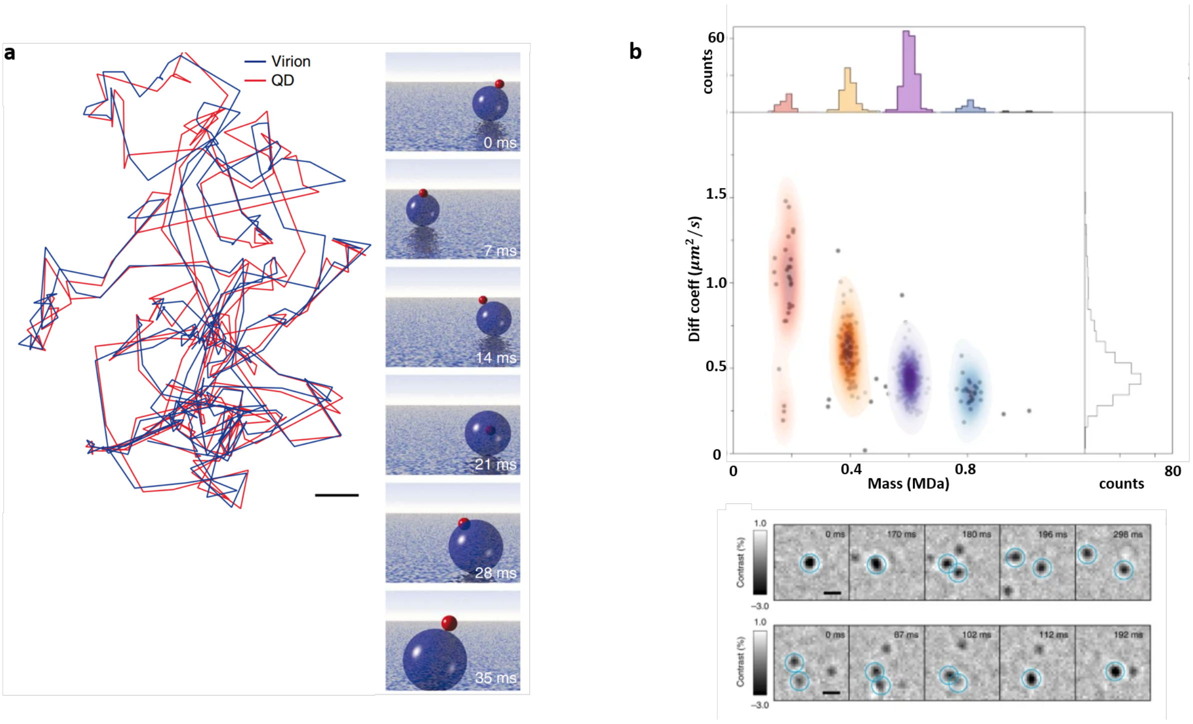

Figure 1.7: **Single virus and single molecule analysis representation** , **a** shows the trajectory of a virus labeled with a quantum dot analysis to study the motion and the direction of the virion on a lipidic membrane as presented in the virtual construction [24]. Image **b** represents the major diffusion coefficient component of molecules versus the estimated mass of the molecule using the interferometric contrast.[30]

Despite reaching the maximum limit of detectors in terms of full well capacity, thanks to the presence of a powerful light source, the attenuation of the reference light beam is an appealing way to reach higher interferometric contrast to detect free molecules. Masking part of the reference light in the back focal plane has been majorly employed to enhance the contrast and therefore, the limit of detection of the optical set-up. As mentioned earlier, the interferometric signal depends on the size and the refractive index of the particles, however, all molecules have a very similar refractive index. Therefore, the interferometric contrast can reveal the mass of each molecule, the resolution of the microscope is therefore defined in mass, defines the resolution of the microscope's performance as a mass measurement device and reaches values as low as 19 kDa [30], the approach is known as mass photometry, shown in fig1.7b.

On a larger scale, interferometric scattering microscopy techniques, usually label-free methods mainly used to image cells, are based on holography and quantitative phase imaging [31]. Interferometric microscopy techniques extend the study of the nanoscopic structures, such as topology and monitoring average mechanics dynamic variations in a wide-field configuration in transmission [32]in fig 1.8b. Other applications consist of labeling and tracking nanomechanics modifications inside cells using 3D single particle tracking algorithm [25], shown in fig1.8. Interferometric microscopy techniques have also been used to image action potential in a single neuron following a stimulated execution [33]. It has been shown that images can be acquired at a very high speed (several thousands or one million frames per second) for ultra-fast dynamics[21, 25].

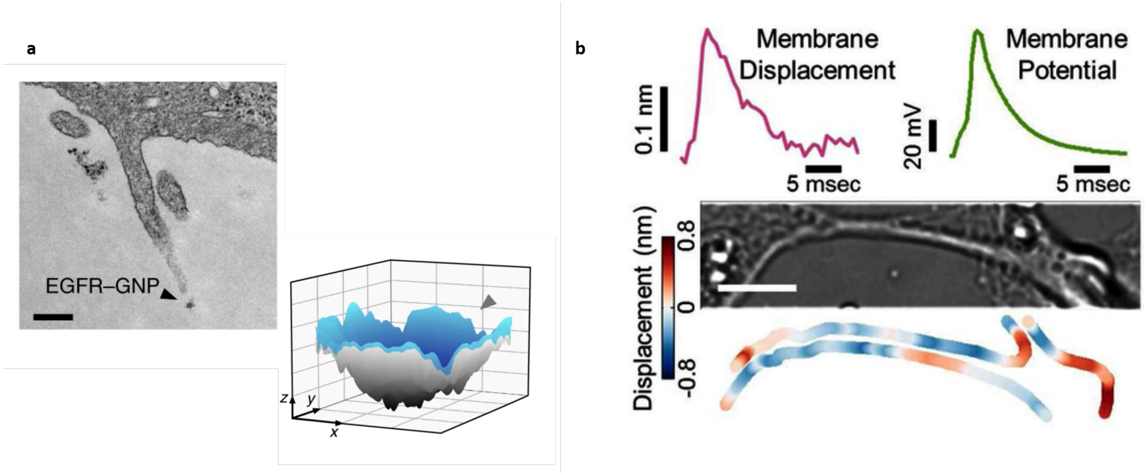

Figure 1.8: **Reconstruction of interferometric scattering images to reveal biomechanics** , **a** A TEM image of a filopodium including an EGFR–GNP and filopodium surface reconstructed from 780,000 trajectory points with a localization error of x,y = 2 nm recorded at 1,000 fps, from [25]. Image **b** Mapping and quantification of local membrane displacement accompanying an action potential, scale bar=10μm adapted from [33]

All these applications show some fundamental advantages regarding other single-molecule optical microscopy approaches, namely the ability to observe new dynamics and to do so beyond the scope of current state-of-the-art of fluorescence approaches. Different configurations are being used to reveal dynamics in biological samples to study molecules or particles of interest or the ensemble dynamics in the field of view. Fast acquisition time is possible due to powerful light sources to overcome the weak scattering signal from small particles. Light source characteristics are crucial for having enough intensity power and increasing the interferometric contrast.

1.7 Challenges and limitations

The sensitivity of the optical system can be defined using the contrast definition in section 1.2. The primary key is to have enough power to fill the camera's dynamic range and attenuate the reference light ideally to match the scattered light.

High dynamic range cameras or more precisely high full well capacity (FWC) are needed because of their low shot noise level and their ability to collect weak interferometric signals with high background offset. Nevertheless, for a limited dynamic range camera, oversampling the field of view by binning neighboring pixels can be a trick to increase the dynamic range virtually. However, it induces the reduction of the total field of view.

High power light sources are needed to overcome the scattering behavior of small particles by attenuating the reference loght beam. Light sources are characterized by their spatial and coherent length. Usually, LASERs are known for their high coherence length. This property is efficient in focusing light on a small spot. However, interferences between different modes of the LASER degrade the image quality. Even though a static optical path can reduce unwanted interferences, it needs to have a stable system that is not practical for studying dynamics. Therefore, ultra-fast scanning can be a solution. Broadband LASERs present a solution for an unspeckled background, but they can be expensive compared to other sources. Incoherent LED illumination can be efficient; however, Focused light is limited by the size of the LED.

To sum up, different light sources can be used depending on the required sensitivity of the system and the desired simplicity of the optical setup.

Bibliography

[1] Scott Prahl. `https://omlc.org/cgi-bin/mie_angles.cgi?diameter=0.01&lambda_vac=0.455&n_medium=1.33&nr_sphere=1.45&ni_sphere=0&n_angles=100&density=0.1`. 7

[2] Rodney Loudon. *The quantum theory of light*. OUP Oxford, 2000. 8

[3] W Neuhauser, M Hohenstatt, PE Toschek, and H Dehmelt. Localized visible ba+ mono-ion oscillator. *Physical Review A*, 22(3):1137, 1980. 8

[4] William E Moerner and Lothar Kador. Optical detection and spectroscopy of single molecules in a solid. *Physical review letters*, 62(21):2535, 1989. 8

[5] Kyle Marchuk and Ning Fang. Three-dimensional orientation determination of stationary anisotropic nanoparticles with sub-degree precision under total internal reflection scattering microscopy. *Nano letters*, 13(11):5414–5419, 2013. 8

[6] F Zernike. Phase contrast. *Z Tech Physik*, 16:454, 1935. 8

[7] RD Allen and GB David. The zeiss-nomarski differential interference equipment for transmitted-light microscopy. *Zeitschrift fur wissenschaftliche Mikroskopie und mikroskopische Technik*, 69(4):193–221, 1969. 8

[8] EW Castner Jr and Mark Maroncelli. Solvent dynamics derived from optical kerr effect, dielectric dispersion, and time-resolved stokes shift measurements: an empirical comparison. *Journal of Molecular Liquids*, 77(1-3):1–36, 1998. 10

[9] Michael J Rust, Mark Bates, and Xiaowei Zhuang. Sub-diffraction-limit imaging by stochastic optical reconstruction microscopy (storm). *Nature methods*, 3(10):793–796, 2006. 10

[10] Philipp Kukura, Michele Celebrano, Alois Renn, and Vahid Sandoghdar. Single-molecule sensitivity in optical absorption at room temperature. *The Journal of Physical Chemistry Letters*, 1(23):3323–3327, 2010. 11

[11] Jennifer C Waters. Accuracy and precision in quantitative fluorescence microscopy, 2009. 10

[12] Ute Resch-Genger, Markus Grabolle, Sara Cavaliere-Jaricot, Roland Nitschke, and Thomas Nann. Quantum dots versus organic dyes as fluorescent labels. *Nature methods*, 5(9):763–775, 2008. 11

[13] SR Hemelaar, P De Boer, M Chipaux, W Zuidema, T Hamoh, F Perona Martinez, A Nagl, JP Hoogenboom, BNG Giepmans, and R Schirhagl. Nanodiamonds as multi-purpose labels for microscopy. *Scientific reports*, 7(1):1–9, 2017. 11

[14] Katelyn M Spillane, Jaime Ortega-Arroyo, Gabrielle De Wit, Christian Eggeling, Helge Ewers, Mark I Wallace, and Philipp Kukura. High-speed single-particle tracking of gm1 in model membranes reveals anomalous diffusion due to interleaflet coupling and molecular pinning. *Nano letters*, 14(9):5390–5397, 2014. 11, 18

[15] Martine Boccara, Yasmina Fedala, Catherine Venien Bryan, Marc Bailly-Bechet, Chris Bowler, and Albert Claude Boccara. Full-field interferometry for counting and differentiating aquatic biotic nanoparticles: from laboratory to tara oceans. *Biomedical optics express*, 7(9):3736–3746, 2016. 12, 16, 18

[16] Kalkbrenner Lindfors, Thomas Kalkbrenner, Patrick Stoller, and Vahid Sandoghdar. Detection and spectroscopy of gold nanoparticles using supercontinuum white light confocal microscopy. *Physical review letters*, 93(3):037401, 2004. 12, 17

[17] Jaime Ortega Arroyo. Investigation of nanoscopic dynamics and potentials by interferometric scattering microscopy. 2015. 13, 15, 18

[18] Daniel Schröder, Joran Deschamps, Anindita Dasgupta, Ulf Matti, and Jonas Ries. Cost-efficient open source laser engine for microscopy. *Biomedical Optics Express*, 11(2):609–623, 2020. 14

[19] J Ortega Arroyo, J Andrecka, KM Spillane, N Billington, Y Takagi, JR Sellers, and P Kukura. Label-free, all-optical detection, imaging, and tracking of a single protein. *Nano letters*, 14(4):2065–2070, 2014. 14, 19

[20] Derin Sevenler, Oğuzhan Avci, and M Selim Ünlü. Quantitative interferometric reflectance imaging for the detection and measurement of biological nanoparticles. *Biomedical Optics Express*, 8(6):2976–2989, 2017. 14, 15

[21] Yi-Fan Huang, Guan-Yu Zhuo, Chun-Yu Chou, Cheng-Hao Lin, Wen Chang, and Chia-Lung Hsieh. Coherent brightfield microscopy provides the spatiotemporal resolution to study early stage viral infection in live cells. *ACS nano*, 11(3):2575–2585, 2017. 15, 17, 20

[22] Jonathan Dong, Dante Maestre, Clara Conrad-Billroth, and Thomas Juffmann. Fundamental bounds on the precision of iscat, cobri and dark-field microscopy for 3d localization and mass photometry. *Journal of Physics D: Applied Physics*, 54(39):394002, 2021. 15

[23] Stephan Uphoff, Rodrigo Reyes-Lamothe, Federico Garza de Leon, David J Sherratt, and Achillefs N Kapanidis. Single-molecule dna repair in live bacteria. *Proceedings of the National Academy of Sciences*, 110(20):8063–8068, 2013. 16

[24] Philipp Kukura, Helge Ewers, Christian Müller, Alois Renn, Ari Helenius, and Vahid Sandoghdar. High-speed nanoscopic tracking of the position and orientation of a single virus. *Nature methods*, 6(12):923–927, 2009. 17, 18, 19

[25] Richard W Taylor, Reza Gholami Mahmoodabadi, Verena Rauschenberger, Andreas Giessl, Alexandra Schambony, and Vahid Sandoghdar. Interferometric scattering microscopy reveals microsecond nanoscopic protein motion on a live cell membrane. *Nature Photonics*, 13(7):480–487, 2019. 17, 20

[26] Ching-Ya Cheng, Yi-Hung Liao, and Chia-Lung Hsieh. High-speed imaging and tracking of very small single nanoparticles by contrast enhanced microscopy. *Nanoscale*, 11(2):568–577, 2019. 18

[27] Gert Wrigge, Jaesuk Hwang, Ilja Gerhardt, Gert Zumofen, and Vahid Sandoghdar. Exploring the limits of single emitter detection in fluorescence and extinction. *Optics Express*, 16(22):17358–17365, 2008. 18

[28] Marek Piliarik and Vahid Sandoghdar. Direct optical sensing of single unlabelled proteins and super-resolution imaging of their binding sites. *Nature communications*, 5(1):1–8, 2014. 18

[29] Rees F Garmann, Aaron M Goldfain, and Vinothan N Manoharan. Measurements of the self-assembly kinetics of individual viral capsids around their rna genome. *Proceedings of the National Academy of Sciences*, 116(45):22485–22490, 2019. 18

[30] Eric DB Foley, Manish S Kushwah, Gavin Young, and Philipp Kukura. Mass photometry enables label-free tracking and mass measurement of single proteins on lipid bilayers. *Nature methods*, 18(10):1247–1252, 2021. 19

[31] YongKeun Park, Christian Depeursinge, and Gabriel Popescu. Quantitative phase imaging in biomedicine. *Nature photonics*, 12(10):578–589, 2018. 19

[32] Houda Bey, Florent Charton, Helena Cruz de Carvalho, Shun Liu, Richard G. Dorrell, Chris Bowler, Claude Boccara, and Martine Boccara. Dynamic cell imaging: application to the diatom phaeodactylum tricornutum under environmental stresses. *bioRxiv*, 2021. 20

[33] Yunze Yang, Xian-Wei Liu, Hui Wang, Hui Yu, Yan Guan, Shaopeng Wang, and Nongjian Tao. Imaging action potential in single mammalian neurons by tracking the accompanying sub-nanometer mechanical motion. *ACS nano*, 12(5):4186–4193, 2018. 20

Chapter 2

Experimental set-up and data analysis

Contents

2.1 Interferometric signal: Mathematical basis

The main interest of interferometric microscopy is its ability to amplify signals of interest, mainly weak signals coming from small scatterers. The detected signal depends mainly on the scattering properties of the sample, its position, and the properties of the reference light beam. This section presents a simplified mathematical model to describe the total collected intensity to find the interferometric signal of interest. Here, we refer to a Michelson interferometer to explain the basic principle and present light behavior in a Linnick common path interferometer working in transmission.

We use a scalar approximation to describe the signal that arises on the photodetector in the case of a Michelson interferometer. In its simplest form, a Michelson interferometer consists of a beam splitter that separates the incident light into two paths. A reference arm that reflects (partially) the incident light and the sample arm in which light interacts with the sample as shown in fig 2.1.

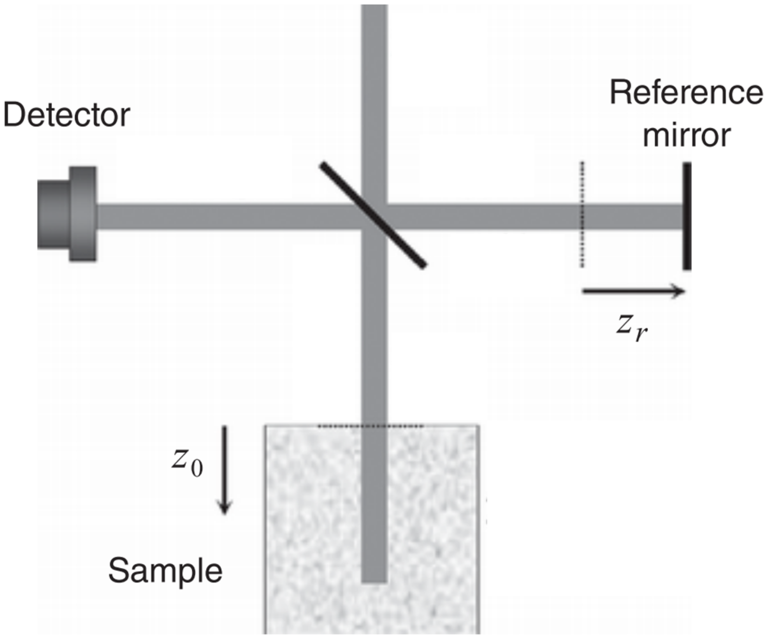

Figure 2.1: **Scheme of a Michelson interferometer**.[1].

Therefore, the intensity collected by the detector consists of the reflected reference and the back-scattered electric field and be written as:

$$E_D(t) = E_i(t - \frac{2}{c}z_r) + \int \rho_z(z_0) E_i(t - \frac{2}{c}z_0)\, dz_0 \tag{2.1}$$

Where the E_d represents the reference electric field reaching the detector, E_i is the incident light z_r represents the reference mirror's axial position,$\rho(z_0)$ and z_0 are the backscattering ratio of the sample, and the position of the axial position of the scatters, respectively and c is the average light speed in the sample.

Therefore, the collected intensity $I_D = |E_D|^2$can be expressed as:

$$I_D = I_{rr} + I_{ss} + I_{sr}(z_r) + I^*_{sr}(z_r) + I_{incoh} \tag{2.2}$$

where:

$$I_{rr} = |E_i|^2 = \zeta^2 I_i \tag{2.3}$$

$$I_{ss} = \iint_{z_0, z'_0} \rho_z(z_0)\rho^*_z(z'_0)E_i(t - \frac{2}{c}z_0)E^*_i(t - \frac{2}{c}z'_0)\, dz_0\, dz'_0 \tag{2.4}$$

$$I_{sr}(z_r) = \int_{z_0} \rho^*_z(z_0)E_i(t - \frac{2}{c}z_r)E^*_i(t - \frac{2}{c}z_0)\, dz_0 \tag{2.5}$$

Where I_{rr} and I_{ss} represent respectively the intensity arising from the reference mirror and the sample only. Here, the reflectivity of the reference arm is expressed as ζ. I_{sr} and I^*sr are the complex conjugate interference terms. I_{incoh} represent the light that does not interfere but still contribute to the detected intensity. To retrieve the interference term as a function of optical path and phase difference, we introduce the temporal coherence of the illumination $\gamma(\tau)$ expressed as:

$$\gamma(\tau) = \hat{\gamma}(\tau)e^{-2\pi c\kappa_c\tau} \tag{2.6}$$

Where $\hat{\gamma}$ is the coherence envelop function and $\kappa_c = \frac{1}{\lambda}$ represents the mean wavenumber of the illumination beam. Hence, the time delay between $E_i(t - \frac{2}{c}z_r)$ and $E_i(t - \frac{2}{c}z_0)$ is $\tau = \frac{2}{c}(z_0 - z_r)$ and therefore, (equ 2.4)can be expressed as:

$$I_{sr}(z_r) = \int_{z_0} \rho^*_z(z_0)\hat{\gamma}(\frac{2}{c}(z_0 - z_r))e^{i4\pi\kappa_c(z_0 - z_r)}\, dz_0 \tag{2.7}$$

Equ:2.7 shows the dependency of the interferometric signal in terms of amplitude and phase on the optical path difference between the backscattered and the reference light. Then the interferometric contrast can be expressed as:

$$I_c = I_{max}\cos(\Delta\phi(z)) \tag{2.8}$$

Where: $I_{max} = 2\frac{|\rho|}{|\zeta|}$

The phase difference $\cos(\Delta\phi(z))$ modulates the interferometric contrast. This phase term consists of an optical path difference term and an intrinsic phase ϕ^i:

$$\Delta\phi(z) = 4\pi\kappa_c(z_0 - z_r) + \phi^i \tag{2.9}$$

The intrinsic phase represents the phase shift induced by the sample ϕ^s in addition to a phase shift induced by the numerical aperture of the system. Here, we would like to note that each numerical aperture induces a phase shift, known as Gouy phase shift ϕ^g near to a focus, that occurs for a converging beam near its focus. The Gouy phase phenomenon can be explained based on the uncertainty principle, where the action of spatially confining a beam of light in the transverse direction by focusing results in an increase in the spread of momenta, which in turn leads to a phase shift[2]. In other words, for a fixed reference path, an additional phase shift is added to the phase induced by the optical path difference that varies depending on the position of the scatterer regarding the focus of an objective lens. For instance, the interferometric contrast I_c of a single scatterer can be described as:

$$I_c = I_{max}\cos\left(4\pi\kappa_c(z_0 - z_r) + \phi^s + \phi^g\right) \tag{2.10}$$

where:

$$\phi^s = \arctan\left(\frac{Im\alpha}{Re\alpha}\right); \phi^g(z) = -\arctan\left(\frac{\lambda}{\pi\omega_0^2}z\right) \tag{2.11}$$

where α is the complex polarizability of the scatterer, ω_0 denotes the waist of a Gaussian beam at the focus point and z is the position of the scatter regarding the focus plane of the lens.

To sum up, in a Michelson interferometer configuration, the contribution of the sample's reflectivity added the phase shift induced by the sample, and the optical set-up are combined to assemble the interferometric signal of interest. Despite that, the interferometric term consists of an amplitude and a phase modulation, these parameters are encoded in an intensity term. In practice, the variation of the axial position of the scatterer of interest induce a variation in terms of interferometric contrast.

The interferometric contrast presented in equ2.10 describes the interferometric contrast for a Michelson interferometer. Thus, the interferometric contrast in a common path interferometer working in transmission can be described as $I_c = I_{max}\cos(\phi^s + \phi^g)$, but with a null phase shift due to the optical path difference ($z - z_0$=0). Nonetheless, the phase shift is attributed only to the sample and the numerical aperture since the reference, and the scattered light beams follow the same optical path to reach the detector. Nonetheless, since the same variations affect the reference and scattered beam, the transmission configuration can be robust against unwanted artifacts. Furthermore, the use of a low coherence light source can be helpful to get rid of unwanted speckle interferences.

2.2 Experimental set-up

In this section of this chapter, we introduce the basic experimental set-up based on a common path interferometric set-up working in transmission, using spatially incoherent light source to provide the illumination of the sample [3], a schematical representation of the optical setup is shown in fig2.2.

As described in the first chapter, a Koehler illumination with an LED or a thermal source can be used to have a homogeneous sample illumination. However, we choose a simple geometry using an LED with higher optical power that is positioned directly under the coverslip to obtain the best performance. We used an LED at 455nm with a bandwidth (FWHM) of 18nm (L4 455), [Thorlabs, USA]. The coherence length l_c can be expressed as $l_c \propto \lambda^2/\Delta\lambda = 11500nm$. The sample solution is deposited on the coverslip. To collect light transmitted inside the sample solution containing nanoparticles, we used a water immersion objective lens (100x, NA=1.0) [Olympus, Japan] dipped directly in the solution sample (or oil immersion objective).

Light collected by the objective lens is directed to a tube lens, which focuses on a CMOS camera. Here, the detector is the most crucial part of the set-up since the system's sensitivity is strongly dependent on the camera technology. The signal-to-noise ratio (SNR) is linked to the full well capacity (FWC) as described in the previous chapter 1.2. FWC is the number of photo-electron the camera can probe per pixel. For fluorescence applications, the number of probed photons is low, and a suitable camera must provide a low dark noise to probe a low number of photons. For interferometric microscopy, it is the opposite here that we aim to collect a large number of photons since the signal of interest is usually weak compared to the background level. Thus, we care less about dark noise because we are working close to saturation, we aim to be shot noise limited in our experiments. Therefore, limited by the Poisson nature of photons arrival and not by the camera's electronic noise.

We are using a large sebsorchip camera,"Quartz 2A750" , [ADIMEC, Netherlands]. This camera is characterized by its large full well capacity $2 * 10^6$ photons-electron at a high frame rate of 720 fps and a 1440*1440 pixels of $12\mu m$. The use of this camera improved the SNR about three times compared to the use of PhotonFocus (MV-D1024E-160-CL-12, Switzerland), which could probe $2 * 10^5$ photo-electrons at 150 frames per second (fps).

For the acquisition software, we adapted a Matlab acquisition software developed in the lab [4]. We used an acquisition rate of 500 fps with a continuous illumination during the acquisition time. The camera and the illumination source are triggered using a National instrument DAQ controller (PCIe-6343) [National Instruments, USA]. The total magnification of the optical system is about 167x, that corresponds to a field of view of 103*103 μm^2.

All the optical set-up has been mounted on a vertical column (95 mm Precision Construction Rail ,Thorlabs) which makes the set-up robust against vibration and mechanical stabilities and versatile.

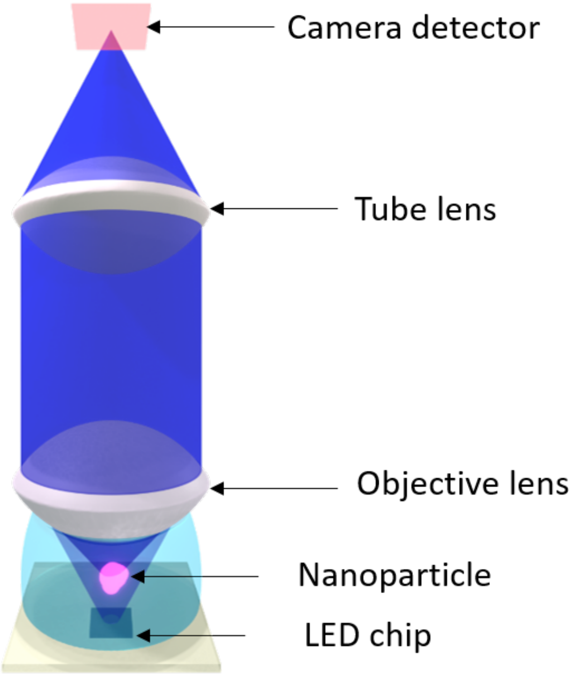

Figure 2.2: **Scheme of the optical set-up**. An LED illuminates the nanoparticles' sample; the light is collected by the objective lens and then focused by a tube lens on the camera.

2.3 Image processing to single particle tracking

This section describes the steps required from raw images to retrieve single-particle trajectories. Using SPT trajectories, we estimate the interferometric signal contrast of each particle and its diffusivity. Therefore we can estimate the hydrodynamic radius and compare the internal composition of different particles based on the refractive index difference.

2.3.1 Image denoising and background removal

Despite using an incoherent homogeneous light source approach, raw images can contain some features from the camera or unwanted static heterogeneities from the sample or even the illumination source. All these constant noises affect the visibility of the particles. Here, removing these patterns is done in some simple processing steps. Raw images are saved in a 16 bit format; we normalize raw images to 12bit format first to homogenize the non-uniform pixel response of some fixed regions on the detector. We calculate the temporal average frame from all the images in the stack, which is subtracted from each stack frame fig.2.3 b. Thus, we eliminate all the static background average patterns because everyhting is fixed accept NPs moving in the solution, and the dynamic signal of interest can therefore be retrieved on a homogeneous background. The process is known as flat fielding (fig.2.3b). Nevertheless, strips artifacts (coming from the camera) are spotted on the processed image, and a simple subtraction cannot remove these stripes. However, the spatial frequency range of these stripes is stable. Using 2D Fourier Transform, we remove the frequencies corresponding to the stripes as presented in (fig.2.3c).

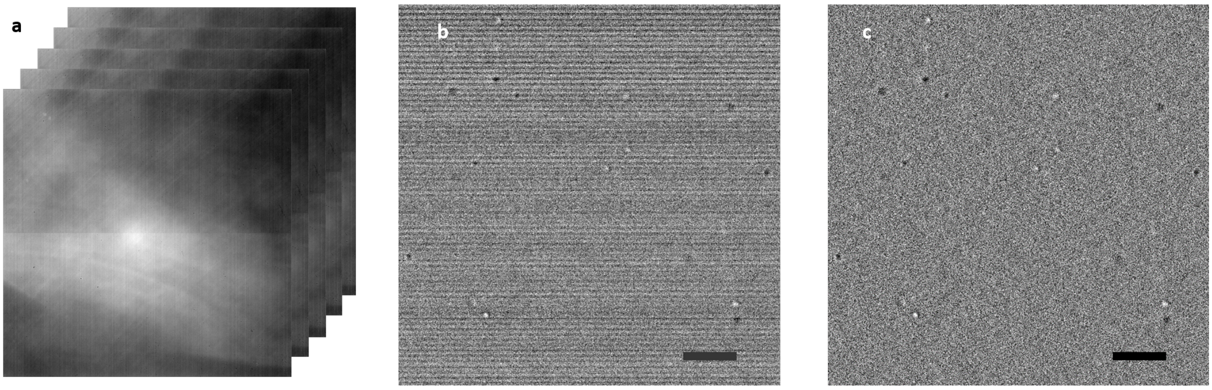

Figure 2.3: **Static background removal and image denoising**. **a** shows stack of direct raw images, **b** represents a frame after subtraction of the static background using temporal average frame, here the bright and dark spots designate nanoparticles of SiO_2 of 100nm in diameter, and **c** shows the frame **b** after removing the stripes artifacts in the Fourier domain, scale bar 5 μm.

In brief, the processing of the acquired images transforms raw data to ideally shot limited noise images containing limited diffraction spots analogous to data acquired under the state of the art of single-molecule localization fluorescence microscopy. Hence, decades of research and development of algorithms for spots detection, localization, and tracking can be transferred simply to be applied to dynamic interferometry techniques.

In our case, nanoparticles are the only moving particles in the solution. Here a median filter is efficient to eliminate the background. Nonetheless, when conducting this type of biological structure, a sliding temporal average window is usually used to remove signals coming from the slow dynamics compared to the high dynamics originating from the scatterers of interest.

2.3.2 Single particle tracking algorithm

Single spot detection

The step consists of recognizing the diffraction-limited spots corresponding to the signal of particle of interest . Eventhough the background noise is homogeneous it consists of fluctuation related to the shot noise. Each image is then filtered using a Gaussian kernel having an FWHM similar to the spot size. This artificial filtering reduces the background noise and increases the SNR. The next step applies an intensity threshold value and retrieves clusters of pixels dispersed in each image. Next, a sliding block (size comparable to the PSF spot) scans each image to find the local maximum pixel value compared to the neighboring pixels. Here, we find the position of the maximum value pixel-intensity per cluster [5].

Sub-pixel localization

Once the position of local pixel maxima is found, the sub-pixel position of the candidate can be estimated using different approaches:

The use of an elliptical Gaussian fit is widely used to find the properties of the spot. It is particularly useful in the 3D localization of single molecules in fluorescence microscopy. When interested in the 2D movement only, an elliptical shape can be useful to take into account the elongation of the spot due to the particle's movement during the camera's exposure time. the fit can be expressed as:

$$G(x,y) = Ce^{-\frac{1}{2}(\frac{x-x_0}{s_x})^2} e^{-\frac{1}{2}(\frac{y-y_0}{s_y})^2} + B \tag{2.12}$$

Where, x_0, y_0 and the amplitude C, s_x and s_y are the widths in the axis x and y respectively, B represents the background offset.

For a short exposure time of the camera, The movement of the particle of interest can be neglected. However, for long exposure time, the shape of the PSF is affected by the movement of the particle and therefore a Gaussian fit is usually used and can be written as:

$$G(x,y) = Ce^{-\frac{1}{2}(\frac{(x-x_0)+(y-y_0)}{s})^2} + B \tag{2.13}$$

where s is the the gaussian width of the spots.

These parameters can be retrieved using an iterative approach such as non-linear least square fit. Other methods are based reduce the number of iterative approach have been used for in fluorescence microscopy such as center of the center of gravity of the pixels forming the clusters [6] or the radial symmetry centers [7].

The performances of all these techniques are comparable. Yet each technique can have some advantages compared to the others in terms of processing time or accuracy.

Trajectory linking

Once the spatial position of single scatters is found, the next step is finding the temporal agreement to form trajectories. The most trivial approach used is searching for the nearest neighbor between 2 frames. This approach was proved to be efficient when having a small number of particles in the field of view and the trajectories do not overlap between them [8]. Multiple hypothesis tracking (MHT) algorithms showed some better accuracy compared to other methods. However, they are usually expensive in terms of computation and time processing. Hypotheses for each candidate target provide a systematic solution to the data association problem. The likelihood of each track is calculated, and the most likely combination of tracks is selected. MHT is ideal for exploiting higher-order information such as long-term motion and appearance models since the entire track hypothesis can be considered when computing the likelihood [9, 10]

Machine learning algorithms have been employed in the detection and tracking process. Although these algorithms need to be trained with simulated and real data, the training process can be long, the use of the trained network to detect particles is fast [11, 12]. The detection performance depends on the training data, the training process, and the network's architecture in use.

Despite the potential of deep learning approaches, in this work, we used classical methods since they can be adapted easily for the modification of the optical setup.

Multiple-target tracing algorithm

We have used the multiple-target tracing algorithm to process the single-particle data in the manuscript [13]. This algorithm is developed to detect the spatio-temporal evolution of fluorescence labels. In brief, a block scans the image frame and checks for a particle's presence, thanks to a ratio test of likelihood by comparing the block region to the case of a simulated PSF depending on the initial input parameters of detection. In this algorithm, the signal to noise ratio is calculated in decibel, comparing the total intensity of the PSF spot to the standard deviation of the background noise,σ.

The last step, reconnecting the positions between the images, is the most difficult, mainly because of the blinking of fluorophores. To best achieve this, Multiple-target tracing algorithm (MTT) takes three parameters into account each time. 1) fluorescence intensity (which considers blinking fluorophores by a law of probability). 2) the possible disappearance of the particle (zero intensity or exit from the volume of detection, based on a certain number of consecutive absences of the particles (off time value). 3) The instantaneous diffusion coefficient of the particle. These parameters are compared with those determined for the previous images on a retrograde period (in number of images). This comparison is important, especially if many fluorophores are nearby. This is why the algorithm considers the maximum diffusion coefficient chosen by the user. Each particle position is compared to the position in the previous frame. If many fluorophores are detected in the same search area, then the final reconnection decision corresponds to the best combination that best satisfies the previously stated parameters and its history.

Again, we would like to mention that this software was developed initially for fluorescence single-particle localization and tracking. We then modified the original code written on Matlab to localize bright and dark spots in two successive steps. Then all the spots are considered indifferently for the tracking part of the code. Few differences are presented here: we used the OFF time to consider the case where the phase shift near to the focal plane of the objective lens is small, and the signal of interest cannot be distinguished from background noise or the case when the particle gets out of the volume of observation. Optimizing all the detection and tracking parameters has been done using particles of known size and the distribution size of particles, trajectory traces of SiO_2 particles of 100nm in diameter are presented in fig 2.4.

We mention that images are acquired at a usual speed of 500 fps, during one second or few seconds. Hence, we are not affected by mechanical or thermal drifts for these short acquisition time, and there is no need for post-processing correction related to these drifts.

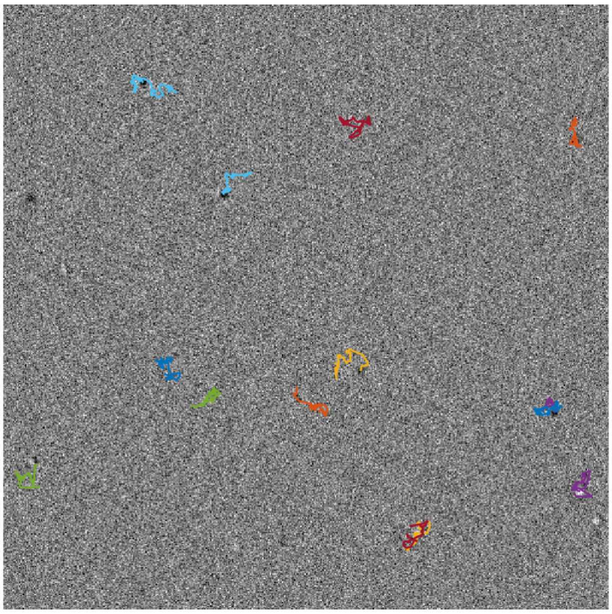

Figure 2.4: **Single trajectories of SiO_2,100nm nanoparticles in water**

2.4 Analysis of single-particle diffusion

All the measurements in this and the following chapter were performed in a water or water-like solution. By analyzing the trajectories resulting from the tracking algorithm, we retrieve some information concerning the diffusion characteristics of the particles in the solution. Here, we distinguish between two different approaches, an ensemble approach in which all the particles are considered identically in the analysis and the second approach based on analyzing each trajectory individually. Both of these approaches aim to estimate the diffusion coefficient of the particles. The diffusion coefficient of a spherical particle can be written as:

$$\mathrm{D} = \frac{1}{f}\mathrm{KT} \tag{2.14}$$

Where, f is the frictional coefficient, K is the Boltzman constant and T is the absolute temperature.

$$f = 6\pi\eta r \tag{2.15}$$

And η represents the liquid viscosity and r is the hydrodynamic radius of the particle.

2.4.1 Mean squared displacement

The simplest and most widely used approach is the mean squared displacement (MSD) analysis. The MSD curve allows the estimation of physical information such as the diffusion coefficient D of the particle and the diffusion regime of the particles.

We start first by presenting the localization error. Two sources of error affect this error when considering moving particles, these errors can be presented as the static and dynamic error;

therefore, the dynamic localization uncertainty is found to be [14]:

$$\sigma = \frac{s}{\sqrt{\mathrm{N}}} = \sigma_0 \sqrt{1 + \frac{\tilde{\mathrm{D}} t_{\mathrm{E}}}{s_0^2}} \tag{2.16}$$

where, s is the width of the spot, N is the number of photons, σ_0 is the localization error for a fixed particle, $\tilde{\mathrm{D}}$ is the diffusion coefficient of the particle, t_{E} is the exposure time of the camera and s_0 is the width of a not moving spot.

Real displacements can be defined for any values of the time lag, while the number of possibilities is limited to multiple of the frame duration t in the case of the observed trajectory. In the absence of any anisotropic medium properties. In a 2D movement, the diffusion can be described by the probability distribution of the displacement d as [14]:

$$\mathrm{P}_{\tilde{d}}(u) = \frac{2u}{4\tilde{\mathrm{D}} t} \exp\left(-\frac{u^2}{4\tilde{\mathrm{D}} t}\right) \tag{2.17}$$

Therefore, we considering the Gaussian error representing the localization error, the probability density function of the displacement can be written as:

$$\mathrm{P}_{\tilde{d}}(u) = \frac{2u}{4\tilde{\mathrm{D}} t + \epsilon} \exp\left(-\frac{u^2}{4\tilde{\mathrm{D}} t + \epsilon}\right) \tag{2.18}$$

Where t is the duration of the displacement or time lag between positions and u is the jump size, represents the mean diffusion coefficient and the error can be written as: $\epsilon = 4\sigma^2$ [14].

The mean squared displacement expressed in equ 2.19

$$\langle d^2(t) \rangle = \epsilon + 4\tilde{\mathrm{D}} t \tag{2.19}$$

In practice, for the single trajectories and the ensemble of trajectories analysis, we rely on the histogram of the jump, the displacement at different lags of time. We, therefore, estimate a diffusion coefficient by fitting the cumulative distribution function (CDF) of the histogram of displacement at a different lag of time using the linear least square fit method as presented in fig.2.5(a-f). Here instead of fitting the histogram directly, we fit the cumulative distribution function of the displacement. In fact, the cumulative distribution function can be less sensitive to the local fluctuations, (equ2.20).

$$\mathrm{CDF}_d(u) = 1 - e^{\frac{-u^2}{4\tilde{\mathrm{D}} t}} \tag{2.20}$$

Instantaneous diffusion coefficients corresponding to different lags of time can be estimated using the cumulative distribution function of jump size. In other words, the instantaneous estimated diffusion coefficient are used to retrieve the mean sqaured displacement using data points at different lags of time, (fig 2.6, a). Hence, a global diffusion coefficient can be found by fitting the mean squared displacement curve using a linear fitting function $y = ax + b$ where $a = 4\mathrm{D}$ and $b = 4\sigma^2$. We therefore fit the MSD curve between the second and the first 25th percent of the data points[15]. Similarly, the processing presented

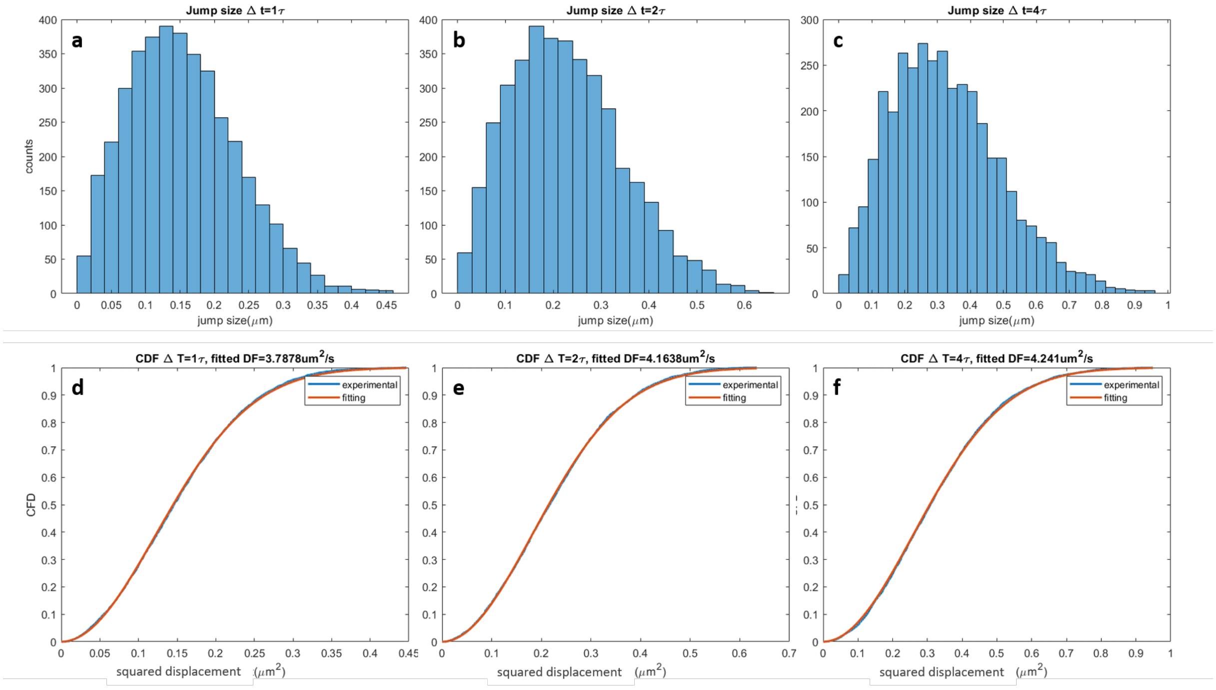

Figure 2.5: **Histograms and cumulative distribution function of the jump size of SiO$_2$100nm at different lag of time**. **a, b and c** show the histogram of jump size in for a lag of time of 2, 4 and 6ms respectively. **d,e,f** represent the cumulative distribution function of the jump size at 2, 4 and 6ms.

for the ensemble of tracked particles can be applied for individual particles to estimate an MSD curve (fig2.6,b). For a single homogeneous population of particles in the sample, the ensemble analysis is equivalent to single trajectories' analysis. When different particles are presented in the sample solution, single trajectory analysis allows one to retrieve individual information about each particle.

Diffusion regime: logarithmic fitting of the MSD

Furthermore, the MSD curve contains information about the diffusion regime of the particles of interest. If the particles abnormalities in Brownian motion can be classified according to the time-dependent variations in the distribution of particle displacements; a property caught by means of larger displacements than expected from random motion, the observed behavior begins to be directional. A sub-diffusion behavior is then estimated if smaller displacements are estimated compared to the normal Brownian motion displacement. Furthermore, if the MSD presents an asymptotically stable behavior as a function of time, the diffusion can be described as confined. The difference in diffusion regime can be attributed to a β parameter affecting the MSD curve, (equ 2.22). The derivation of the normal behavior can be detected easier for high lags of time. The derivation parameter is therefore estimated when fitting the MSD in a logarithmic scale as, (equ 2.22):

$$\langle d^2(t)\rangle = (\epsilon + 4\tilde{D}t)^{\beta} \tag{2.21}$$

$$\log(\mathrm{MSD}) = \mathrm{K}_1 + \beta \log t \tag{2.22}$$

And K_1 is a constant value.

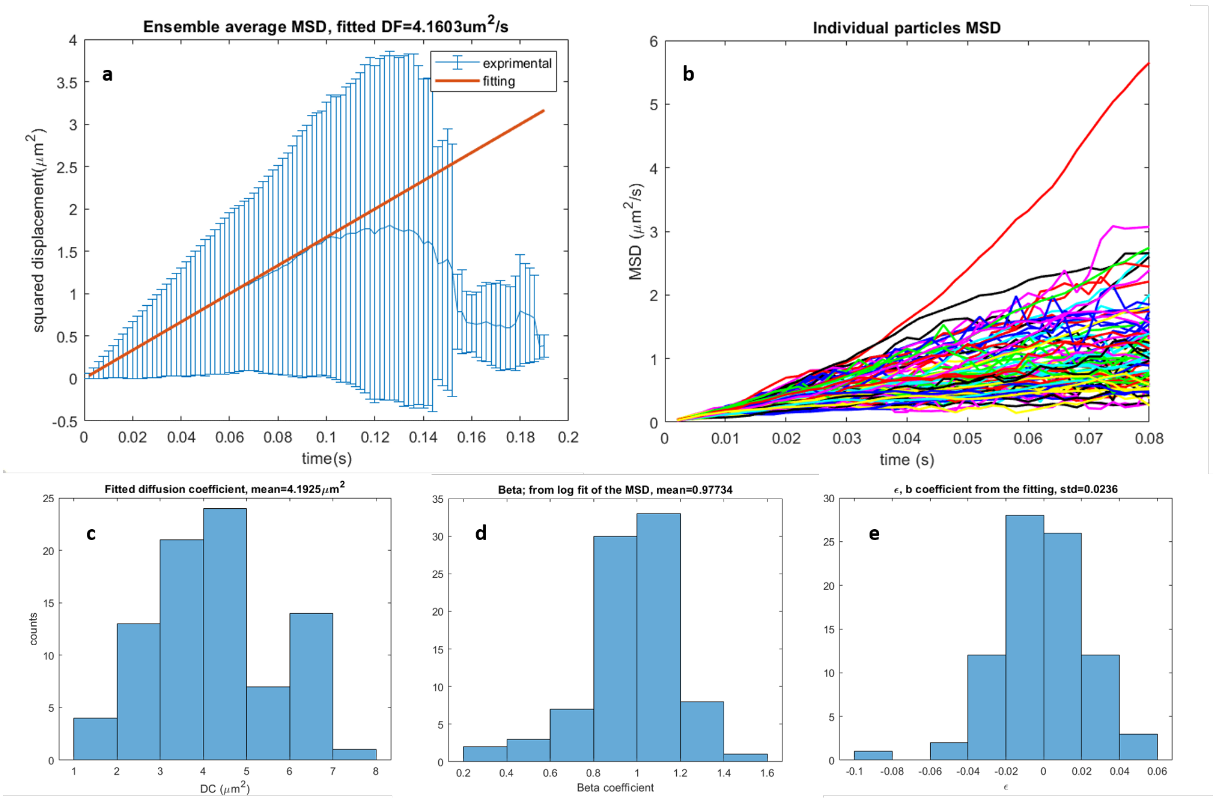

Figure 2.6: **Ensemble and individual diffusion analysis using MSD curves of $Si O_2$, 100nm in diameter a** shows the ensemble average MSD curve and the linear fitting, the fitted diffusion coefficient=4.16 $\mu m^2/s$. **b** represents the individual MSD curves. **c,d,e** represent histograms of the estimated diffusion coefficient (mean= 4.19$\mu m^2/s$),β coefficient (mean value= 0.977) and b coefficient of the fitted curve representing the localization error (standard deviation= 0.023), repectively.

We would like to note that many approaches have been developed to monitor the variation of the diffusion regime in biological samples using more sophisticated algorithms [11, 16]. Here we limit the analysis to the average diffusion coefficient of the ensemble of trajectories and individual trajectories resulting from the MSD. However, a verification step is considered by comparing the displacement histogram at different lags of time normalized by the square root of lag of time. Here, an abnormal diffusion behavior can be detected by an increasing shift of the maximum position for larger lags of time.

Let us mention that displacement histograms have been used in fluorescence [16, 17] to estimate the ratio of different populations of particles having different diffusion properties $\frac{\mathrm{A}}{\mathrm{B}}$, by fitting the CDF $(1 - \mathrm{A}e^{-x1} - \mathrm{B}e^{-x2})$ in the sample; where A and B represent the ratio of each population in the sample solution. However, this type of analysis can be more complicated to apply in interferometric scattering microscopy since the trajectory length of each particle depends on the interferometric signal and its diffusion properties.

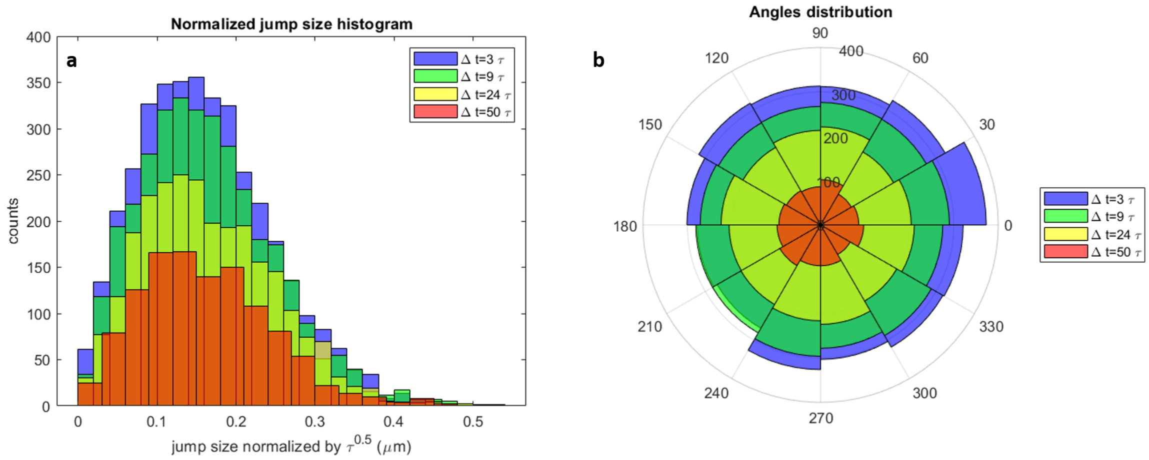

Figure 2.7: **Histogram of jump size and angle distribution of** SiO_2**, 100nm at different lags of time**

Angle orientation of single particles

In an analogous way to the displacement histogram, the histogram of angles between the vector position of the spots can reveal some information about how a spot discovers its surrounding. A normal Brownian motion can be seen for an isotropic distribution of the angles in a 2π interval (fig2.7). However, a biased, directive diffusion can be seen when privileging some angles in the 2π interval[17].

2.4.2 Diffusion coefficient of SiO_2 nanoparticles

We study the diffusion coefficient properties of SiO_2 nanoparticles having 50, 100, and 200 nm in diameter. We want to note that we use SiO_2 nanoparticles, mainly because of their refractive index similar to viruses and biological samples.

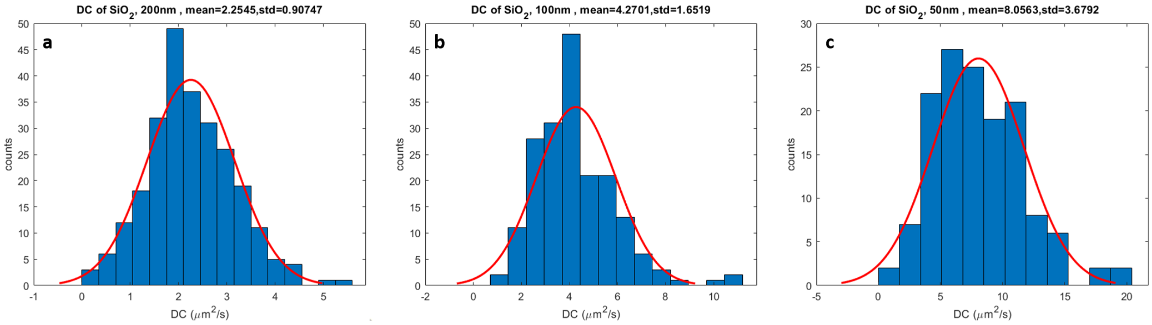

Figure 2.8: **Estimated diffusion coefficient histograms of** SiO_2 **nanoparticles**. **a, b and c** show the histograms of the estimated diffusion coefficient resulting from single trajectories analysis for SiO_2 nanoparticles of 200, 100 and 50nm respectively

The estimated diffusion coefficient increases when using smaller nanoparticles which confirms the theoretical formula 2.14. A mean diffusion coefficient of 2.25, 4.27, and 8.05 $\mu m^2/s$ is found for SiO_2 nanoparticles of 200, 100 and 50 nanometer respectively, the histogram distrubtion of the diffusion coefficient is presented in fig 2.8. However, the standard deviation of the diffusion coefficient increases inversely proportional to the size of the particles. This behavior is attributed to the SNR ratio and the diffusivity of the particles. Smaller particles faster out of the volume of detection. Furthermore, the SNR ratio defines the ability to distinguish the particles of interest from the background. Therefore, this task gets for weaker intensities from small particles. These standard deviations are relatively high compared to the dispersion of the size of particles indicated by the manufacturer (less than 5% for each solution) [Silica Microspheres, Polysciences, USA].

2.5 Interferometric intensity single trajectories

As presented in the first part of this chapter, the interferometric signal is affected by the phase induced by the objective lens. For a particle moving in a solution sample, the intensity depends on the axial position of the particle regarding the focal plane of the objective lens. Here, the spots consist of altering bright and dark spots, depending on the axial position of the particle that affects the phase of the scattered beam. The intensity parameter has a particular value in interferometric scattering microscopy because it embodies the difference of refractive index between the particle and the surrounding medium, and it also depends on the size of the particle.

Here, we attribute an intensity value to each trajectory. This value consists of the maximum absolute value of the intensities found during each trajectory. Doing so, we assume that the intensity profile is symmetric for bright and dark spots for both sides of the focal plane, as explained previously in this chapter. The variation of the interferometric intensity will be explained in chapter 4.

In our set-up working in a transmission configuration, the alteration between dark and bright spots occurs mainly when crossing the focal plane for dielectric non-metallic particles. The maximum and minimum of intensity are therefore shifted from the focal plane of the objective lens. Furthermore, the same approach can be considered for metallic particles and particles having some plasmonic resonance, such as gold nanoparticles. Here the phase shift is affected by the phase shift induced by the particle in addition to the phase shift due to the objective lens.

Thus, the interferometric intensity alters depending on the axial position of the particle of interest. This property allows the relative positioning axially. For the detection of single nanoparticles in a solution sample, we are interested in the absolute maximum intensity of a particle during its trajectory. Yet, tracking the 3D position of the particle can be done based on the intensity and shape of the PSF can be intersting for studying biological structures [18].

The interferometric intensity scales non-linearly with the size of the nanoparticles following Rayleigh regime. A visual inspection is presented in fig2.9(a,b,c). The variation of the interferometric intensity for different size of particles is shown in fig2.9(d). Here, we applied a gaussian fit for each population of particles; mean values of (38, 111, 242) and standard deviation of (5.04, 10.67, 11.93) are estimated for particles of 50, 100, and 200nm, respectively. Measured intensities represent the total intensity of the spot and are measured in arbitrary units (A.U.).

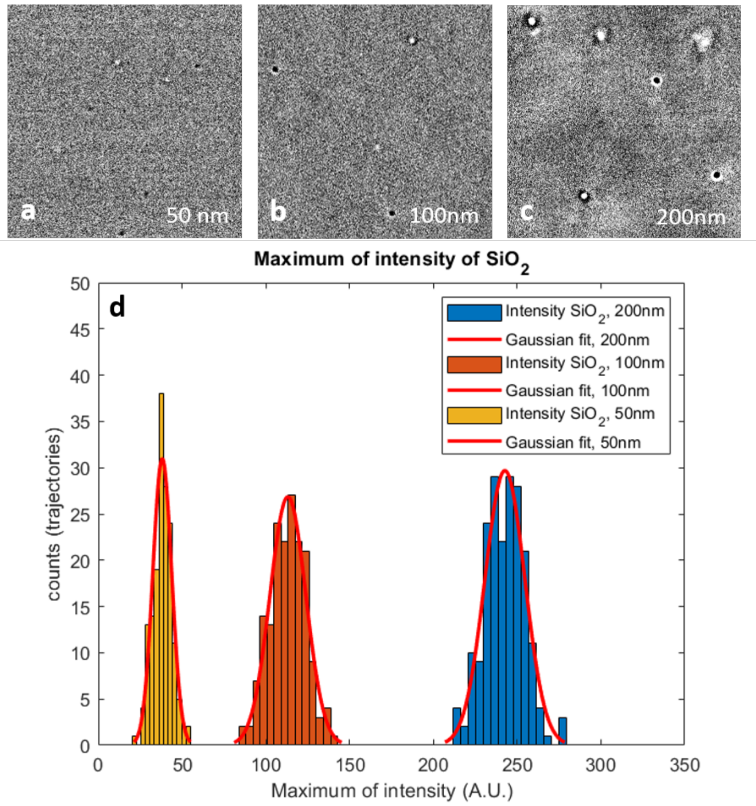

Figure 2.9: **Interferometric detected spots images and histogram of maximum of intensity in each trajectories of different size of SiO_2 nanoparticles**. **a, b and c** show a frame image of beads of 50, 100 and 200 nm in diameter of SiO_2. **d** represents the histogram of the maximum of absolute intensity per trajectory for different size of particles

We would simply add that despite that we have been able to distinguish between different sizes of same refractive index particles, the intensity did not scale as expected by the radiation patterns of the particles, as presented in section 1.1.

We will get into the details of the interferometric PSF in chapter4 in this manuscript.

2.6 Volume of detection and normalization

This section discusses the observation volume for better quantification of the concentration of nanoparticles in a solution.

By analogy to fluorescence methods, the SNR depends on the fluorophores and the number of molecules labeling the target of interest in fluorescence methods. However, for the interferometric PSFs, the observation volume depends on the particles' optical and diffusion properties. Therefore, smaller particles will be observed in a smaller detection volume compared to the bigger particles having similar optical properties. Bigger particles will then have a higher interferometric contrast that makes them detectable when moving further from the focal plane.

As presented in the previous section, the interferometric signal depends on the optical and diffusion properties of the particles. Yet, interferometric SNR is different from single-molecule tracking using fluorescence microscopy, where the intensity depends mainly on the fluorescent label and the number of fluorophores labeling the target. Here, we have to consider the SNR related to the optical properties of the nanoparticle of interest and the movement of the particles (a smaller particle explores a more significant volume). Therefore, small particles are observed in a smaller volume of detection than bigger particles having similar optical properties.

Knowing the detection volume is convenient to estimate the concentration of particles in the solution sample. Here, we rely on each particle's trajectory's length (in time) to calibrate the individual volume of observation, by relying on the axial variation of the interferometric intensity. Once the diffusion coefficient is estimated using the approaches presented before, we can approximate the average z displacement of the particle during the interval of time corresponding to the number of tracked frames. In a similar way to (equ2.19) the MSD can be generally expressed as:

$$\langle d^2(t)\rangle = 2dim\tilde{\mathrm{D}}t \tag{2.23}$$

where dim is the dimensionality of the system. In one dimension along the z axis, MSD = $\langle d^2(t)\rangle = 2d\tilde{\mathrm{D}}t$. Therefore, the average displacement, d can be written as $\langle d(t)\rangle = \sqrt{2dim\tilde{\mathrm{D}}t}$. For our measurements, the time interval between 2 consecutive frames is 2ms. Thus we normalize the volume of detection regarding the $\sqrt{}(\mathrm{N}_t)$, where N_t is the trajectory time length including the OFF time frames.

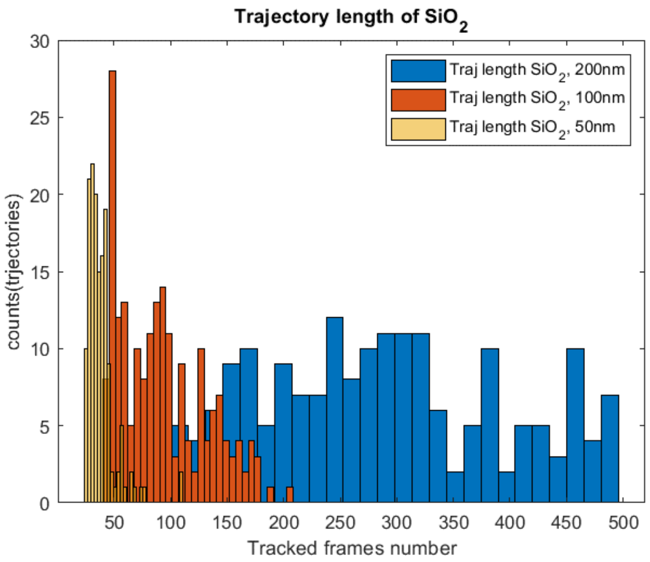

Figure 2.10: **Trajectories length distribution of different size of SiO_2 nanoparticles.**

We show in fig2.10 the histogram distribution of trajectories length for SiO_2 nanoparticles of 50, 100, and 200 nm in diameter with a mean value of 38.7, 92.3, and 273.3 frames, respectively. Using this parameter, we can retrieve the estimated displacement along the Z-axis using the diffusion coefficients values in section**??** as well as the square root of the trajectory length. Therefore, the means displacements of 1.11, 1.256 and 1.568 μm along the axial direction have been found for SiO_2 of 50, 100 and 200nm, respectively.

This analysis allows to retrive the volume of observation of different particles and thus estimate the concentration of particles in the solution sample.

2.7 Number of tracked data point particles and challenges

We investigated the statistical distribution of the diffusion coefficient value of the tracked particles and check the influence of the number of data points on the confidence interval of the measurements. Therefore, we estimate the variation of the mean value depending on the number of tracked particles going to the total number of tracked particles. Here, we show the plot of the mean value and the standard derivation of the diffusion coefficient as a function of the sampling for SiO_2, 100nm. For each number of observations,k samples are chosen randomly without replacement.

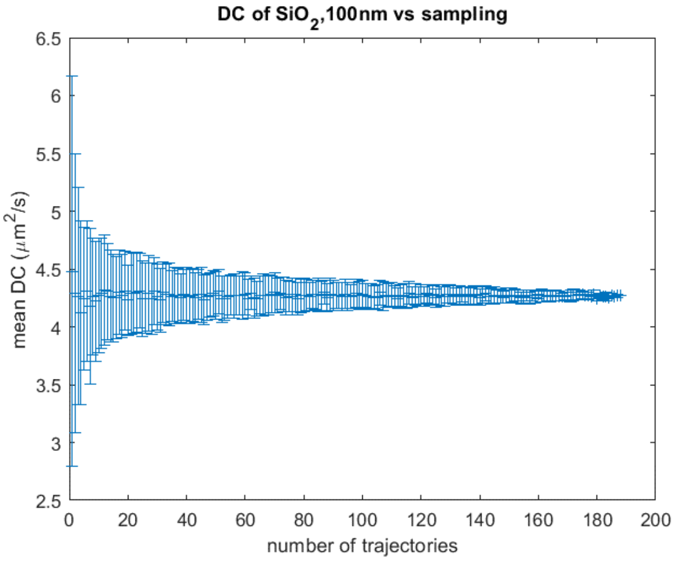

Figure 2.11: **Mean value of the estimated diffusion coefficient as a function of sampling SiO_2 nanoparticles**.

We notice in fig 2.11 that the mean value gets stable with a relatively low number of tracked particles. However, the standard deviation of the distribution of the estimated diffusion coefficient is relatively high (1.65 for 188 tracked particles). Here, this number depends directly on the signal-to-noise ratio of the particles. An artificial way to increase the precision is to analyze long trajectories. Thus, we have to compromise between the number of tracked particles and the measurement uncertainty when estimating the diffusion coefficient. We can see that the average value of the diffusion coefficient is stable even for very few tracked trajectories. The standard deviation of the estimated diffusion coefficient depends on the dispersion of nanoparticles in the sample, the tracking parameters, the size, and the SNR of the nanoparticles.

In this work, we did not get into the details of detection and tracking parameters. Choosing the detection and tracking parameters is not trivial. A visual inspection and calibration using a specific particle size are needed to choose the tracking parameters efficiently. Therefore, working with low particle concentration can be efficient for linking trajectories, and a minimum number of tracked particles is needed for a reasonable estimation of the mean diffusion coefficient (fig 2.11). In practice, for specific tracking parameters, using a relatively low threshold of detection, we have been able to detect particles of 50 nm of SiO_2 in a sample having a concentration of $5 * 10^7$ particles/mL for an acquisition of 500 frames at 500 FPS. Let us note that lower concentrations can be used to detect bigger particles of SiO_2

Bibliography

[1] Jerome Mertz. *Introduction to optical microscopy*. Cambridge University Press, 2019. 26

[2] Simin Feng and Herbert G Winful. Physical origin of the gouy phase shift. *Optics letters*, 26(8):485–487, 2001. 27

[3] Martine Boccara, Yasmina Fedala, Catherine Venien Bryan, Marc Bailly-Bechet, Chris Bowler, and Albert Claude Boccara. Full-field interferometry for counting and differentiating aquatic biotic nanoparticles: from laboratory to tara oceans. *Biomedical optics express*, 7(9):3736–3746, 2016. 28

[4] J Scholler. Ffoct control and acquisition software. 2019. 29

[5] John C Crocker and David G Grier. Methods of digital video microscopy for colloidal studies. *Journal of colloid and interface science*, 179(1):298–310, 1996. 31

[6] Hao Shen, Lawrence J Tauzin, Rashad Baiyasi, Wenxiao Wang, Nicholas Moringo, Bo Shuang, and Christy F Landes. Single particle tracking: from theory to biophysical applications. *Chemical reviews*, 117(11):7331–7376, 2017. 32

[7] Raghuveer Parthasarathy. Rapid, accurate particle tracking by calculation of radial symmetry centers. *Nature methods*, 9(7):724–726, 2012. 32

[8] Ulrike Endesfelder, Sebastian Malkusch, Franziska Fricke, and Mike Heilemann. A simple method to estimate the average localization precision of a single-molecule localization microscopy experiment. *Histochemistry and cell biology*, 141(6):629–638, 2014. 32

[9] Ingemar J. Cox and Sunita L. Hingorani. An efficient implementation of reid's multiple hypothesis tracking algorithm and its evaluation for the purpose of visual tracking. *IEEE Transactions on pattern analysis and machine intelligence*, 18(2):138–150, 1996. 32

[10] Khuloud Jaqaman, Dinah Loerke, Marcel Mettlen, Hirotaka Kuwata, Sergio Grinstein, Sandra L Schmid, and Gaudenz Danuser. Robust single-particle tracking in live-cell time-lapse sequences. *Nature methods*, 5(8):695–702, 2008. 32

[11] Lucas von Chamier, Romain F Laine, Johanna Jukkala, Christoph Spahn, Daniel Krentzel, Elias Nehme, Martina Lerche, Sara Hernández-Pérez, Pieta K Mattila, Eleni Karinou, et al. Democratising deep learning for microscopy with zerocostdl4mic. *Nature communications*, 12(1):1–18, 2021. 33, 37

[12] Saga Helgadottir, Aykut Argun, and Giovanni Volpe. Digital video microscopy enhanced by deep learning. *Optica*, 6(4):506–513, 2019. 33

[13] Arnauld Sergé, Nicolas Bertaux, Hervé Rigneault, and Didier Marguet. Dynamic multiple-target tracing to probe spatiotemporal cartography of cell membranes. *Nature methods*, 5(8):687–694, 2008. 33

[14] Xavier Michalet. Mean square displacement analysis of single-particle trajectories with localization error: Brownian motion in an isotropic medium. *Physical Review E*, 82(4):041914, 2010. 35

[15] Xavier Michalet and Andrew J Berglund. Optimal diffusion coefficient estimation in single-particle tracking. *Physical Review E*, 85(6):061916, 2012. 35

[16] Anders S Hansen, Maxime Woringer, Jonathan B Grimm, Luke D Lavis, Robert Tjian, and Xavier Darzacq. Robust model-based analysis of single-particle tracking experiments with spot-on. *Elife*, 7:e33125, 2018. 37

[17] Ignacio Izeddin, Vincent Récamier, Lana Bosanac, Ibrahim I Cissé, Lydia Boudarene, Claire Dugast-Darzacq, Florence Proux, Olivier Bénichou, Raphaël Voituriez, Olivier Bensaude, et al. Single-molecule tracking in live cells reveals distinct target-search strategies of transcription factors in the nucleus. *Elife*, 3:e02230, 2014. 37, 38

[18] Reza Gholami Mahmoodabadi, Richard W Taylor, Martin Kaller, Susann Spindler, Mahdi Mazaheri, Kiarash Kasaian, and Vahid Sandoghdar. Point spread function in interferometric scattering microscopy (iscat). part i: aberrations in defocusing and axial localization. *Optics Express*, 28(18):25969–25988, 2020. 39

Chapter 3

Label-free virus-antibody interaction monitoring in real-time by common-path interferometry

Contents

During the many months of lockdown imposed by COVID-19, access to the lab was forbidden, then significantly reduced in the following months. Therefore, I proposed following the evolution of the diffusivity of nanoparticles to follow the virus-antigen interactions for potential diagnostics applications. To carry out this experimental study, I benefited from the help of Martine Boccara to obtain support and the viruses and antibodies necessary for this proof of concept. Ignacio Izeddin and Claude Boccara helped to achieve a relevant statistical analysis of the data get quantitative parameters.

This chapter uses a label-free, full-field, incoherently illuminated common path interferometric method to detect, track, and quantify biotic nanoparticles. This method combines the scattering level interferometric signal contrast of single particles to the diffusion mobility to follow the interaction between viruses and specific antibodies or non-purified serum. The first interactions occur after around one minute, and the recognition signature is detectable after minutes. In addition, we have been able to differentiate two populations of similar size of empty and full (encapsulating DNA) capsids of T5 in a heterogeneous solution demonstrating the robustness of this label-free detection approach. Furthermore, we estimated the affinity of the virus-antibodies reaction as well as an approximation of the rate equation of the interaction.

We would like to thank Pascale Boulanger (I2BC) for the samples of T5- bacteriophages and capsids samples and the corresponding antibodies, Paulo Tavares(I2BC) for SPP1 bacteriophages, and the corresponding serum. We also would like to thank Yves Gaudin and Aurélie Albertini(I2BC) for the VSV viruses and corresponding antibodies. Finally, we would like to thank Delphine Muriaux (IRIM) for the Virus-Like Particle samples (VLP).

A paper manuscript presenting this approach is in preparation to be submitted.

3.1 Methods for virus quantification

3.1.1 Usual methods for virus quantification

The ability to detect and characterize viruses rapidly and efficiently plays a crucial role in avoiding widespread global health issues. In fact, early detection of viruses helps provide targeted therapy, extends the treatment space, reduces morbidity, and limits the transmission of viruses. Therefore, there has been considerable interest in nanoparticle detection, especially in biomedical, pharmaceutical, and virus research, particularly improving testing and diagnostics. The current methods for virus detection can broadly be divided into three categories. Firstly, techniques based on measuring the infectivity as virus culture in eukaryotic cell lines. These cells represent a suitable host to be infected by the virus. An appropriate incubation period results in the formation of plaques, which can be fixed and stained for visualization. Note that the plaque assay is the standard gold method for quantifying infectious virus titer and can take up to several days[1]. Secondly, techniques that consist of examining the viral nucleic acid or protein of viruses include PCR (Polymerase Chain Reaction) amplification techniques or antigen-based tests. PCR techniques amplify a genetic sequence of interest to quantify its presence in the initial sample. It is known for its specificity; however, it takes up to a few hours to get the result[2] and yet virus quantification is not trivial. Antigen-based tests are used to detect specific viruses by looking for proteins on the surface of the virus related to the presence of the pathogen. In this type of test, the results can be obtained quickly, usually in tens of minutes [3]. However, These tests suffer a major issue of lack of sensitivity [4]. The third category relies on a direct count of virus particles, such as viral flow cytometry, which counts individual particles in the solution sample. The dynamic light scattering method is also used to estimate the average ensemble size of particles in solutions based on the diffusion coefficient of particles in the sample solution. Electronic microscopy techniques have been widely used to study the detailed morphology of viruses in terms of structure and composition [5]. Each technique has some primacy in specificity, sensibility, and sensitivity. However, they can be expensive in processing, equipment, or time.

Light microscopy presents a powerful tool to study biological samples; nevertheless, virus particles are quite small to be visualized directly with optical microscopy. This is due to their weakly scattering characteristics resulting from their small size and low refractive index compared to the surrounding medium. In terms of detection, the scattered intensity induced by the illumination of the particles scales with the sixth power of the particle size, which makes it indistinguishable from the background illumination due to the lack of contrast when detecting small NPs. In order to overcome this issue, fluorescence microscopy methods are usually employed. In these methods, the targeted molecules are labeled with fluorescent labels so that one can detect the molecule of interest without getting affected by the non-labeled background. Here, we note that fluorescent labels have been employed in tagging the capsid protein of viruses [6] or their viral genome DNA [7]. N. Robb et AL. reported a rapid virus detection method requiring about one minute to detect a result, in which calcium labeling has been used to track the mobility of viruses when interacting with specific antibodies [8]. Despite that fluorescent techniques are precise, the user has to adapt the labeling and excitation and the emission of fluorescent labels depending on the set-up. Also, fluorescence labels suffer from phototoxicity, photobleaching, photostability, and saturation.

Highly sensitive optical interferometric microscopy techniques are an added value to optical microscopy due to their conception based on interferometry signal amplification. Even though the intensity scattered from small particles is very weak compared to the illumination light, the concept of interference makes the detection of nano-size particles achievable with a camera-based detector. Different interferometric microscopy configurations have been developed to detect, identify and track small particles, molecules, metallic particles, and other materials in a wide range of domains [9, 10]. Highly sensitive optical interferometric microscopy techniques are an added value to optical microscopy due to their conception based on interferometry signal amplification. Even though the intensity scattered from small particles is very weak compared to the illumination light, the concept of interference makes the detection of nano-size particles achievable with a camera-based detector. Different interferometric microscopy configurations have been developed to detect, identify and track small particles, molecules, metallic particles, and other materials in a wide range of domains [9, 10]. In addition, these imaging methods have been used to characterize single particles and molecules in solutions[11]. However, the main drawback of label-free interferometric methods is the lack of specificity. Many groups tackled the specificity challenge in different ways. For example, the functionalization of surfaces and nonmaterial provides a means for targeting through selective binding to receptors at targeted sites [12]. Another example showing the ultra-high sensitivity is the ability to detect individual molecules through the change in light scattering at the interface when biomolecules (un)bind from said interface. This approach has been used to study the interactions between antibodies and the SARS-CoV-2 spike receptor, providing information on affinity, avidity, and cooperativity [13] and many other applications [14].

3.1.2 Principle of following virus-antibody interaction in a solution

In this chapter, we used the full field incoherent illuminated common path interferometer in transmission, described in the previous chapter 2, in order to detect, track and count viruses and vesicles in an aquatic environment. With this approach, the magnitude of the interferometric signal has been used in complement to single particle tracking analysis to distinguish between different populations of particles of similar size and distinct nature. Furthermore, we introduce a new approach to virus detection by adding specific antibodies to the simple solution containing the targeted virus. In this manner, we could monitor the interaction between viruses and antibodies molecules by tracking the modification of the diffusion mobility of particles and the interferometric contrast (see fig 3.1). This approach is demonstrated with purified IgG molecules anti pb8 with T5 phages and a non-purified serum-containing multiple antibodies anti-SPP1 and SPP1 phages. Despite the heterogeneity of particles in a non-purified serum, we could detect a recognition signature of the reaction of antibodies with antigens existing on the virus's outer surface in about 1 minute, and the aggregation is detected in a few minutes.

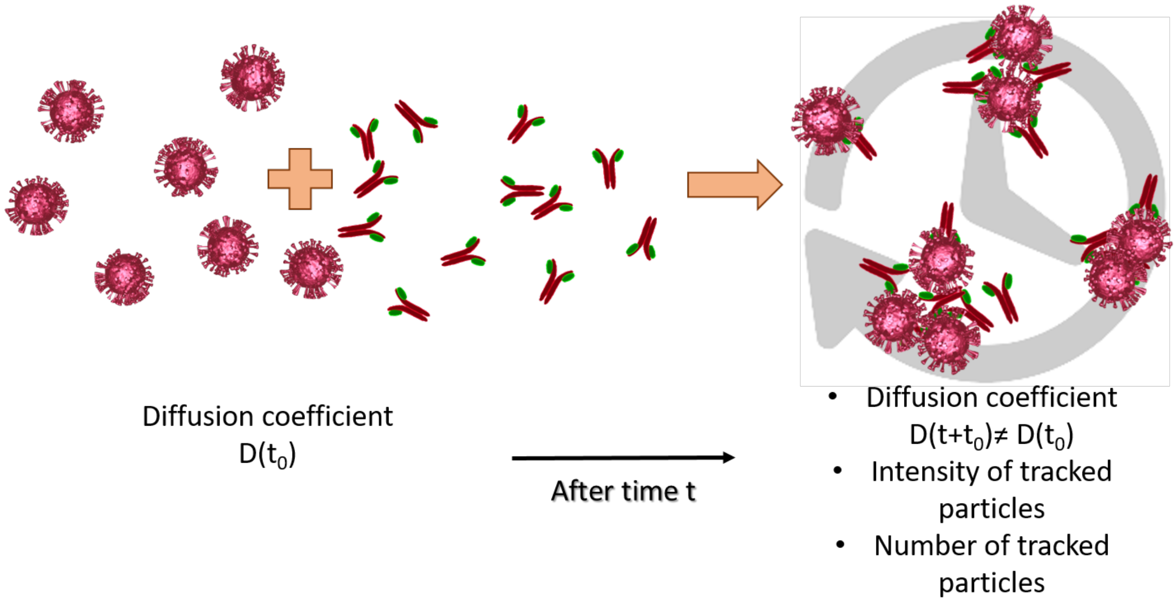

Figure 3.1: **Schematical representation of the reaction between viruses and antibodies in the solution sample**

3.2 Single-particle tracking analysis and interferometric signal contrast

The modality used in this chapter consists of tracking single biotic nanoparticles moving in the liquid sample to estimate the diffusion coefficient of the particles as well as the maximum intensity, as described in chapter 2.

3.2.1 Characterization of the size and internal structure of biotic nanoparticles

In brief, as described in the previous chapter, the interferometric intensity contrast depends mainly on the size and the refractive index of the particle of interest. However, the diffusion coefficient is estimated when tracking these particles. We would like to note that the diffusion depends on the hydrodynamic radius of the particle that is associated with the shape of the particle. Therefore, we aimed to detect and differentiate NPs of similar size and different nature. In particular, we aim to differentiate between capsids of T5 phage containing DNA inside of the particle and capsids of similar size lacking DNA. These two populations of particles have a similar size, and thus, their diffusion coefficient in a liquid solution is close. However, the refractive index of the Full capsids encapsulating DNA has a higher refractive index compared to capsids lacking DNA.

T5 capsids are characterized by their icosahedral geometry with an average size of 90nm in diameter. They are characterized by the lack of the infecting tail compared to a full T5 phage. We used two different types of capsids. Empty capsids, lacking DNA, with an initial concentration of 0.6 mg/mL (about $4*10^{13}$ heads/mL), and Full capsids, with the DNA inside of the capsid (or head), having an initial concentration of about 10^{12} heads/mL [15]. Cryo-Electron microscopy image is presented in fig3.2.

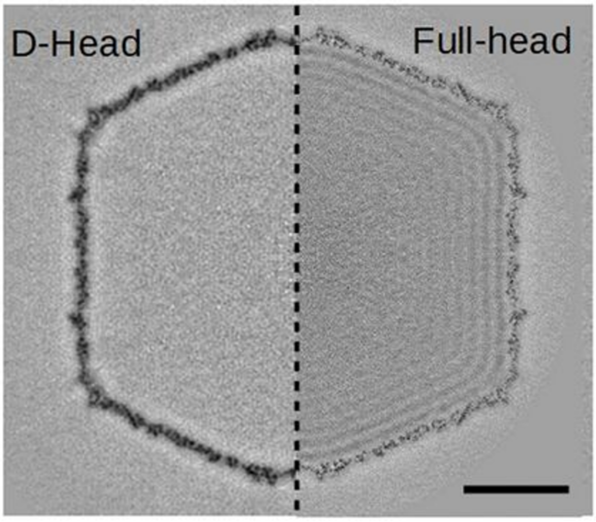

Figure 3.2: **Cryo- Electron microscopy image of empty mature capsids (D head) and full heads, scale bar= 1μm, image from [15]**

In order to characterize each population, we first acquire two stacks of 500 images at 500 FPS of a solution of empty capsids and full capsids of T5, respectively. A nominal concentration of 10^9 particles/mL was used for each acquisition. Each stack is processed separately in order to retrieve the diffusion characteristics of the particles as well as the interferometric signal.

A diffusion coefficient based on individual particles of 3.92±0.81 µm^2/s was estimated for 192 tracked empty T5-capsids compared to 4.03±0.98 µm^2/s which was estimated for 471 tracked full T5 capsids. Fig 3.3 represents the distribution of the estimated diffusion coefficient for both samples. The diffusion coefficient resulting from fitting the ensemble average MSD is represented in the plot of fig 3.3 (a), an ensemble diffusion coefficient of 3.89µm^2/s and 4.01µm^2/s have been found for empty and full capsids, respectively. A difference in interferometric intensity has been detected for two samples of capsids. The average intensity of 60.49±6.25(A.U.) is found for empty T5-capsids compared to a value of 86.38±9.68 (A.U.) for full capsids, as shown in fig3.3 (b). These results indicate that we can differentiate between full and empty capsids solutions using the interferometric signal despite the similarity in the diffusion properties. Furthermore, we noted a higher standard deviation when estimating the diffusion coefficient and the Interferometric signal, which indicates a larger dispersion of full capsids than empty capsids. This observation is previously confirmed based on the morphological study of the capsids using transmission electron microscopy [15].

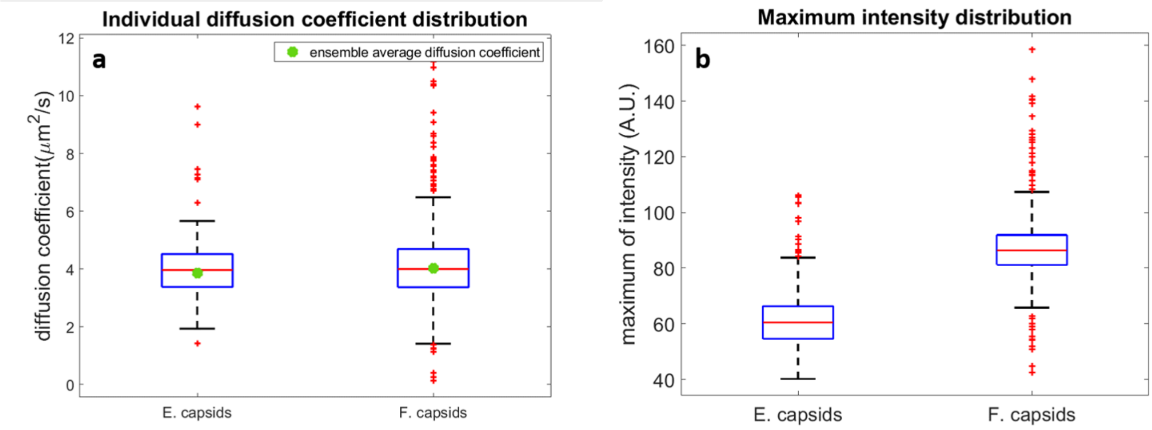

Figure 3.3: **Diffusion coefficient and interferometric intensity distribution of full and empty capsids**. Boxplot representations of; **a** the diffusion coefficient of individual/ ensemble of particles and **b** the estimated interferometric intensity for full and empty capsids of T5

We thereby use the same approach to distinguish between populations in a mixed sample of empty and full capsids of T5 with similar concentrations used before. As expected, we were not able to distinguish between the two populations in terms of diffusion coefficient, as shown in fig 3.4 (a). When fitting the histogram distribution of the diffusion coefficient with two Gaussian distributions using the least square error approach, we have seen a perfect overlap of the two curves. Here, we used a fitting with 2 Gaussians since two different populations are presented in the sample solution. However, in fig 3.4 (b), we distinguished two distinct populations using two gaussian fitting curves. The first is centered at 58.33 (A.U.), with an amplitude of 43.26 and a standard deviation of 8.11 (A.U.). The second population centered at 88.03 (A.U.) with a standard deviation of 9.75 (A.U.) and an amplitude of 101.63.

Consequently, the first population designates the population of empty capsids of T5 while the second population consists of Full capsids having higher intensity.

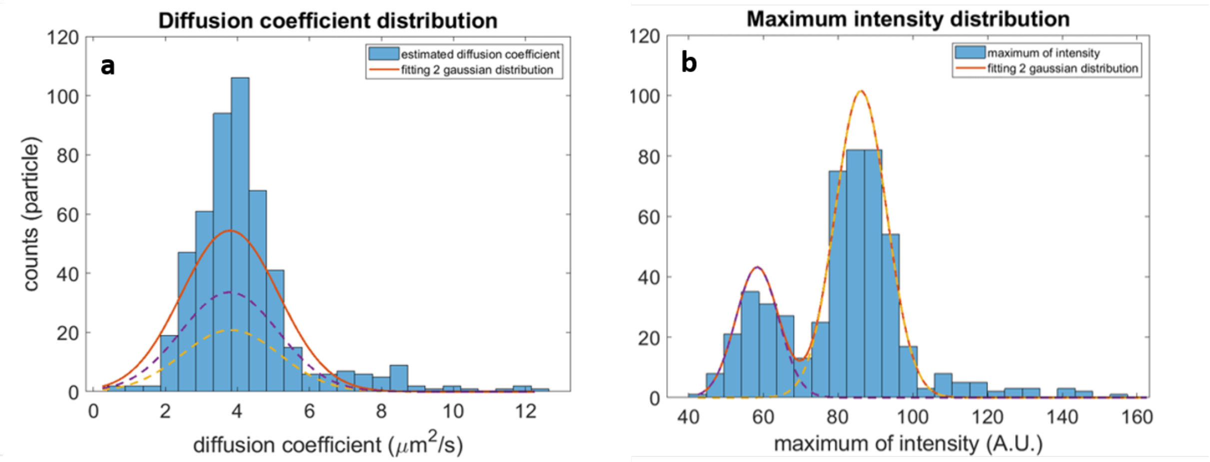

Figure 3.4: **Distribution of the diffusion coefficient and interferometric intensity of full and empty capsids in the sample solution**. **a** and **b** show the distribution of the individual diffusion coefficient and the interferometric intensity for full and empty capsids of T5 in the sample solution with two gaussian fittings, respectively

We would like to point out that full capsids are detectable in larger detection volumes because of their higher refractive index and the correlated larger signal-to-noise ratio. This allows us to probe particles further from the focus; indeed, we have been able to track more than two times full capsids compared to empty capsids of T5. The normalization of the detection volume can be estimated using the trajectory length of each tracked particles as presented in the previous chapter.

3.2.2 Monitoring virus-antibodies reaction

Antibody-antigen reaction is known to be a highly specific reaction. In this part of this chapter, we were interested in monitoring the reaction between T5 bacteriophages and purified IgG molecules.The concept relies on following the size of the particles in the solution. In case of recognition, free antibodies added into the solution will bind to the targeted protein on the outer surface of the virus, and thus, if the antibody can bind to two different viruses, significantly bigger particles will be detected in the solution. We have applied this approach using T5 bacteriophages.

T5 bacteriophages: consist of a capsid (90nm in diameter) containing DNA and a flexible tail (250 nm). The initial concentration is estimated to be 7.3 x10^{12}pfu/mL (PFU: plaque-forming unit) at the extremity of the tail where fibers are present on the tail, as seen in fig3.5. T5 capsids and phages are diluted in a T5 buffer solution whose composition is: 10mM Tris-Cl pH=7.4, 100mM NaCl, 1mM $MgCl_2$. **Purified IgG against T5 major capsid protein (pb8)** consists of polyclonal IgG targeting pb8 protein represented major capsid protein of T5 phages (800 sites/capsid), initial concentration 0.84 mg/mL. These samples have been prepared by Pascale Boulanger's group at I2BC.

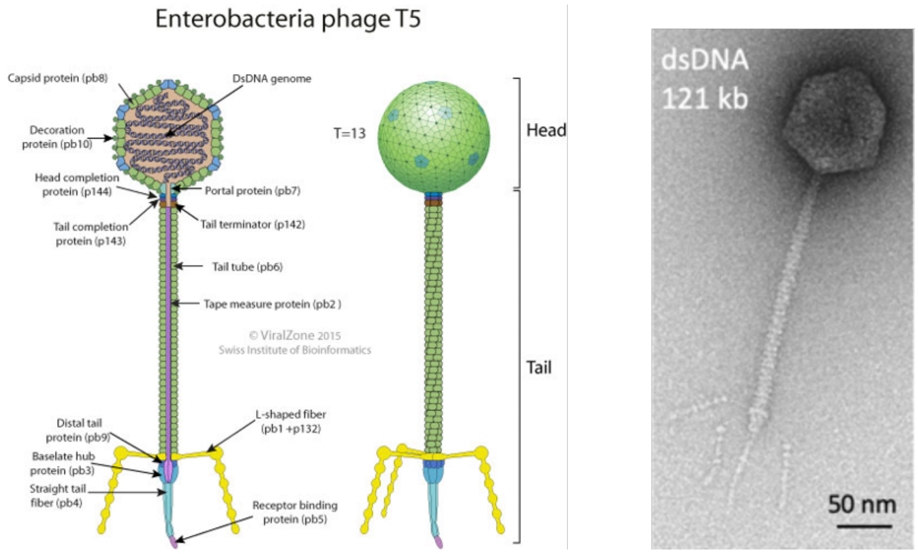

Figure 3.5: **Schematical representation and electron microscopy image of T5 bacteriophage [16]**

We first placed a 15 µL droplet containing purified polyclonal IgG molecules anti pb8 (major protein of the T5 capsid) in front of the objective lens, and then we added T5 phage to the IgG solution. For this test, we have an excess of IgG molecules (around 4×10^8 molecules of IgG to 2×10^6 PFU in a total volume of 16 µL).

Once having the objective lens dipped into the solution sample, we acquired stacks of 500 images at different time intervals on a binary logarithmic scale. We first performed the control tests, the first test contains the T5-phages only and the second control consists of antibodies only. Then, we perform the measurement when adding T5-phages to the sample solution containing the antibodies (IgG). Here, we would like to note that IgG molecules have a size of less than tens of nanometers. Thus these single molecules cannot be directly detected using our set-up.

At this stage, if we take a look at the direct images of these acquired data, we cannot see any difference. However, when removing the offset background of the images as described in chapter 2, we can see differences in the different tests as can be seen in fig 3.6 (a) and (b) processed images of the control T5-phages and the T5 phages in the presence of specific antibodies at different time intervals, respectively. The visual inspection of the T5 control does not reveal any significant differences. However, a progressive difference in terms of contrast, number of spots, and size of the detected spots could be visualized after adding T5 phages to antibodies solution.

In order to evaluate the interaction between antibodies and viruses, we have applied a single particle tracking approach to estimate the Diffusion coefficient and the interferometric intensity of single spots, presented in chap 2. A progressive decrease of the diffusion coefficient can be seen for the sample containing the IgG+T5 phages. A Diffusion coefficient of 3.11 μm^2/s has been estimated a minute after adding both species. This diffusion coefficient value decreases gradually to reach 1.17 μm^2/s after 64 minutes. Based on the Stokes-Einstein equation, the hydrodynamic radius of individual particles increases by a factor of

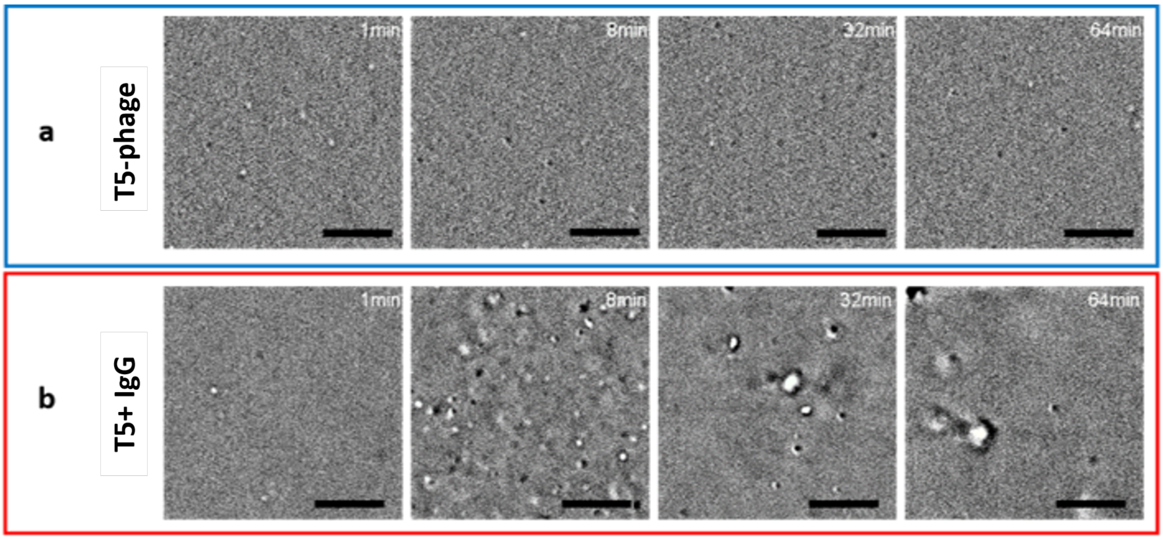

Figure 3.6: **Visual inspection of processed images** . **a** represents images of T5-phages only and **b** shows images of T5+IgG molecules (scale bar=5µm)

3 in 64 minutes (fig3.7 (a)). The modification of the diffusivity of particles is paralleled the continuous rise of the interferometric signal as shown in fig3.7 b.

We would like to add that we did not detect any significant modification in terms of diffusion coefficient, interferometric intensity, and the number of tracked particles for the T5 control test, as shown in fig3.7.

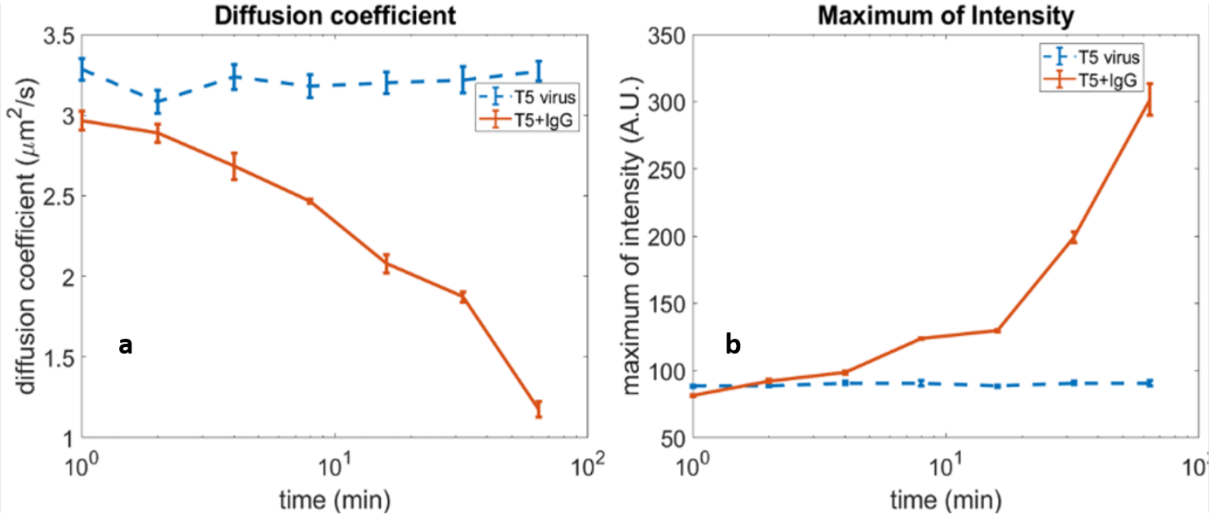

Figure 3.7: **Modification of the diffusion coefficient and the interferometric signal describing the reaction between T5+IgG** . **a** and **b** show the variation of the diffusion coefficient and the interferometric intensity, respectively, for T5+IgG and the T5 control.

The interaction between phages and Ab can be confirmed by the progressive increase of the interferometric intensity. Then, the Brownian motion of the particles gets slower since the hydrodynamic radius of the particles increases progressively to reach micrometric size aggregates.

3.2.3 Monitoring the serum-viruses reaction

So far, we have demonstrated the use of our approach to monitor the interaction between viruses and purified antibodies. In this part of the manuscript, we expand the applicability of this approach by studying the interaction between the targeted phage (SPP1) and non-purified serum-containing multiple polyclonal antibodies molecules. For this purpose, we used SPP1 bacteriophages and non-purified serum against the virus.

SPP1 bacteriophage have a similar T5 morphology, icosahedral capsid (60 nm diameter) and a long, flexible tail (190 nm) [17], initial concentration: 2.24*10^{11}PFU/mL. SPP1 dilution buffer solution consists of (100mM Tris-Cl pH=7.5, 100mM NaCl, 10mM $MgCl_2$. **The anti-SPP1 serum** mainly recognizes two proteins of the protein of the viral particle, most likely because they are the most exposed at the particle's surface in several ten of copies. However, these are not the most abundant proteins in the particle. Furthermore, the serum also recognizes some other proteins much less efficiently, neither on the tail or the capsid of SPP1 [18, 19]. Therefore, quantifying the interactions of the antibodies of this serum with specific proteins of SPP1 can be difficult.

Serum can be more challenging since it can consist of different particles that do not necessarily interfere with the interaction between antibodies and the virus. These particles affect the single-particle tracking analysis. Nevertheless, serums are usually more stable than purified antibodies, which can lose their effectiveness in several weeks. Furthermore, serum can represent actual physiological conditions for usual biological samples. Therefore, We centrifuged the serum solution and aspired the supernatant after a 10 minutes centrifugation at 14000rpm to eliminate these unwanted particles. In order to perform the measurement,we add the virus solution to the diluted serum solution to have a final SPP1 concentration of 10^9PFU/mL, (PFU: Plaque forming units).

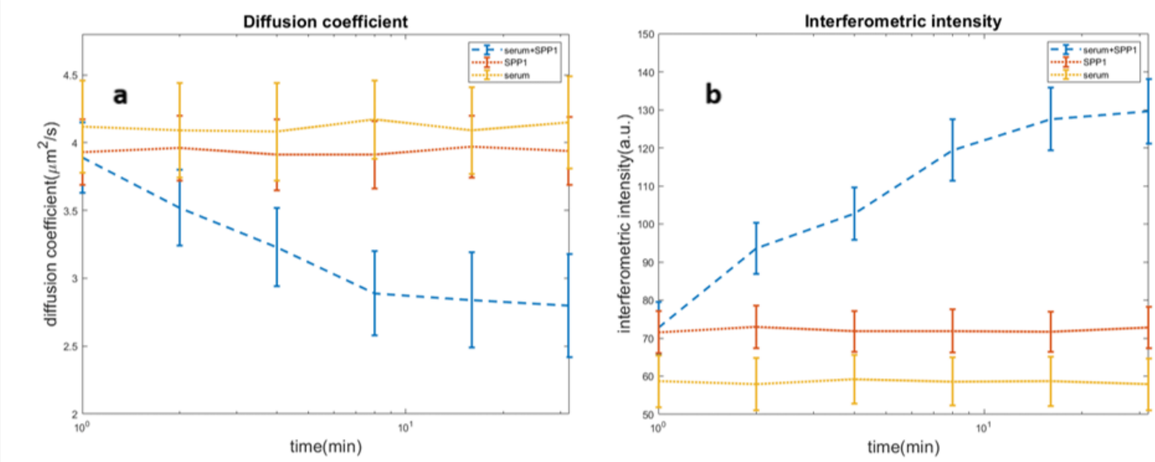

Figure 3.8: **Variation of the diffusion coefficient and the interferometric signal describing the reaction between SPP1+serum** . **a** and **b** show the variation of the diffusion coefficient and the interferometric intensity, respectively, for SPP1+serum, serum control and the SPP1 control.

Similarly to the interaction between viruses and antibodies, the progressive decrease of the diffusion mobility of individual particles has been detected for the sample containing SPP1 phages and the anti-SPP1 serum. The diffusion coefficient reduces from 3.89 to 2.73 $\mu m^2/s$ in 25minutes, as shown in fig 3.8a. This increase of the average size of the particles is confirmed by the rise of the interferometric signal, as we observed in fig 3.8b a gradual rise of the signal from 72.8 to 129.6 (A.U.) in 32 minutes. In fig 3.8, the diffusion coefficient and the interferometric signal respectively, do not vary in time for the control sample of the SPP1 and the serum sample only.

So far, in this chapter, we have been able to follow the interaction between viruses and specific antibodies as well as the interaction between viruses and non-purified serum based on the modification of the Diffusion coefficient and the interferometric contrast of single particles in the solution sample. This modification is attributed to an increase in the size of particles when interacting with antibodies in the sample. Such an approach can therefore be interesting to detect the presence of specific viruses or even specific proteins on the surface of viruses. Furthermore, it also can be convenient to detect the presence of specific antibodies in non-purified serum.

3.2.4 Quantitative analysis of the IgG-T5 reaction

Antibodies bind antigens through weak chemical interactions, and binding is essentially non-covalent. Different types of interaction can describe the recognition; electrostatic interactions, hydrogen bonds, van der Waals forces, and hydrophobic interactions are all known to be involved depending on the interaction sites [20]. The reaction gets more complicated when describing the phenomenon of cross-reactivity and other indirect bonds.

Dissociation rate and rate equation

Here, we use a quantitative approach to estimate the number of viruses that interact with the antibodies. The interaction between antibodies and specific antigens is straightforward on the molecular scale, as seen in equ 3.1. Thus a dissociation constant equ 3.2 and a rate equation can be estimated using equ 3.3.

$$\mathrm{A}b + \mathrm{Ag} \rightleftharpoons \mathrm{A}b\mathrm{A}g \tag{3.1}$$

$$\mathrm{K}_d = \frac{1}{\mathrm{K}_a} = \frac{[\mathrm{A}b][\mathrm{Ag}]}{[\mathrm{A}b\mathrm{Ag}]} \tag{3.2}$$

$$\mathrm{R}ate\mathrm{E}quation = -\frac{\Delta[\mathrm{A}b]}{\Delta t} = -\frac{\Delta[\mathrm{Ag}]}{\Delta t} = \frac{\Delta[\mathrm{A}b\mathrm{Ag}]}{\Delta t} \tag{3.3}$$

Where $\mathrm{A}b$, $\mathrm{A}g$, and $\mathrm{A}b\mathrm{A}g$ represent antibodies molecules, antigen molecules, and the recombination of both molecules. K_a,K_d are the association and dissociation constants, respectively.

The reaction between antibodies and antigens depends on the characteristics of the two species. The avidity and affinity of antibodies rely on the dissociation constant for the interaction they describe. In a few words, the main difference between affinity and avidity is that affinity is the strength of a single interaction of an antibody, whereas avidity is the strength of accumulation of multiple affinities. The lower the dissociation constant, the higher the avidity or affinity, and the stronger the interaction.

However, we are interested in the reaction at the virus particles scale. Therefore, instead of studying the interaction between antibodies and antigens, we study the reaction on a macromolecular level. This part of this section is inspired by Enzyme Kinetics: Principles and Methods [21] . To describe the reaction, we are interested in studying the concentrations of macromolecule virus [V], the free substrate antibodies [Ab], and the antibody-virus complex [V Ab]. Here, only the total initial amounts of virus $[\mathrm{V}]_0$ and ligand $[\mathrm{A}b]_0$ added to the reaction are known. Therefore, according to the mass conservation principle, all the viruses present in the solution can be separated into free and bound components expressed as:

$$[\mathrm{V}]_0 = [\mathrm{V}] + [\mathrm{VA}b] \tag{3.4}$$

$$[\mathrm{A}b]_0 = [\mathrm{A}b] + [\mathrm{VA}b] \tag{3.5}$$

Using equ 3.4and equ 3.5 the dissociation rate describing the formation of macromolecule+ligand can be expressed as:

$$\mathrm{K}_d = \frac{([\mathrm{V}]_0 - [\mathrm{VA}b])\,[\mathrm{A}b]}{[\mathrm{VA}b]} \tag{3.6}$$

Therefore, equ 3.7 Describes the binding of a ligand to a macromolecule with one binding site.

$$[\mathrm{VA}b] = \frac{[\mathrm{V}]_0\,[\mathrm{A}b]}{\mathrm{K}_d + [\mathrm{A}b]} \tag{3.7}$$

However, the IgG (anti pb8) molecules used for this experiment target the capsid proteins that represents about 800 binding sites per capsid. In our analysis, we consider that all the binding sites have an independent and equal probability of interaction with the antibodies in the solution sample. Hence, the bound antibodies can no longer be equated with [V Ab] but comprise the sum of all forms of V Ab bounds. Here, the dissociation rate of the reaction is described as:

$$\begin{array}{ll}
\mathrm{A}b + \mathrm{V} \rightleftharpoons \mathrm{A}b\mathrm{V} & \mathrm{K}'_{d1} = \frac{[\mathrm{A}b][\mathrm{V}]}{[\mathrm{A}b\mathrm{V}]} \\
\mathrm{A}b + \mathrm{A}b\mathrm{V} \rightleftharpoons \mathrm{A}b_2\mathrm{V} & \mathrm{K}'_{d2} = \frac{[\mathrm{A}b\mathrm{V}][\mathrm{A}g]}{[\mathrm{A}b_2\mathrm{V}]} \\
\ldots & \ldots \\
\mathrm{A}b + \mathrm{A}b_{n-1}\mathrm{V} \rightleftharpoons \mathrm{A}b_n\mathrm{V} & \mathrm{K}'_{dn} = \frac{[\mathrm{A}b_{n-1}\mathrm{V}][\mathrm{A}g]}{[\mathrm{A}b_n\mathrm{V}]}
\end{array}$$

Hence, the concentration of bound antibodies in the solution sample depends on the consecutive step recognition between Ab and the macromolecule consisting of the possible binding target. Yet, measuring the concentration of all species in the solution is complicated. Therefore, another implicit way to find the number of bound antibodies is by finding the number of remaining macromolecules of virus particles that are not affected by the reaction when reaching the system equilibrium.

The interaction between the n binding sites present on the virus and antibodies in the solution sample can be described by a saturation function r described by the ratio of the concentration of bound antibodies presented in equ 3.7 and the initial concentration of virus:

$$r = \frac{[\mathrm{A}b]_{\mathrm{bound}}}{[\mathrm{V}]_0} = \frac{n[\mathrm{A}b]}{\mathrm{K}_d + [\mathrm{A}b]} \tag{3.8}$$

The saturation ratio function can be calculated based on the hypothesis that all the binding sites presented on the capsid surface are bound to specific antibodies in the solution. The complex reaction is described in details in [21]. Here, we would like to note that the bound antibodies are estimated using the n binding sites on one capsid.

On a higher scale, the interaction between viruses and antibodies can be represented as:

$$x\mathrm{A}b + y\mathrm{V} \rightleftharpoons z\mathrm{VA}b + \cdots \text{ aggregation} \tag{3.9}$$

$$\text{Rate Equation } = -\frac{1}{x}\frac{\Delta[\mathrm{A}b]}{\Delta t} = -\frac{1}{y}\frac{\Delta[\mathrm{V}]}{\Delta t} \tag{3.10}$$

Where x, y, z are the stoichiometric coefficients of the reaction for each species: antibodies, viruses and aggregates virus- antibodies respectively. Monitoring the rate equation is particularly interesting to monitor the variation the speed of the reaction for a specific concentration of antibodies.

Estimation of the affinity of antibodies using single particle tracking analysis

We performed several measurements in which the same amount of viruses was used with different concentrations of antibodies. We changed the concentration by a factor of 5000 between the most and least dilute samples to have different data point for different concentration for the estimation of the dissociation constant on the virus particle scale. As mentioned previously in this chapter, the optical setup cannot detect single antibodies. The aggregation between viruses and antibodies is not homogeneous (particles of different size can be tracked for different time interval) and therefore we estimated various diffusion coefficients using single-particle tracking analysis corresponding to different sizes of particles. Hence, in the following analysis, we rely on the number of tracked viruses only (that did not interact with antibodies presented in the solution), particles having a similar diffusivity as the T5 control sample.

Fig 3.9 a shows the diffusion coefficient histogram curve of the T5 control samples for different time intervals. When plotting the estimated diffusion coefficient histogram curve, we could see an overlap of the estimated diffusion coefficient curves for different time intervals. This plot shows that the number of tracked particles (presented by the amplitude of the curves) as well as the estimated diffusion coefficient is stable for the T5-phages control. Therefore, we retrieve the mean diffusion coefficient curve of the T5 control in order to compare it to the measurements done when adding antibodies at different time intervals as presnted in yellow in fig 3.9 b and c.

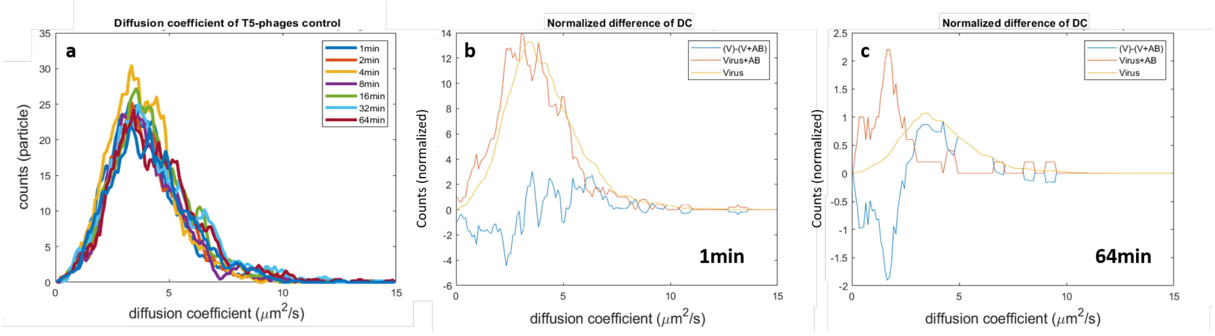

Figure 3.9: **Diffusion coefficient of the T5-phage control sample and variation of the diffusivity when adding specific IgG molecules.** **a** shows the diffusion coefficient histogram curves of the control T5 samples at different time intervals. **b** and **c** show comparison between the estimated diffusion coefficient of the average T5 control samples and T5+IgG molecules after 1 minute after adding the virus and 64minutes later, respectively.

We compared the diffusion coefficient histogram curve for each concentration and different time intervals to the T5 control sample only. When adding antibodies to the virus solutions, the number of tracked particles varies for the different time intervals. Here, we normalize the diffusion coefficient histogram for each case in number of tracked particles to be able to compare it to the average T5-control diffusion coefficient. Here, we estimate a percentage of virus particles by comparing the diffusion coefficient histogram curve to the T5 control for each measurement. In practice, we subtract both normalized curves representing the diffusion coefficient V-(V+Ab), and then we calculate the integral of the positive area. Then, we compare the ration of the positive area to the integral of the normalized curve for a given time interval to find the percentage of virus particles in the solution. We then estimate the number of tracked virus particles using these ratios values of the total tracked particles in each measurement. One can notice from fig 3.9c that the diffusion coefficient peak shifts towards a smaller diffusion coefficient after 64 minutes compared to the diffusion coefficient curve 1 minute after adding the antibodies, as shown in fig 3.9b (here, we show the curves for a 20x dilution of the initial IgG solution).

We thus estimated the number of virus particles not interacting with IgG for different concentrations of IgG molecules as a function of time intervals as shown in fig 3.10. As we can see the number of tracked unbound virus particles decreases as a function of time. Here, two behaviors can be seen, specifically for the high concentration of antibodies. For small time intervals, the number of detected viruses decreases rapidly in a few minutes. Then, it reaches an asymptotic behavior indicating that the system has reached its chemical equilibrium.

Hence, we estimated the number of bound viruses by subtracting the number of virus particles from the initial number of viruses in the control sample ($V_{bound} = V_0 - V(t)$). Then, we

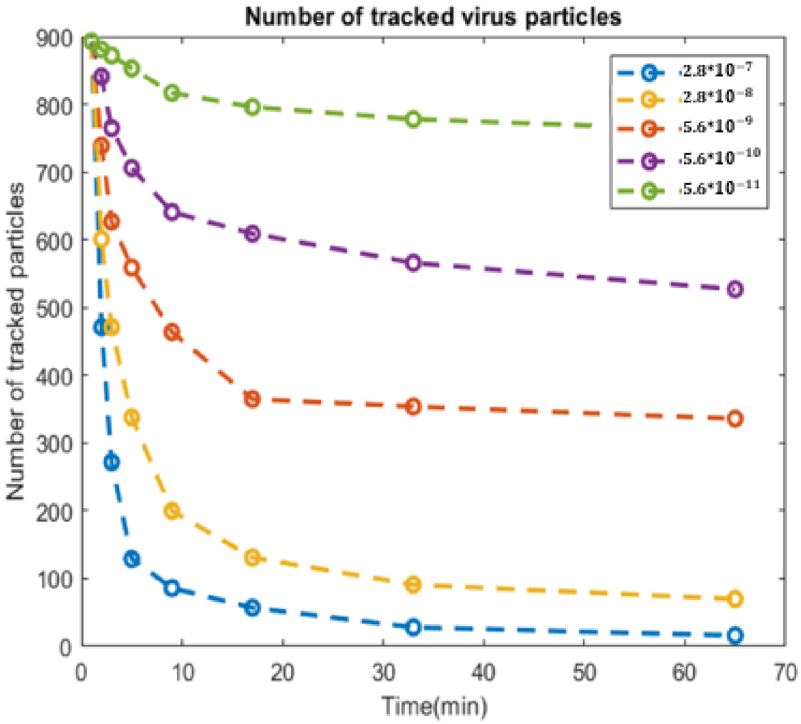

Figure 3.10: **Plot showing the number of tracked T5-phages for different concentrations of antibodies at different time intervals**

can estimate the number of bound antibodies as $\mathrm{A}b_{bound} = n * \mathrm{V}_{bound}$.

We then calculate the molar concentration of the IgG molecules in the samples using the number of unbound viruses, knowing that the molar mass is about 108.4 MDa and for the IgG molecules is about 150KDa. Therefore, we plot the saturation function as presented in equ 3.8. Fig3.11 shows, on the left axis, the saturation function of the binding as function of the concentration of Ab in a semi-log representation. Thus, based on equation 3.8, we can find the K_d for a specific value of $r = n/2$, knowing that the n=800 binding sites. By fitting the experimental data using saturation function formula, we estimated $\mathrm{K}_d = 1.12 * 10^{-9}$M.

Furthermore, equation 3.10 describes the reaction between phages and antibodies on a higher scale, so we are interested in measuring the speed of the reaction depending on the concentration of Ab in the solution. We attribute a half-life before reaching the system's equilibrium state when varying the initial concentration of Ab. Despite the equilibrium state being reached at a different time interval, we attribute the number of virus particles at 64 minutes to the equilibrium. Then, we estimate the variation of the number of virus particles of the time interval corresponding to the half-life time $(([\mathrm{V}]_0 - [\mathrm{V}]_{64})/2)$. The right axis in Fig3.11 shows the disappearance rate of virus particles in the solution. In order to know the equation rate of the reaction, the proportional coefficient based on the stoichiometric coefficient is needed. Although we plotted the disappearance rate of viruses in the solution as a function of the concentration of antibodies, despite that this disappearance rate of viruses is proportional to the rate equation, we still need to find the stochiometric ratio of the reaction to be able to retrieve the rate equation of the reaction.

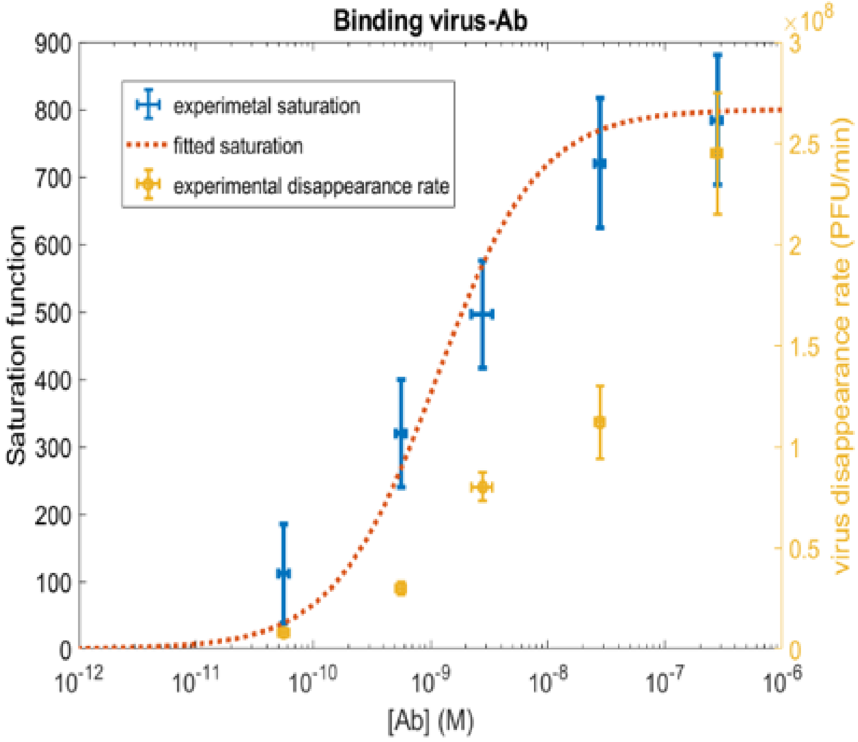

Figure 3.11: **Plot representing the saturation ratio function and the variation of the number of viruses as a function of IgG concentration**

Using this approach, we were able to estimate the dissociation rate of the IgG by relying on the modification of the diffusivity properties of the viruses in the sample solution. Furthermore, since we rely on the number of virus particles in our analysis, we are not affected by the modification of the depth of field affected by the properties of the particles as mentioned in chapter2.

3.3 Discussion and general conclusion

Through these examples, we have combined the interferometric signal contrast with the single particle tracking analysis to analyze the particles diffusion mobility and composition.

3.3.1 Increase the sensitivity and sensibility of the optical set-up

This approach has been used to distinguish between 2 populations of capsids of a similar size. Furthermore, viruses have been added to specific antibodies, and we have been able to monitor the antibody-virus reaction evolution in a wide field of view ($103\mu m$ x $103\mu m$). The recognition signature was detected in a few minutes. We also demonstrate the possible application of this approach in monitoring the evolution of the reaction between phages and non-purified serum, representing a more realistic way to study physiological samples of viruses and estimate the affinity value of specific antibodies.

Further technical improvement can be made to have a better sensitivity and sensibility. An efficient approach is based on attenuating the reference light beam in the pupil plane of the objective. This approach can be very practical in the case of having sufficient light power to saturate the camera to a shot-noise limited level and increase the interferometric contrast in. Moreover, we estimate a detection limit for particles of 50 nm in diameter SPP1 viruses with a lower concentration of 10^8particles/mL for the acquisition of 500 frames at 500 FPS. In order to detect a small concentration of particles, a trivial solution can be found by acquiring images for longer times. Although the volume of detection is linked to the numerical aperture of the objective lens, one efficient strategy to increase the volume of detection without affecting the intensity signal is to use a phase mask in the pupil plane of the objective lens [22].

We have shown in this study that a simple, robust incoherent illuminated common path interferometer can be used to characterize nanoparticles in biological samples. The simplicity and yet the robustness of the detection method and the use of antibodies for specificity and processing might define new perspectives for virus and antibodies detection as a medical diagnosis tool (to quantify viruses or antibodies in solutions) and a control tool for the pharmaceutical drug delivery methods using viruses and vesicles and differentiate between their genetic loads.

3.3.2 Conclusion

In the single-particle analysis presented before, we estimate a diffusion coefficient resulting from a certain hydrodynamic radius. We have studied different types of viruses having different shapes, mainly interested in bacteriophages, T5, and SPP1 bacteriophages. These bacteriophages consist of a symmetrical icosahedral head and a long tail. Despite that the diameter of the tail is very small compared to the size of the head, we estimated a diffusion coefficient smaller than the theoretical diffusion coefficient corresponding to the size of the head only, as shown previously in the chapter. This observation is confirmed by more than a 20% reduction of the diffusion coefficient when comparing the T5 phage to full and empty capsids of T5 lacking the infective tail. These observation are interesting for a better understanding of the infective behavior of these bacteriophages.

Bibliography

[1] Aryn A Price, Timothy R Sampson, Hannah K Ratner, Arash Grakoui, and David S Weiss. Cas9-mediated targeting of viral rna in eukaryotic cells. *Proceedings of the National Academy of Sciences*, 112(19):6164–6169, 2015. 48

[2] Sue C Kehl and Swati Kumar. Utilization of nucleic acid amplification assays for the detection of respiratory viruses. *Clinics in laboratory medicine*, 29(4):661–671, 2009. 48

[3] Robert C Benirschke, Erin McElvania, Richard B Thomson Jr, Karen L Kaul, and Sanchita Das. Clinical impact of rapid point-of-care pcr influenza testing in an urgent care setting: a single-center study. *Journal of clinical microbiology*, 57(3):e01281–18, 2019. 49

[4] Ian W Pray. Performance of an antigen-based test for asymptomatic and symptomatic sars-cov-2 testing at two university campuses—wisconsin, september–october 2020. *MMWR. Morbidity and mortality weekly report*, 69, 2021. 49

[5] Ian W Pray. Performance of an antigen-based test for asymptomatic and symptomatic sars-cov-2 testing at two university campuses—wisconsin, september–october 2020. *MMWR. Morbidity and mortality weekly report*, 69, 2021. 49

[6] Irena Zurnic Bönisch, Lieve Dirix, Veerle Lemmens, Doortje Borrenberghs, Flore De Wit, Frank Vernaillen, Susana Rocha, Frauke Christ, Jelle Hendrix, Johan Hofkens, et al. Capsid-labelled hiv to investigate the role of capsid during nuclear import and integration. *Journal of virology*, 94(7):e01024–19, 2020. 49

[7] Boerries Brandenburg and Xiaowei Zhuang. Virus trafficking–learning from single-virus tracking. *Nature Reviews Microbiology*, 5(3):197–208, 2007. 49

[8] Nicole C Robb, Jonathan M Taylor, Amy Kent, Oliver J Pambos, Barak Gilboa, Maria Evangelidou, Alexios-Fotios A Mentis, and Achillefs N Kapanidis. Rapid functionalisation and detection of viruses via a novel ca2+-mediated virus-dna interaction. *Scientific reports*, 9(1):1–13, 2019. 49

[9] Richard W Taylor and Vahid Sandoghdar. Interferometric scattering microscopy: seeing single nanoparticles and molecules via rayleigh scattering. *Nano letters*, 19(8):4827–4835, 2019. 49

[10] Gavin Young and Philipp Kukura. Interferometric scattering microscopy. *Annual review of physical chemistry*, 70:301–322, 2019. 49

[11] Anna Olerinyova, Adar Sonn-Segev, Joseph Gault, Cédric Eichmann, Johannes Schimpf, Adrian H Kopf, Lucas SP Rudden, Dzmitry Ashkinadze, Radoslaw Bomba, Lukas Frey, et al. Mass photometry of membrane proteins. *Chem*, 7(1):224–236, 2021. 49

[12] Marek Piliarik and Vahid Sandoghdar. Direct optical sensing of single unlabelled proteins and super-resolution imaging of their binding sites. *Nature communications*, 5(1):1–8, 2014. 50

[13] Victor Yin, Szu-Hsueh Lai, Tom G Caniels, Philip JM Brouwer, Mitch Brinkkemper, Yoann Aldon, Hejun Liu, Meng Yuan, Ian A Wilson, Rogier W Sanders, et al. Probing affinity, avidity, anticooperativity, and competition in antibody and receptor binding to the sars-cov-2 spike by single particle mass analyses. *ACS central science*, 7(11):1863–1873, 2021. 50

[14] Roi Asor and Philipp Kukura. Characterising biomolecular interactions and dynamics with mass photometry. *Current Opinion in Chemical Biology*, 68:102132, 2022. 50

[15] Alexis Huet, Robert L Duda, Pascale Boulanger, and James F Conway. Capsid expansion of bacteriophage t5 revealed by high resolution cryoelectron microscopy. *Proceedings of the National Academy of Sciences*, 116(42):21037–21046, 2019. 51, 52

[16] `https://www.i2bc.paris-saclay.fr/equipe-bacteriophage-t5/`. 54

[17] Sophie Lhuillier, Matthieu Gallopin, Bernard Gilquin, Sandrine Brasilès, Nathalie Lancelot, Guillaume Letellier, Mathilde Gilles, Guillaume Dethan, Elena V Orlova, Joël Couprie, et al. Structure of bacteriophage spp1 head-to-tail connection reveals mechanism for viral dna gating. *Proceedings of the National Academy of Sciences*, 106(21):8507–8512, 2009. 56

[18] Isabelle Auzat, Anja Dröge, Frank Weise, Rudi Lurz, and Paulo Tavares. Origin and function of the two major tail proteins of bacteriophage spp1. *Molecular microbiology*, 70(3):557–569, 2008. 56

[19] Athanasios Ignatiou, Sandrine Brasilès, Mehdi El Sadek Fadel, Jörg Bürger, Thorsten Mielke, Maya Topf, Paulo Tavares, and Elena V Orlova. Structural transitions during the scaffolding-driven assembly of a viral capsid. *Nature communications*, 10(1):1–11, 2019. 56

[20] CJ Van Oss, RJ Good, and MK Chaudhury. Nature of the antigen-antibody interaction: Primary and secondary bonds: optimal conditions for association and dissociation. *Journal of Chromatography B: Biomedical Sciences and Applications*, 376:111–119, 1986. 57

[21] Hans Bisswanger. *Enzyme kinetics: principles and methods*. John Wiley & Sons, 2017. 58, 59

[22] Olivier Lévêque, Caroline Kulcsár, Antony Lee, Hervé Sauer, Artur Aleksanyan, Pierre Bon, Laurent Cognet, and François Goudail. Co-designed annular binary phase masks for depth-of-field extension in single-molecule localization microscopy. *Optics Express*, 28(22):32426–32446, 2020. 63

Chapter 4

Surprising in-depth PSF, interpretation and optimization of the interferometric contrast

Contents

4.1 Understanding the interferometric signal intensity

The radiation patterns and intensity profiles of dielectric, non-absorbing nanoparticles depend on the size of the nanoparticle and the refractive index difference between the particle and the surrounding medium, as presented in the first chapter. In a few words, under plane wave illumination, the scattered field is characterized by larger intensity in the forward direction for particles of diameters larger than $\lambda/2\pi$ whereas smaller particles (typically less than 50nm in diameter) exhibit a more isotropic scattering (Rayleigh scattering), as shown in fig4.1 a. Furthermore, the elongation of the scattered electric field due to the size of the particle of interest can be understood when considering near field Finite-Difference Time-Domain (FDTD) simulations presented in fig4.1 b, c and d. In these simulations, indeed the near-field cigar-shaped field distribution is much more pronounced for larger particles that makes the scattered field more intense in the forward direction because off axis phases are more likely to be out of phase.

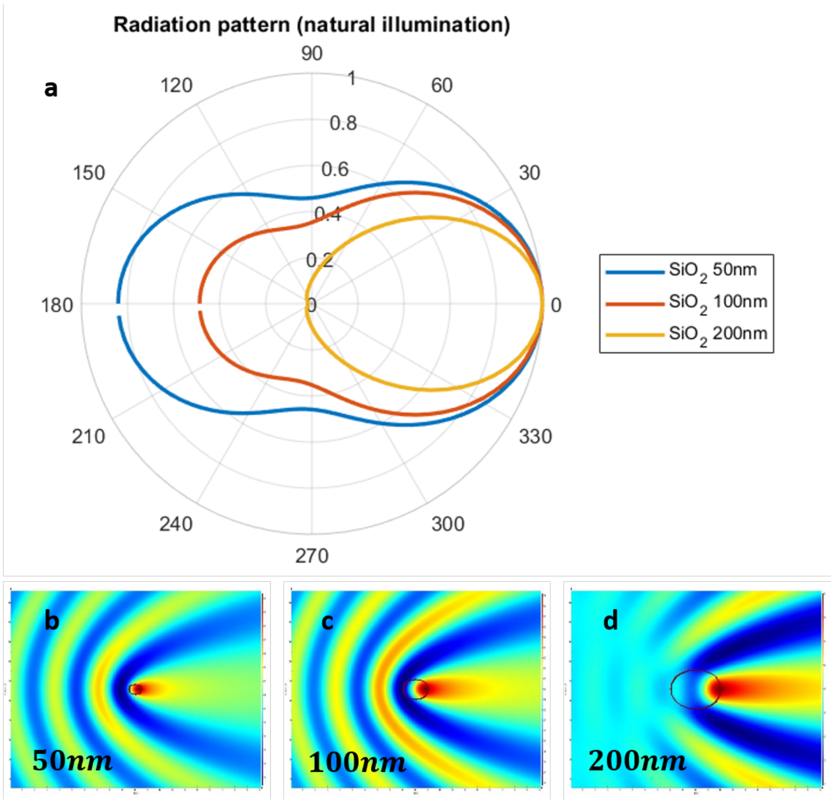

Figure 4.1: **Radiation diagram and 2D profile of the scattered field for** SiO_2 **particles , of 50, 100 and 200nm in diameter, immersed in water.a** shows the normalized radiation pattern, using mie calculator[1]. **b,c and d** represent the 2D profile of the three different size of particles when illuminated with a plane wave (from left to right), FDTD simulations performed on Lumerical, FDTD-solutions

In the Rayleigh regime, the scattered field amplitude scales with the third power of the size of particles. Therefore, the bigger the particle gets, the forward propagating scattered field is more pronounced. However, in practice, we did not observe such expected behavior of the measured scattered field. In this chapter, we are interested in understanding the interferometric signal to increase the interferometric contrast to detect smaller particles.

4.1.1 Interferometric Intensity signal for SiO_2 nanoparticles

Interferometric intensity for different sizes of particles

Using a water immersion objective lens (Na=1, 100x Olympus) dipped directly into the sample solution containing nanoparticles, we have measured a progressive increase of the interferometric intensity as a function of the size of the particles for SiO_2 nanoparticles of 50, 100, and 200 nm in diameter, this intensity is shown in the fig 4.2. Here, the half scattering angle is expected to be about 75, 60, and 45 degrees for 50, 100, and 200 nm particles, respectively. The acceptance angle is about 49 degrees for a NA=1 in water. In a second test, we have replaced the water immersion objective lens with an oil immersion objective lens (NA=1.25, 100x, Olympus). Here, the sample solution containing nanoparticles is sandwiched between 2 coverslips, and the nanoparticles can move freely in the solution. Although the acceptance angle is about 70 degrees in water, the measured intensities are similar to those measured with the water immersion objective lens, as seen in the fig 4.2. Let us note that the acceptance angle difference is amplified considerably when considering the solid angle $\omega = (2\pi(1-\cos\theta))$ in the 3D space and θ represents the acceptance angle of the objective lens, 2.16 and 4.13 steradians for water and oil immersion objective lenses respectively. We add that despite that we compare the absolute maximum of intensity of the moving particles using different objective lenses.

One can be surprised by the quasi-linear dependence of the signal amplitude to the particle diameter d (instead of the d^3, expected for the Rayleigh scattering regime). This is due to the extension of the electric field in the axial direction, as can be seen in fig4.1. This extension overlaps the positive and negative signal region and reduces significantly for particles larger than 50nm in diameter.

The use of an oil immersion objective lens can be practical in different ways. As presented before, the evident advantage is collecting more light scattered in larger angles. Even more, oil immersion objective lenses usually have working distances smaller than those of water immersion objective lenses, and therefore a smaller sample volume is required. In addition, usually, oil immersion objectives are much cheaper. However, when going into depth in the sample volume, the refractive index mismatch between the immersion liquid ($n_{oil} = 1.51$)and the sample solution ($n_{water} = 1.33$) induces spherical aberrations that are expected to decrease the image quality.

The effect of aberrations in imaging instruments is to blur images and reduce their contrast and signal-to-noise ratio. It is common to improve optical images quality by compensating for aberrations in either a static way using eyeglasses for eyes or a Schmidt corrector plate for telescopes or dynamically by taking advantage of adaptive optics (AO) for astronomy or microscopy observations[2, 3]. For interferometric imaging working in reflection such as OCT (Optical Coherence Tomography), the coupling with AO has led to spectacular progress in retinal high-resolution imaging [4] in terms of resolution and signal level detection. Numerical based aberration corrections methods have also successfully restored the image quality

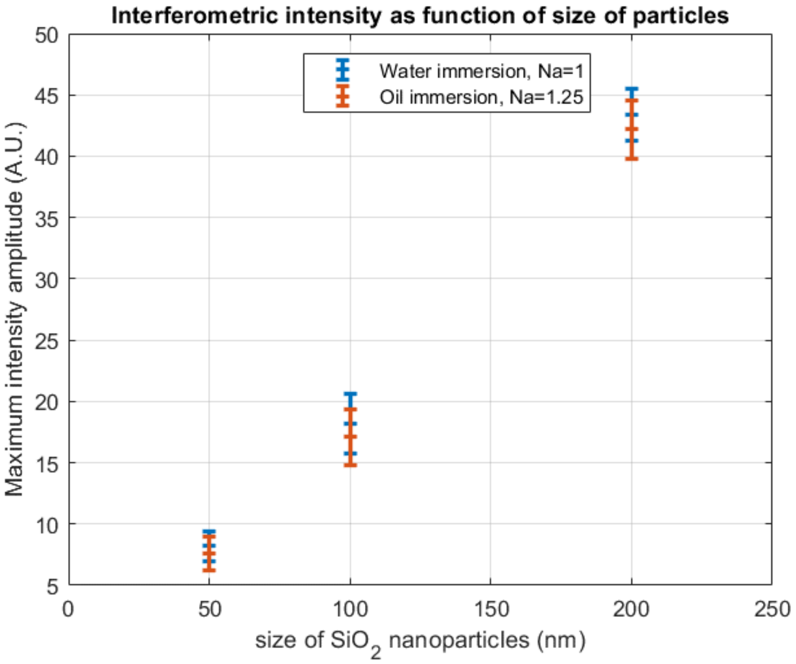

Figure 4.2: **Maximum intensity amplitude of** SiO_2 **of 50, 100 and 200 nm in diameter in water** The maximum intensity represents the amplitude of the gaussian fitting of the spots, the detected intensity does not follow Rayleigh's regime

[5]. When using incoherent illumination in a full field model (FFOCT), it has been proved experimentally and theoretically using a Strehl ratio-based approach that the point spread function (PSF) width is almost insensitive to moderate symmetric aberrations [6]. A deeper theoretical, analytical description of full-field optical coherence tomography (FF-OCT) was given in [7]; moreover, a numerical calculation coupled to experimentally induced aberrations can be found in [8]. In brief, for even small wavefront distortions (e.g., defocus or spherical aberration), the PSF (or the modulation transfer function, MTF) is not affected, but the signal strength is damped whereas for odd wavefront distortions (e.g., coma) the image is blurred. When a "best focus" that minimizes the Strehl ratio is achieved, the parity of the aberration is lost, and it can be shown that the MTF [9] keeps its properties. Strehl ratio is proportional to the peak of the aberrated image intensity $\exp\left(-\sigma^2\right)$, where σ is the root mean square deviation over the aperture of the wavefront phase $\sigma^2 = (std(\phi)^2)$ and ϕ is the phase of the interference wavefront between the sample signal and the reference signal coming from the coherence area. In the absence of aberrations and using a uniform incoherent light source located at the image plane of the objective lens, the spatial coherence areas (CA) at the level of the focal plane correspond to a zone of radius $\rho = f_0 \lambda / D$or $\rho = \lambda / 2NA$, where f_0 is the focal length of the objective lens and D is the pupil diameter. In the case of signal determination for the point of interest, the overlap between the reference and the scattered amplitude is perfect, and the Strehl ratio is 1. In our case, opposite to FFOCT for which the reference beam is not perturbed, both the reference and the scattered field are similarly affected by aberrations.

4.1.2 Effective numerical aperture of the system

Imaging particles deep in the sample solution

The first manifestation of the refractive index mismatch between the objective immersion liquid and the sample liquid can be seen in fig4.3 by the shift of the focal plane of the objective lens based on Snell law. For instance, using an oil immersion objective of NA=1.25 if the particle is about 15 μm below the coverslip, the focus plane shifts more than 5 μm for a numerical aperture of 1.25. This spherical aberration is supposed to affect the scattered fields leading to a degradation of the resolution and a decrease of the interferometric intensity.

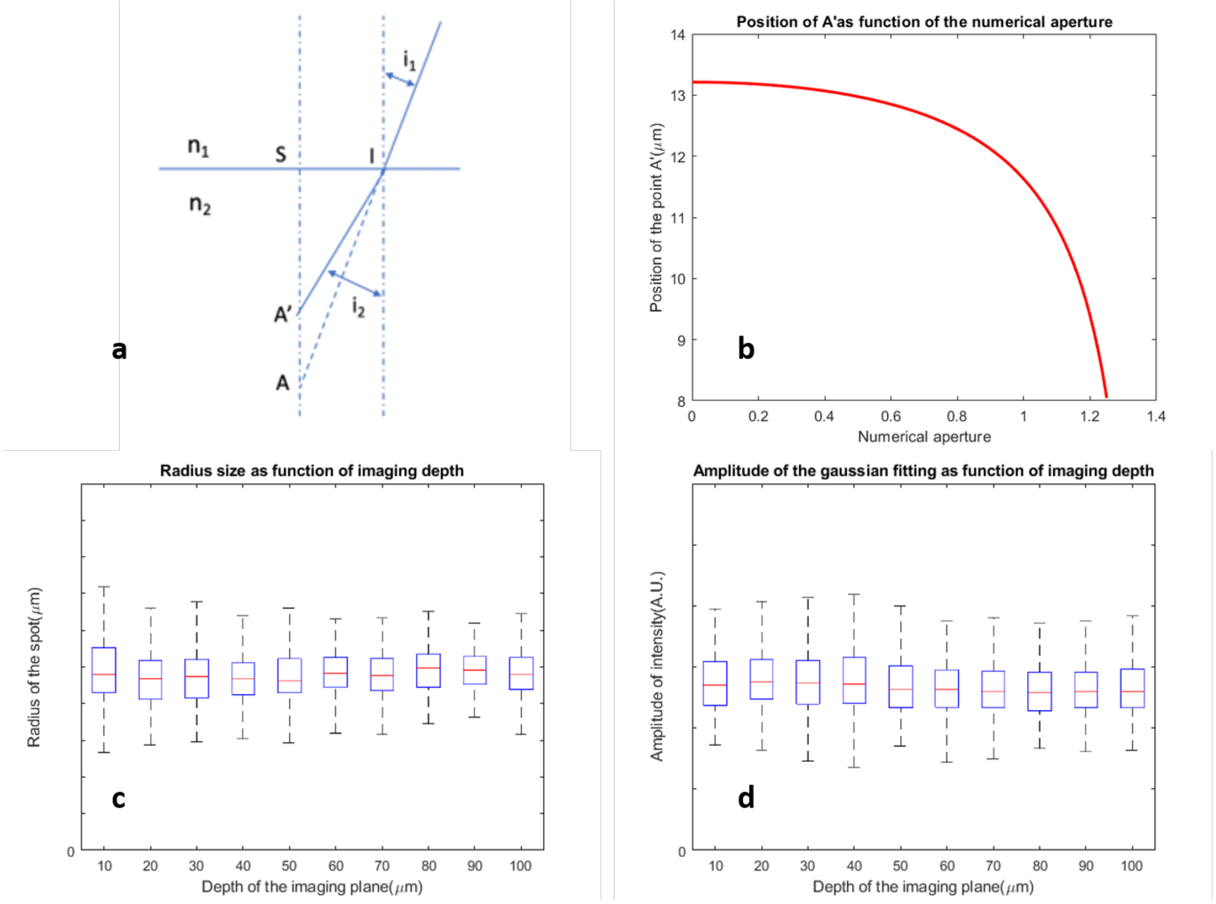

Figure 4.3: **Impact of refractive index mismatch on the intensity and PSF of** SiO_2 **of 100 nm in diameter in water** The maximum intensity represents the amplitude of the gaussian fitting of the spots. **a** shows a schematical representation of Snell's law , **b** shows the variation of the image plane position as function of the numerical aperture for an initial position of 15μm below the coverslip, and **c** represents the experimental radius of the gaussian corresponding to the ,and **d** shows the experimental variation of the absolute value of maximum of intensity signals.

Surprisingly, we found that the aberration level, associated with the depth at which we focus in water, did not affect considerably the width of the PSF nor the value of the maximum signal associated with the SiO_2 particles of 100nm in diameter experiencing Brownian motion. Even when moving the position of the objective lens 100μm below the coverslip, as shown in fig 4.3, (here, we note that we did not correct the position of the focal plane in water).

Impact of the numerical aperture on the interferometric signal

We investigated the variation of the interferometric signal as a function of the collection NA. We used an oil immersion objective lens with a variable numerical aperture (0.36-1.25, Amscope). It consists of a diaphragm at the level of the back focal plane of the objective, it allows us to therefore control the numerical aperture by adjusting the aperture size of the diaphragm.

We imaged SiO_2 nanoparticles of 50, 100, and 200 nm and gradually reduced the collection numerical aperture. When varying the numerical aperture between 1.25 and 0.54, we did not measure a significant difference in maximum intensities and the shape of the PSF when reducing the numerical aperture from 1.25 to 0.54. This behavior has been seen for all sizes of particles, as can be seen in fig4.4.

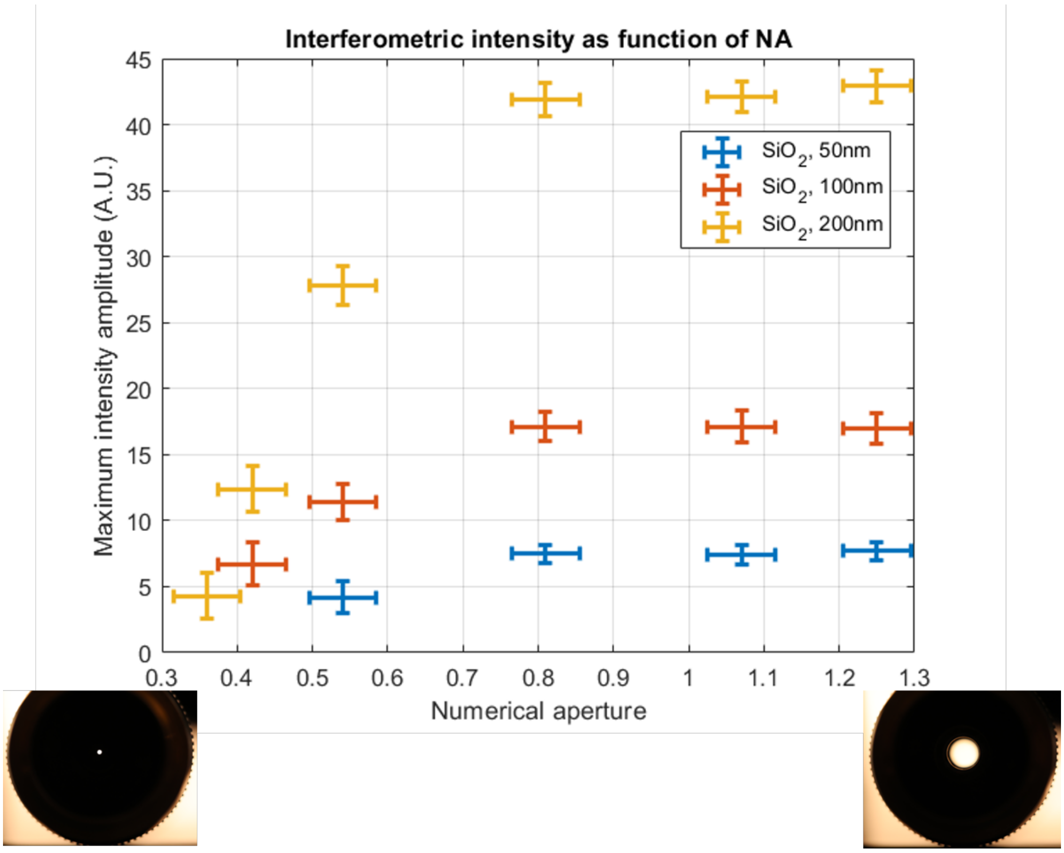

Figure 4.4: **Maximum intensity amplitude of SiO_2 of 50, 100 and 200 nm in diameter in water as function of the numerical aperture** we show the images of the back focal plane aperture for NA=0.36 and 1.25

These observations show that the effective numerical aperture of the collection is smaller than the maximum numerical aperture of the objective lens.

4.1.3 Interferometric axial PSF measurement

In order to better understand the interferometric signal behavior, we imaged nanoparticles of TiO_2 of 23nm on a coverslip to retrieve the 3D PSF. We used TiO_2 nanoparticles because of the higher refractive index than the one of SiO_2, 2.87 compared to 1.45. Here, a higher refractive index since the refractive index of the immersion oil and the coverslip is about 1.51. We would like to note that oil immersion liquid and the coverslip have similar refractive index of 1.51. Therefore, we eliminate the effect of spherical aberrations due to refractive index mismatch in this measurement. We acquire 3D images of single particles by moving a piezoelectric motor (NV 40/3 CLE, Piezosystem Jena) with a step interval of 100nm. For the z profile axis of the PSF, we realize that despite the steep variation of the interferometric intensity near to the focal plane of the objective lens, the distance between bright and dark maxima is about 2μm, much larger than the depth of field estimated for a numerical aperture of 1.25. This measurement has also been performed with a smaller numerical aperture, and a similar PSF has been estimated until a numerical aperture of 0.54 has been reached (see fig 4.5).

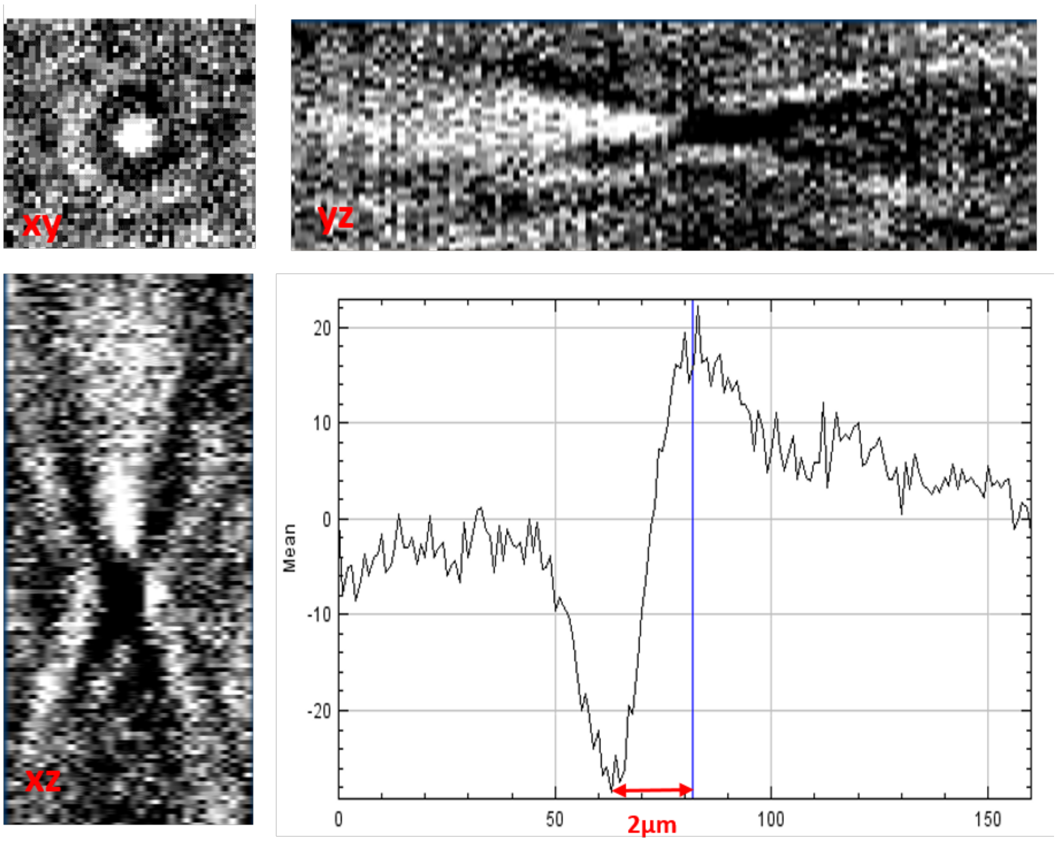

Figure 4.5: **3D interferometric PSF using TiO_2 of 23nm in diameter.** We show the xy, xz, and yz cross-sections of the interferometric PSF in addition to the z-axis profile of the interferometric intensity. The images are acquired with a step size of 100nm, and the stack size is about 16μm in the axial direction.

Using, the 3D PSF presented in fig 4.5, we compared the radiation pattern to the theoretical radiation pattern resulting from such the numerical aperture in use. Indeed, a narrower angle is estimated using experimetal PSF, whichs confirms the filling of a smaller numerical aperture compared to the numerical aperture of the objective in use. We would like to note that we have tested this objective on a fluorescence microscopy setup where we have detected a massive decrease of the fluorescent signal when reducing the NA at the back focal plane.

Interpretation of spherical aberrations induced by refractive index mismatch

These observations confirm that the effective numerical aperture is not determined by aberrations level but by the system itself, indeed similar interferometric intensities behaviours have been estimated when imaging particles in water or particles fixed on a coverslip without aberrations due to the refractive index mismatch. Here, we note that spherical aberrations are known to create a distortion affecting the wavefront by the fourth-order of the numerical aperture. However, defocus affects the interferometric signal because of the Gouy phase shift that is null at the focus plane of the objective lens, affecting the wavefront with a distortion that increases with the second-order of the numerical aperture. Since the effective numerical aperture is smaller than the one defined by the objective lens, the effect of spherical aberrations is highly dampened for a smaller numerical aperture that makes the system less sensitive to the spherical aberrations. We estimate the wavefront's standard deviation at the best focus position by varying the amplitude of the spherical aberration distortion compared to defocus aberrations ($std(a * y_1 - y_2)$), by varying the value of a to minimize the standard deviation. We found an std about 0.076 at the best focus, as shown in fig4.6 b. We then plot the wavefront distortion due to spherical aberrations as a function of the numerical aperture. Here, $n_{water} = 1.33$, $n_{oil} = 1.51$, and for a plane 88μm in water, this value corresponds to 100μm in the absence of aberrations induced by the refractive index mismatch. Also, the impact of spherical aberrations increases drastically for high numerical aperture, as shown in fig4.6b. Here, we estimated the distortion of the wavefront as a function of the numerical aperture using spherical aberration formulas presented in [10]. Thus, for a numerical aperture of 0.54, the wavefront distortion at the pupil plane is about 0.174μm.

Therefore, Strehl ratio considering the distortion at the best focus is estimated to be about $\exp(\frac{-2\pi * 0.174 * 0.076}{0.455}) = 0.84$. Thus, the impact of aberrations is not dramatically important for NA=0.54, even when imaging 100μm deep in the solution using an oil immersion objective lens.

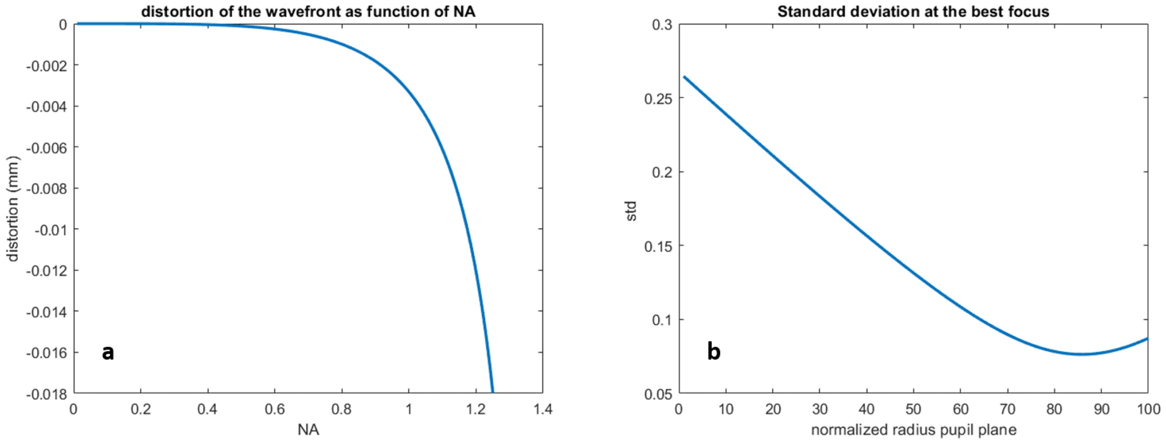

Figure 4.6: **Distortion of the wavefront at the best focus and the impact of spherical aberrations** a represents the variation of the standard deviation resulting from defocus and spherical aberrations to find the std at the best focus.b shows the spherical aberration distortion of the wavefront at the pupil plane level as a function of the NA.

4.2 Simple simulation and naïve analytical model

The previous results show that in practice, the effective numerical aperture of the system is limited to 0.5- 0.6, even when using a high numerical objective lens, NA=1.25. In this section, we first explore the local perturbation of the electric field near the focal plane of the objective lens in a simple Finite-difference time-domain (FDTD) using a Gaussian illumination to reveal the Gouy phase shift near the objective lens. In a second approach, using a simple naïve analytical model, we examine the interferometric signal of the camera plane using a Gaussian beam.

4.2.1 FDTD-Simulation near the focal plane

We used Finite-Difference Time-Domain (FDTD) method on Lumerical-solutions, FDTD module. In brief, FDTD is a fully explicit numerical solution method of the hyperbolic first-order Maxwell's curl Partial differential equation (PDE) system. The computational domain is discretized by cubic cells [11], and the spatial values of the electromagnetic field components are updated iteratively.

We want to mention that the aim of the simulation is not to develop a numerical tool to faithfully reproduce the response of nanoparticles in our optical set-up but to have a simulation allowing us to monitor the local field perturbation of the electric field due to the presence of the nanoparticle. Therefore, we are mainly interested in understanding the Gouy phase shift influence linked to the objective's position. Here, we simulate the Gouy phase using a Gaussian beam for which we can vary the numerical aperture representing the acceptance aperture imposed by the objective. We then add the particle (SiO_2, 100nm in diameter) at different positions, below and above the waist position of the focal plane as shown in fig 4.7

Here, we have seen a perturbation of the local electric field near the focus. A difference in the beam profile can be spotted when moving the particle above and below the focus. To note

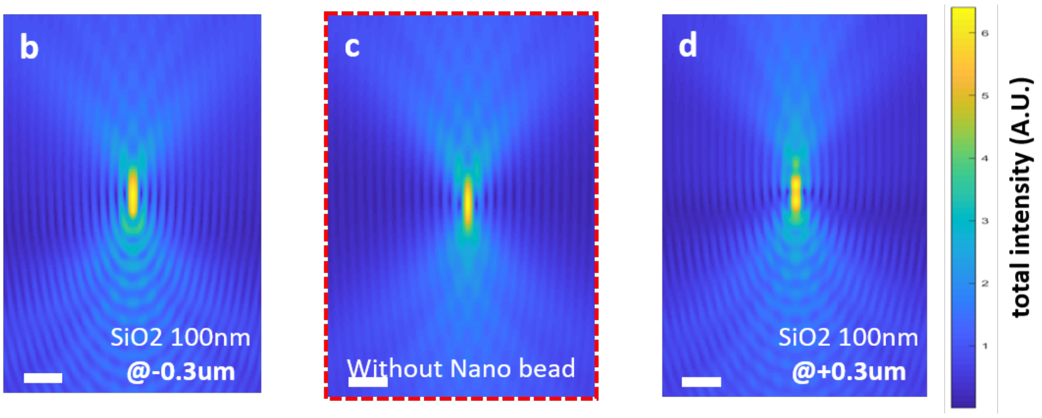

Figure 4.7: **2D profile of the local electric field of an incident Gaussian beam near its focus, NA=1.25**. **a**, **b** and **c** show the local perturbation of the electric field near the focus without particle, and with an SiO_2 nanoparticle of 100nm at 0.3µm below and at 0.3µm above the focus, respectively, scale bar=1µm.

that the signature of the presence of the particle can be seen in back-propagating fringes as seen in fig 4.7 b and c.

Although those small perturbations of the electric field can be seen in the fig above, the incident reference field is dominant. Therefore, we subtract the reference beam (without the particle) of interest from each case to better visualize the interferometric signal.

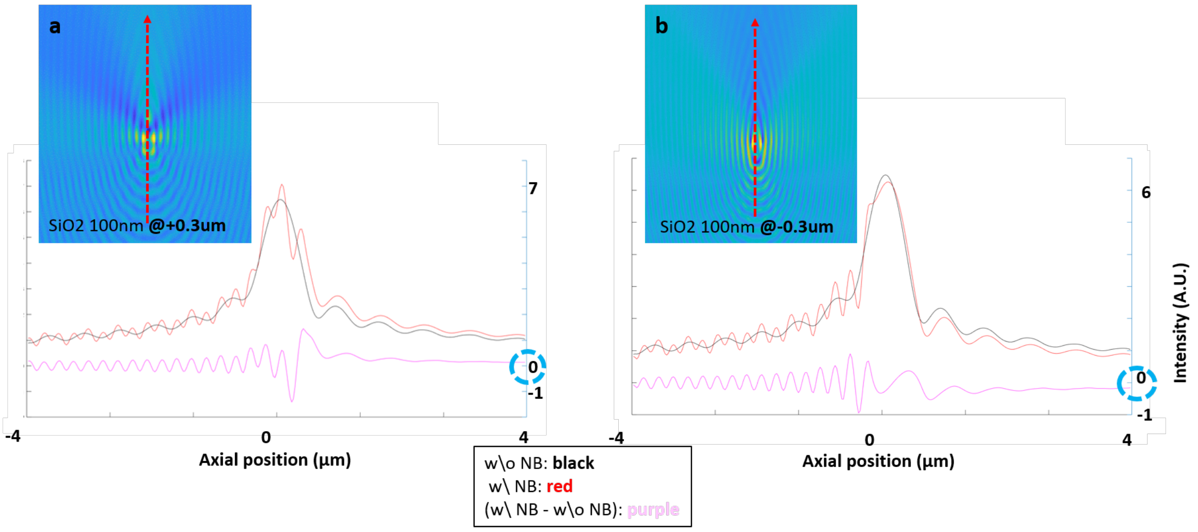

Figure 4.8: **2D profile and central profile of the electric field with a particle when subtracting the incident electric field**. **a** and **b** show the local perturbation of the electric field with an SiO_2 nanoparticle of 100nm at 0.3µm above and below the focus, respectively. For each case, the central axial plots represent the case when a particle is presented and the case without a particle and the interferometric signal

When subtracting the reference incident light from each case, similar behavior of the local electric field is seen when moving the particle around the focus, but with inversion of the field signal. This behavior can be attributed to the Gouy phase shift induced by the Gaussian beam near the focus, as seen in the fig4.8 . Therefore, we compare the forward propagating field along the central axis when moving the particle between 2 opposite positions across the focus.

Despite that the local perturbation of the electric field near the waist depends on the nanometric position of the particles, the forward propagating field is relatively stable. Therefore, we examined the influence of the particle's position on the forward propagating field for three, Numerical Aperture, 1.25, 1, and 0.6. For each numerical aperture, we moved the particle $0.5\mu m$ above and below the focus of the incident beam and monitored the value of the forward propagating field, as presented in fig4.9.

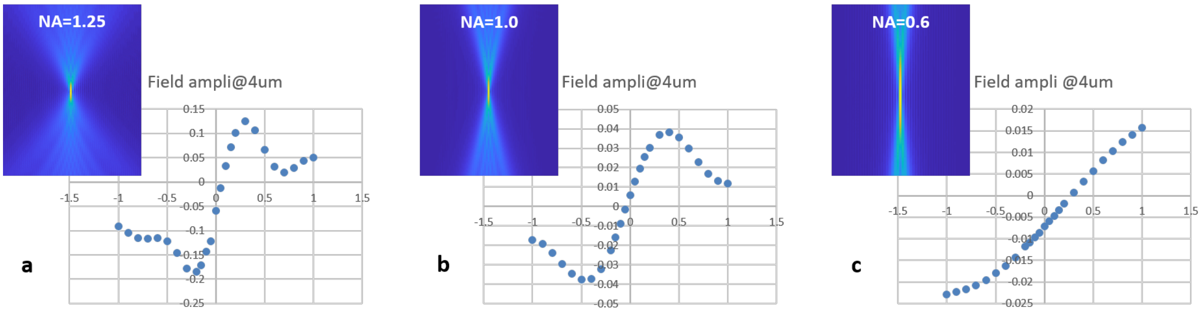

Figure 4.9: **2D profile and central profile of the electric field with a particle when subtracting the incident electric field**. **a** and **b** show the local perturbation of the electric field with an SiO_2 nanoparticle of 100nm at $0.3\mu m$ above and below the focus, respectively.

These simulations show the dependency of the numerical aperture on the forward scattering direction. Here, the impact of the Gouy phase shift can be seen by the inversion of the propagated field when crossing the focus of the Gaussian beam. In addition, we can see that the distance between the maximum and minimum at each side of the waist increases when reducing the numerical aperture of the incident Gaussian beam from 1.25 to 1 and 0.6, as shown in fig 4.9 a, b and c, respectively. However, despite the clear dependency of the numerical aperture on the interferometric signal, these profile do not correspond to the experimental data in terms of intensity as well as resolution.

4.2.2 Analytical model on the camera plane

This section of the manuscript shows the image resulting from the optical system on the camera plane. A plane wave illuminates the sub-wavelength scatterer, which scatters light in an isotropic and homogeneous way. An Airy disk presents the response of the scatterer at the camera plane. We analyze the experiment using the Gaussian beam model that provides particularly simple equations [12]. The scattered electric field can be written as:

$$E_s(r,z) = E_{s0} \exp\left(\frac{W_0}{w(z)}\right) \exp\left(-\frac{r^2}{w^2(z)}\right) \exp\left(-i\left(kz + \frac{kr^2}{2R(z)} - \psi(z)\right)\right) \tag{4.1}$$

Where E_{s0}, is the amplitude, W_0 is the waist at focus, r is the radial distance from the center axis of the beam, z is the axial distance from the beam's waist, $W(z) = W_0\sqrt{1 + (\frac{z}{z_0})^2}$ is the radius of the beam along the propagation direction and $z_0 = \frac{\pi W_0^2 n}{\lambda}$, $R(z) = \frac{z^2+z_0^2}{z}$ is the curvature radius of the beam for a z position, $k = \frac{2\pi n}{\lambda}$ is the wavenumber, λ is the wavelength and n is the refractive index of the medium. $\psi(z) = \arctan\left(\frac{z}{z_R}\right)$ is the Gouy phase shift at the focus of the Gaussian beam.

In brief, the phase affecting the Gaussian beam consists of a forward propagating phase, a phase induced by defocus and a Gouy phase shift that takes place near the focus. In this simulation, we simulate the incident beam using a plane wave presented as:

$$E_i(z) = E_{i0}\exp(-i(kz)) \tag{4.2}$$

The interference term of both fields is therefore expressed as: $2Re[E_s \cdot E_i]$

We first simulate a numerical aperture of 1.25. Here we show the interference intensity, in which two cone-like radiation patterns of opposite signs are centered near the focus plane of the interferometric intensity. As shown in fig 4.10 , these constructive and destructive interferences occur along the propagation direction and are affected by the phase shift modifying the Gaussian beam. To estimate the influence of each phase, we present in fig the resulting interferometric profile when considering only the phase shift term only and the phase shift caused by defocus only, respectively.

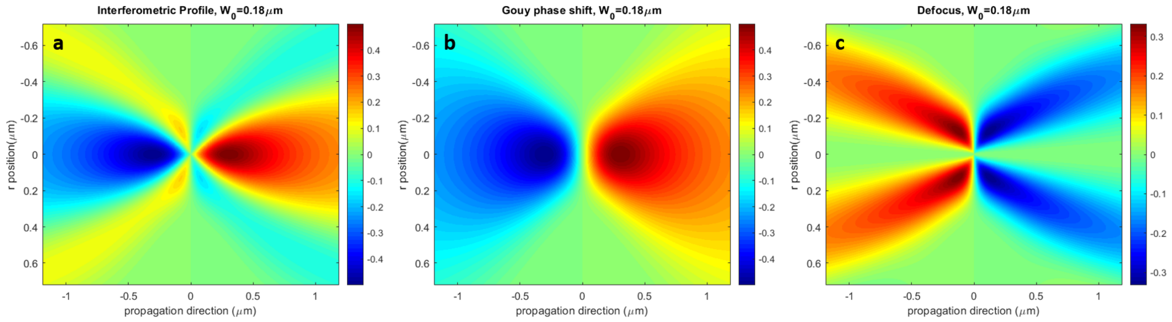

Figure 4.10: **2D profile of the interferometric signal**. **a** shows the interferometric signal, **b** and **c** represent the interferometric signal due to the Gouy phase shift and defocus only, repectively.

The interferometric intensity is sensitive to the phase variation along the propagation direction. Therefore, the effect of the axial phases induces two focuses on each side of the focal plane. When comparing the interferometric PSF to the scattering only or fluorescence PSF, the distance between the two focuses is about the depth of field estimated for usual fluorescence wide-field PSF as presented in fig 4.11. In this simulation, we can see that the position of the minimum and maximum intensity depends on the numerical aperture of the Gaussian beam. Here, we modified the waist of the gaussian beam from $0.18\mu m$ to $0.32\mu m$, to simulate a smaller numerical aperture. We would like to note that the interferometric intensity profile for each numerical aperture is extended over a longer distance compared to the depth of field estimated for wide-field fluorescence microscopy. In other words, the interferometric PSF represents the amplitude of the scattered field.

To note that the interferometric intensity alters between negative and positive values after removing the background offset. The total intensity collected consists of positive values only.

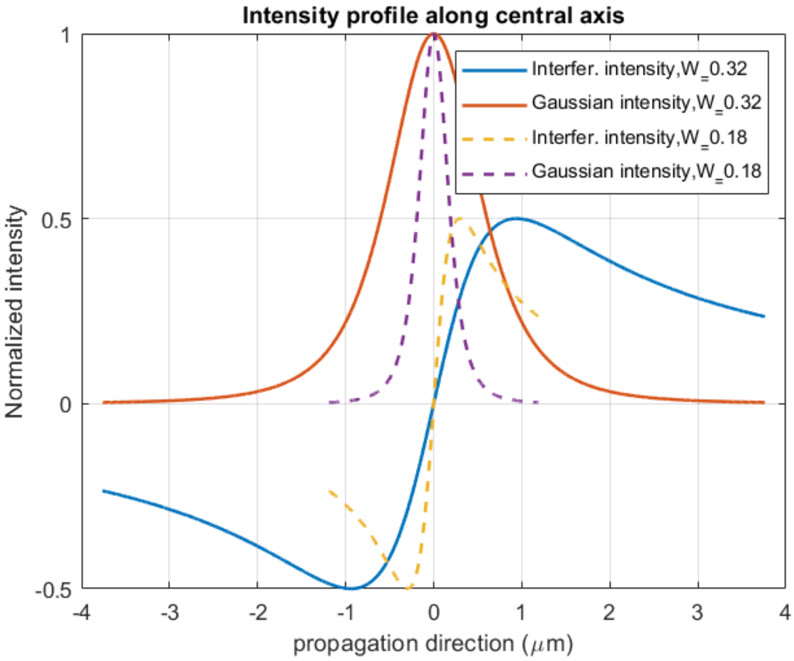

Figure 4.11: **Inteferometric and fluorescence intensity profile along the central axis for** $W_0 = 0.18$ **and** $0.32\ \mu m$. The interferometric intensity presented here is the intensity found after removing the background offset

We have shown in the previous section the interference profile of a Gaussian beam representing the beam scattered from the particle and incident collimated beam. We found that constructive and destructive interferences can be seen at each side of the focal plane for a collimated illumination. However, when tilting the illumination beam, we begin to detect constructive and destructive interferences simultaneously at both sides of the focal plane of the Gaussian beam. Here, the 2D profile of the interference intensity when the illumination beam is tilted by 18 degree angle.

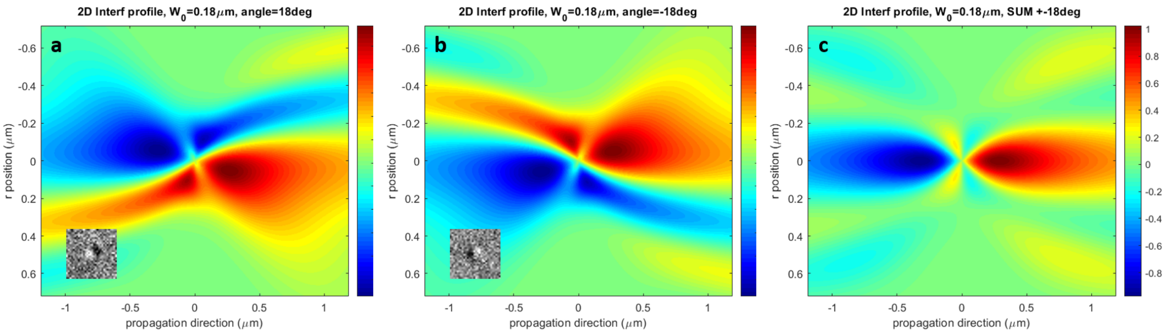

Figure 4.12: **2D profile of the interferometric intensity under tilted illumination (angle=18**deg). **a** and **b** show the interferometric signal for an illumination tilted by 18 and -18 degree, respectively.**c** represents the sum of the both interferometric intensity for both symmetrical angle illumination.

Interpretation of the simulated interferometric signal

In brief, we presented experimental measurements showing that the effective numerical aperture is about 0.54 even when using a higher NA objective lens. In a first approach, FDTD simulations show that the interferometric signal and the shape of the PSF depend on the numerical aperture of the objective lens. We were interested in the signal variation along the axial axis. Also, using a naive analytical model, we have noticed that the interferometric signal depends on the numerical aperture of the Gaussian beam and the axial position scales with the numerical aperture in use. Despite that, the simulations in the near field correspond to the analytical model using a plane reference wave and a Gaussian beam representing the scattered field from the particle; they do not fit the experimental measurements for high NA (NA>0.54).

However, we can notice in fig 4.12 a that the interference between the Gaussian beam and a plane wave is narrower in the lateral direction compared to fig 4.12b, in which we present the effect of the Gouy phase shift only. The narrowness can be explained by the involvement of the Gouy phase shift and the defocus, fig 4.12 b and c. The cancelation of the interferometric signal for wide angles can be explained by the phase opposition due to Gouy phase shift and defocus, respectively. This simulation considers the interference on the camera plane conjugated to the sample plane. Thus the involvement of both phases can induce the reduction of the effective collection NA.

We would like to note that we have detected simultaneously destructive and constructive double spots when tilting the illumination source. These observations have been confirmed in experimental measurements where we can see double spots altering between bright and dark depending on the position of the LED, as shown in fig 4.12. Thus, the use of high numerical illumination can be useful to saturate the camera's full well capacity but can be ineffective in terms of useful interferometric signal.

4.3 Increase the interferometric contrast

So far, we have been using incoherent light illumination sources based on high-power LEDs. These sources have some significant advantages when it comes to their remarkable power stability. Moreover, the setup is not sensitive to some unwanted artifacts due to the spatial coherence of the source itself or to other unwanted artifacts due to the speckle. However, we are limited by the luminance of the LED chip when trying to get a suitable illumination power for saturating our camera. With such incoherent source, we have been able to detect and track particles of SiO_2 of 50nm in diameter and viruses as small as 60nm.

In order to detect smaller virus particles, we have to increase the interferometric contrast. The most straightforward approach is to attenuate the reference beam while keeping the illumination close to the camera saturation. Indeed, having enough intensity power is needed to take fully take advantage of the shot-noise limit of the camera and to reduce the influence of the dark noise of the detector.

4.3.1 Speckle decorrelation

While LASER illumination can efficiently deliver a high amount of power, a new challenge arises because of the unwanted speckle patterns generated along the illumination beam path that degrades the image quality. One solution is to scan a focused illumination beam over the sample of interest. Indeed, rapid beam scanning illumination utilizes a pair of acousto-optic deflectors (AODs), which scan a focused beam across the sample, generating an even illumination profile while reducing speckle patterns observed in widefield iSCAT. This illumination approach has often been implemented in combination with a polarization-dependent method to separate the signal from the illumination path using a quarter-wave plate (QWP) and polarizing beamsplitter (PBS) in order to increase the collection efficiency. Here, the scanning and the acquisition speed rate of the camera can be high, about a few kHz [13, 14]. Another option is to use a wide field collimated beam to illuminate the sample. Here, the speckle patterns affect the interferometric signal and degrades the SNR of the signal of interest. Different methods can be employed to overcome the speckle limitations. The stability of the speckle, that is important for methods based on dynamic analysis, depends mainly on the characteristics of the laser, the stability of the optical set-up, and the acquisition rate.

If the speckle is stable for consecutive frames, the signal of interest can be retrieved by simple subtraction of the constant background, this concept can be applied to a stack of images, and here a moving average can be used to recover the signal of interest. This concept is mainly applicable when monitoring the interaction of particles or proteins of interest with a surface.

Therefore, we have to distinguish between the speckle pattern and the stability of the pattern. First, the laser speckle pattern depends mainly on the optical path of the laser beam. Therefore, if the speckle pattern is stable, one can retrieve the interferometric signal coming from weak scatterers. However, in practice, the speckle patterns fluctuate temporarily. In our case, the acquisition rate is relatively low compared to the fluctuation frequency of speckle pattern, a certain stability of the laser and of the setup is needed and large integration time to homogenize the beam profile. However, when interested in tracking small particles in a solution, the speckle pattern should be stable for a short exposure time, which is not trivial experimentally. The task gets more complicated when imaging weak scattering particles that requires low background fluctuations to localize the particles of interest that could be hidden by the background.

Perturbing the speckle pattern faster than the camera frame rate effectively averages it out. Several approaches have been explored in order to remove speckles from a laser imaging optical system, including rotating optical elements [15], oscillating scattering films [16] or mechanical agitation of a multimode optical fiber in which the laser is injected [17]. Recently the use of a long multimode optical fiber has been reported to reduce the speckle pattern at its output [18]. The modes propagate at different axial velocities because of the dispersion their paths in the fiber. The number of modes propagating in the fiber N depends on the normalized frequency of the fiber V where $\mathrm{N} \approx \mathrm{V}^2/2$ and $\mathrm{V} = 2\pi \mathrm{NA} a/\lambda$, where a is the core radius of the fiber, NA is its numerical aperture. N can be expressed as:

$$\mathrm{N} \approx \frac{2\pi^2 a^2 \mathrm{NA}^2}{\lambda^2} \tag{4.3}$$

Here, the concept is to prevent all these modes from interfering with each other by separating them by a distance larger than the coherence length of the laser $l_c < \frac{\Delta L}{N}$ and $l_c = 0.44\lambda^2/\Delta\lambda$ and therefore, the minimum fiber length can be estimated as:

$$L_{min} = \frac{4 l_c \pi^2 a^2 n_1}{\lambda^2} \tag{4.4}$$

where $n1$ is the refractive index of the core of the fiber and a is the core diameter of the fiber.

When assuming that all the modes propagating in the fiber are uncorrelated with no coupling between them, the speckle contrast can be approximated to $C = 1/\sqrt{(N)}$.

This method can be easy to implement and use, especially since it does not require moving elements. However, the main drawback of this method is the high attenuation of the violet beam that we use when propagating into the fiber. Nonetheless, usual fibers have a very low attenuation coefficient for wavelengths in the near IR and much stronger attenuation in the violet. Indeed, the attenuation coefficient increases quickly in dB when using shorter visible wavelengths.

Other LASER sources can be speckle free intrinsically due to the light source itself. Let us mention that the use of a random laser has been reported to be used for speckle-free imaging [19]. Random lasers are unconventional lasers in that they are made from disordered materials that trap light via multiple scattering; the modes are therefore inhomogeneous and highly irregular. With external pumping, many modes can lase simultaneously with uncorrelated phases. Their distinctly structured wavefronts combine to produce emissions with low spatial coherence. Pulsed mode-locked lasers represent a speckle free source for imaging in microscopy due to their ultra-short duration that insure non overlapping of different cavity modes. Therefore, the output beam of these lasers results in the conservation of spatial coherence and low temporal coherence. However, finding the appropriate wavelength is not always possible. Supercontinuum lasers might also present a solution for speckle-free imaging, which results in a broadband emission spectrum thanks to the superposition of all the cavity modes. However, all these solutions can be relatively expensive.

Another approach that has been reported to reduce speckle contrast is to pulse a laser at a high frequency (a few hundred KHz), [20]. Although we have tried to perform this approach, we did not succeed in reducing the speckle.

Finally, we have tried to average the speckle pattern to get a homogeneous illumination using a high-frequency mechanically deformable mirror. It is based on the use of a phase-randomizing deformable mirror technology fabricated by DYOPTYKA. This membrane has a high reflectivity of more than 95%, it is used to reduce the speckle patterns in the image plane. However, some random lower frequency vibration artifacts affect the background stability of the source. Moreover, these random patterns are complicated to remove because of their instabilities [21].

Therefore, to reduce the effect of the unwanted global fluctuations, we inject the beam reflected by the membrane mirror into a multi-mode fiber to mix the modes propagating in the fiber in order to homogenize the beam profile. Surprisingly, the beam profile becomes much more homogeneous, and the unwanted membrane fluctuations are not visible on the image plane. We want to note that we have been able to inject the reflected beam efficiently in the multi-mode fiber because of the small divergence angle of the deformable membrane, approximately 3° full-angle divergence [22] (the beam profile is not substantially broadened).

4.3.2 Speckle free imaging using a wide-field illumination

Delivering a high-power incident beam can be advantageous to increase the sensitivity of interferometric microscopy set-ups. However, scientific grade lasers used in advanced microscopy techniques can be expensive compared to inexpensive laser diodes that can deliver similar or comparable incident light power for a fraction of the cost. However, these inexpensive lasers usually have poor beam profile quality (high divergence or asymmetrical intensity profile). It can therefore be challenging to couple the light beam into a single-mode fiber; yet, they can be coupled with a good efficiency to multimode fiber, and therefore, a uniform profile can be retrieved at the output of the fiber. At this point, we did not reduce the speckle pattern but we only wanted to have a uniform beam profile at the output of the fiber.

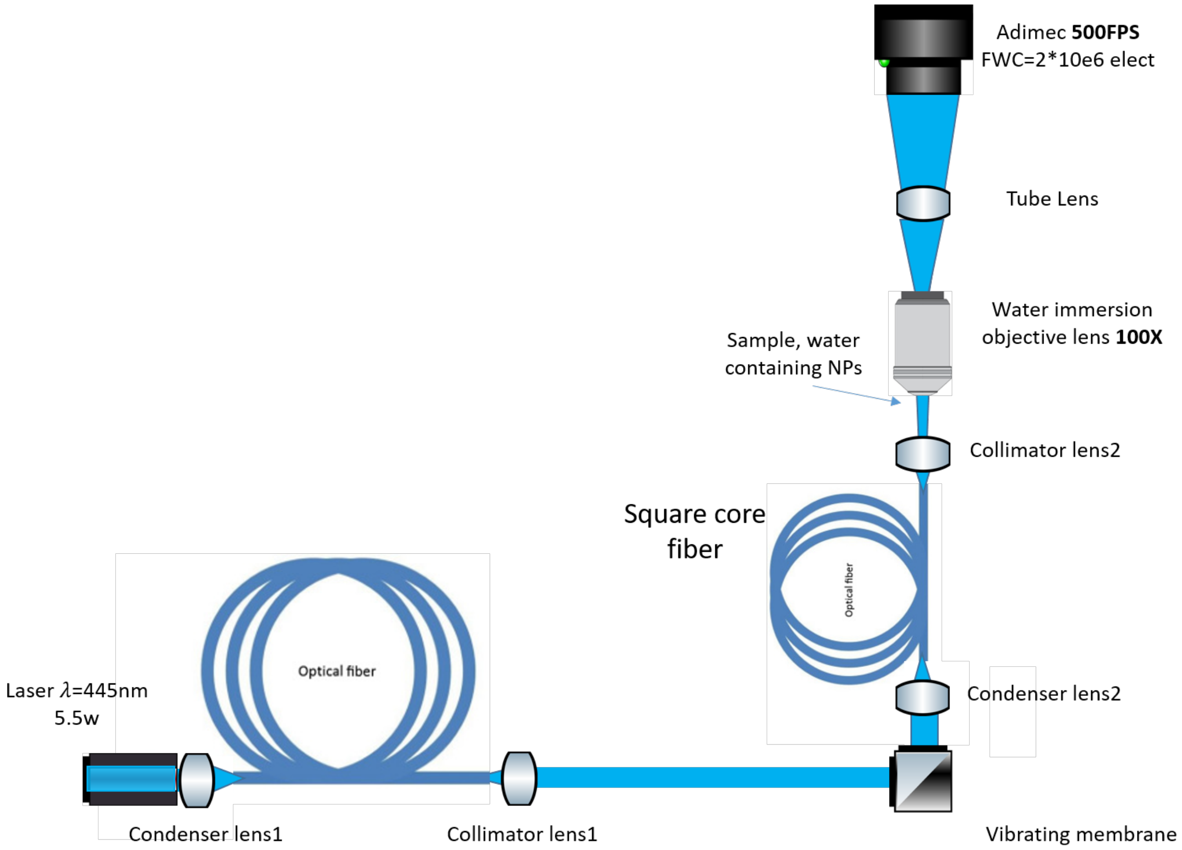

Figure 4.13: **Schematical representations of the optical set-up and wide-field illumination path using the deformable membrane mirror.**

Hence, as shown in fig 4.13, we coupled a low-cost 5.5 W, 445nm diode laser (generally used for engraving) into a multimode circular fiber of 100μm core diameter. The coupling efficiency is more than 80%, and at the output of the fiber, we placed a collimator lens to get a beam shape diameter of 2mm on the deformable mirror. It has been reported by D Schröder et al. that the use of a square core fiber decreases the speckle contrast compared to the case when using usual circular fibers [17]. Therefore, the beam reflected from the membrane is coupled using a condenser lens to a square core multimode fiber of 150*150µm^2 of 5m length, the use of a square core fiber has. Finally, a collimator is positioned at the output of the square fiber. Here, we fixed the collimator on a translation stage to get a micrometric adjustment of the position of the incident beam.

With this approach, we have been able to deliver high power illumination intensity with small divergence in the field of view. The primary benefit of using this approach compared to high-power LEDs is the ability to concentrate the illumination intensity on an adapted field of view without being limited by the size and the divergence of the LED chip. Furthermore, the use of the square core multimode fiber presents a homogeneous, speckle-free, top-hat illumination on the sample plane. Indeed, the addition of the square fiber after the deformable mirror drastically reduces the effects of the membrane's unwanted vibrations and allows us to reach a shot-noise limited level when removing the background offset. However, we would like to note that we had more than a twofold increase in noise value (of the standard deviation of the background) in addition to fluctuations of spatial artifacts degrading the signal when not using the square fiber. The effect of the vibrating membrane can be seen in fig 4.14. We can see about a five-fold decrease in terms of the standard deviation of the background level when switching on the membrane. So far, we have presented the illumination path. With this approach, we can have a wide field homogenized illumination with the possibility of increasing the power illuminating the sample.

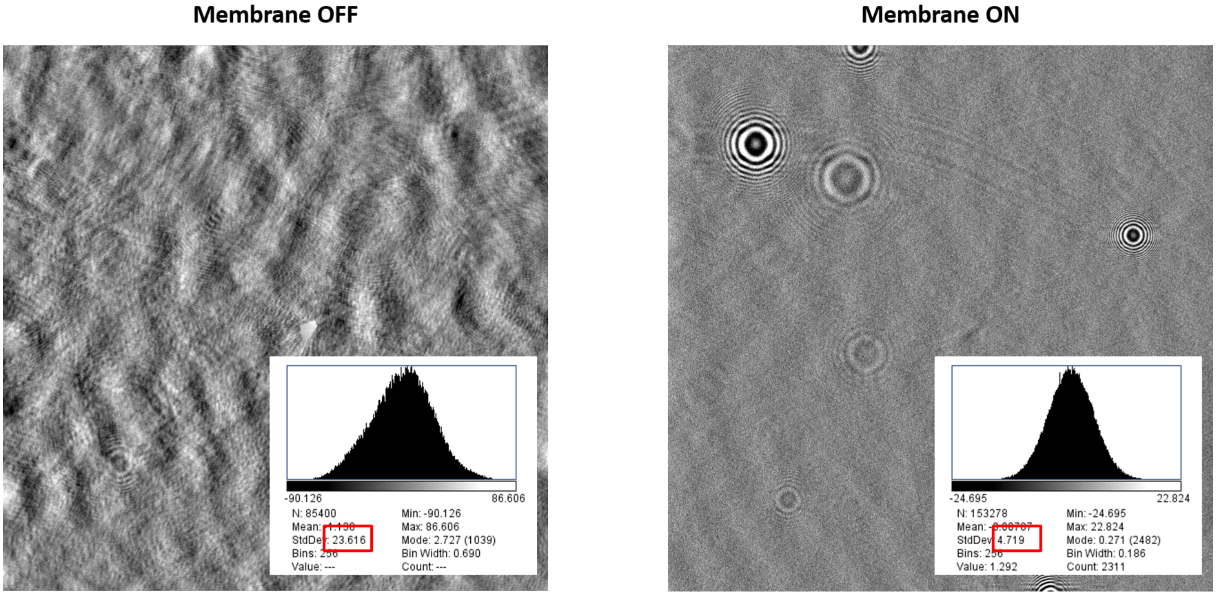

Figure 4.14: **Effect of the deformable mirror membrane on the background noise level.**

4.3.3 Attenuation of the incident beam for contrast enhancement

An attractive way to enhance the interferometric contrast of weak scatterers is to attenuate the incident beam in the back focal plane of the objective lens. This approach is especially interesting for a quasi-collimated wide-field illumination in transmission

Moreover, the concept here is to use a dot attenuator to reduce the transmission of the low numerical aperture incident light. The interferometric contrast scales proportionally to the square root of the attenuation of the incident beam, as long as we can saturate the camera, the attenuation affects the reference beam and not the sample, as presented in the interferometric contrast in chapter 2. In theory, the interferometric contrast increases tenfold when the reference beam is reduced by 100, for the same saturation level of the camera. However, when blocking the incident beam totally in the back focal plane, we retrieve the dark field case in which we do not use the benefit of interferometric detection.

Usually, the attenuator consists of a thin metallic layer coated onto a glass window [23]. Here, the degree of attenuation of the incident light can be tuned by changing the thickness of the metallic layer depending on the characteristics of the dynamic range, acquisition speed, and the amount of the incident power intensity.

The method can be applied to different types of objective lenses. In practice, usually, the real position of the back focal plane is inside the objective lens, and therefore accessing the back focal plane is not always possible. Therefore, a relay lens system is used to access the back focal plane using two lenses of similar focal distances to project the back focal plane, as shown in fig 4.15.

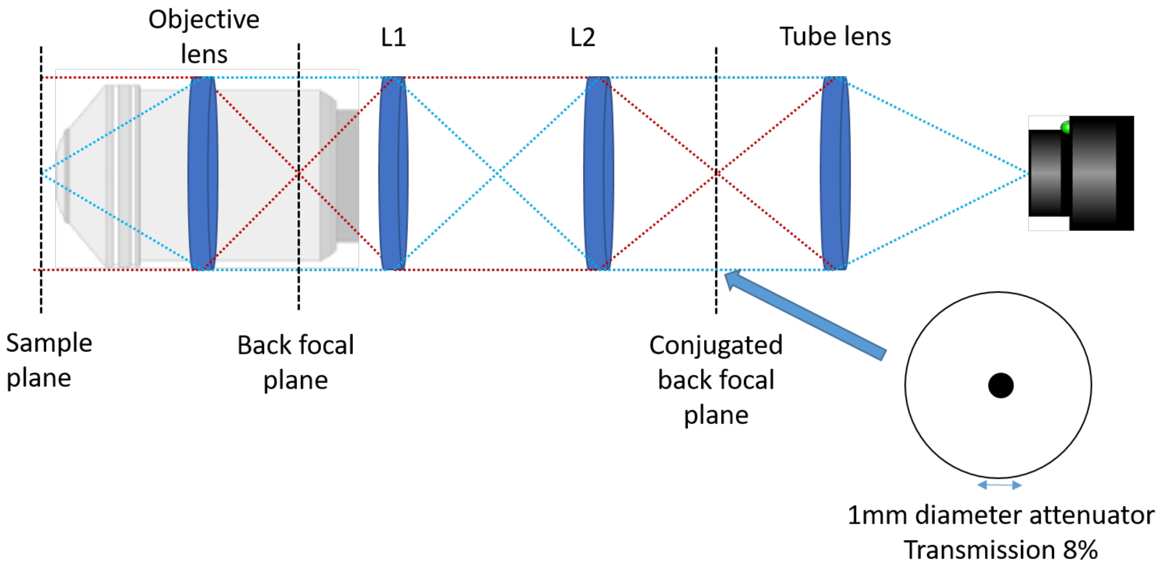

Figure 4.15: **Schematical representation of optical set-up used to attenuate the reference beam in the back focal plane of the objective lens.**

We used two identical lenses of 50mm focal lengths to project the back focal plane and attenuate the reference beam. The mask used consists of a dot attenuator of 15nm thick aluminum coating. The transmission of the mask depends on the thickness of the metallic layer, as shown in fig 4.16.

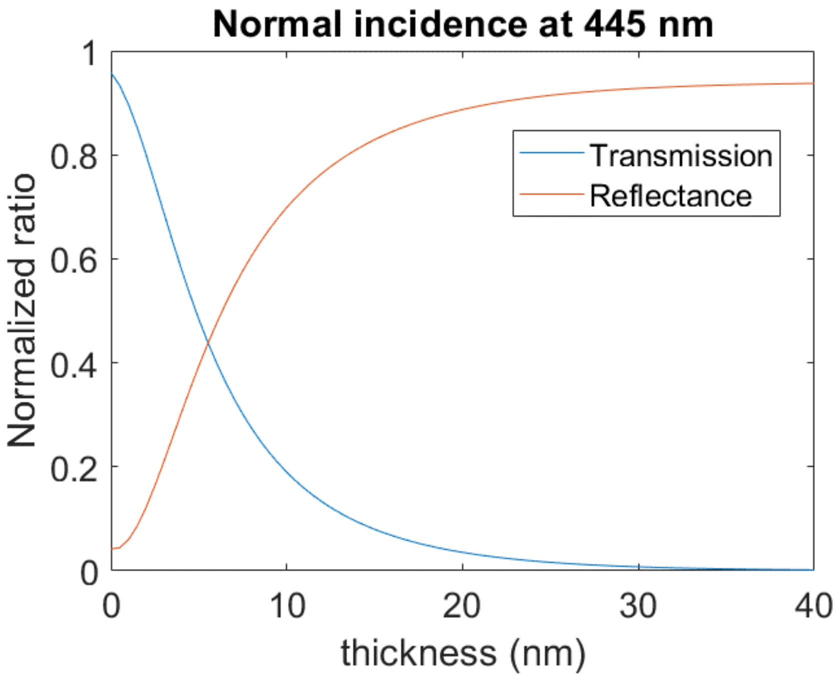

Figure 4.16: **Transmission and Reflectance of an Aluminum layer as function of the layer thickness in nm. The standard deviation of the background is about 3.5 (shot noise limited) for 12bit images**

Using this mask, about 8% of the initial incident light is transmitted to the camera. In theory, this attenuation would increase the interferometric of a factor of at least 8. We used the Olympus water dipping objective lens(100x, NA=1). The size of the back focal plane is estimated to be about 5.5 mm in diameter; the dot attenuator of 1mm in diameter corresponds to the low numerical aperture illumination angle and does not affect the interferometric intensity coming from the higher numerical aperture due to the scattered field.

Using this illumination configuration, we have measured more than a six-fold increase of the interferometric SNR of particles of SiO_2 nanoparticles of 50nm in diameter compared to LED illumination, as shown in fig4.17.

4.3.4 Setup performances and small virus detection

We have used this optical set-up to detect smaller viruses that we were not able to detect before. Therefore, for such small particles a higher diffusion coefficient can be expected. Thus, we have reduced the camera's exposure time to 0.8 ms to freeze the moving particles during the acquisition time and reduce the localization error of the spots, as presented in section 2.4.1. In addition, we attenuated the reference beam even more using a 18nm Al coating in the back focal plane, about 4% of the initial beam is only transmitted through the focal plane.

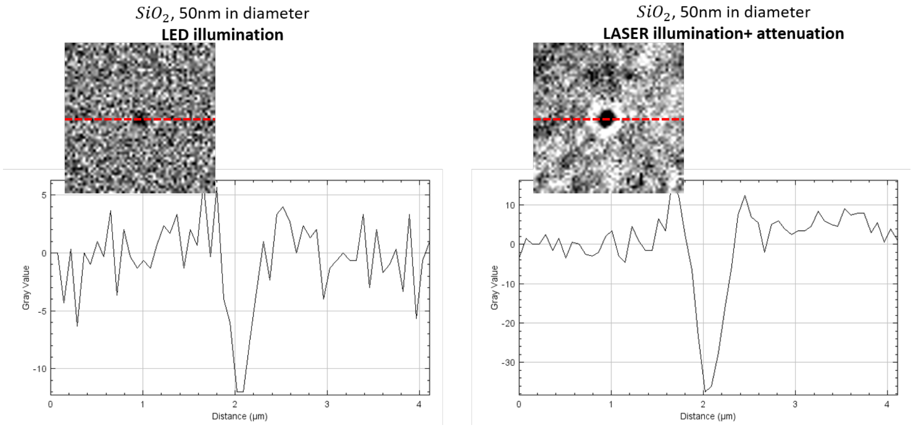

Figure 4.17: **Comparison between the interferometric signal of SiO_2 NP of 50nm in diameter using LED and LASER illumination when attenuating the reference beam**

First, we have tracked SiO_2 nanoparticles of 30nm in diameter. Then, we studied small biological samples, Bacteriophage MS2, having an icosahedral shape with a diameter about 27nm, and Adeno-Associated Viruses (AAV), having a diameter about 20-25nm. The estimated diffusion coefficient, as well as the maximum intensity, is presented in fig4.18.

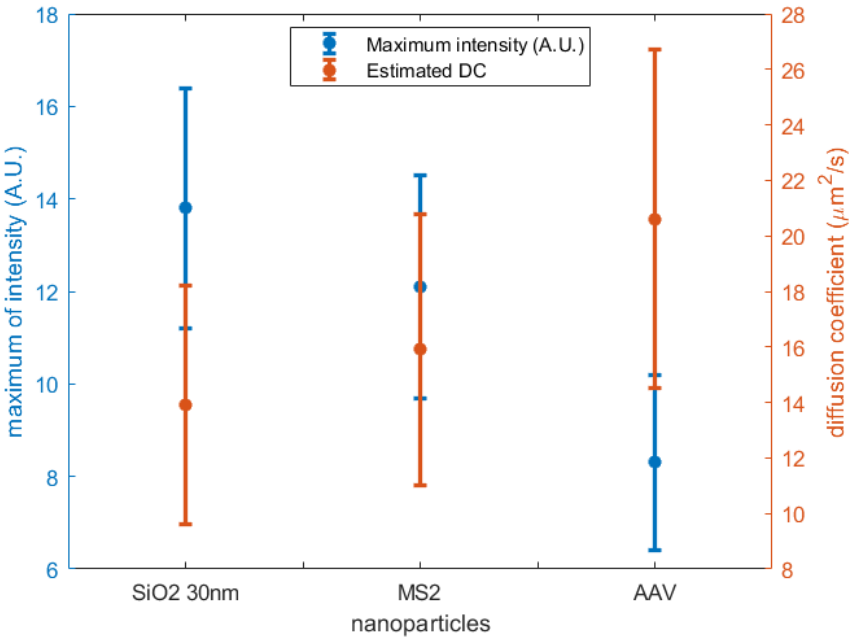

Figure 4.18: **Estimated diffusion coefficient and interferometric intensity for small viruses.**

We have done preliminary tests with a higher attenuation of the reference beam, but the challenge is to follow the Brownian motion of small particles with high accuracy. We can see in fig4.18 that the standard deviation of the diffusion coefficient is relatively large since we follow the particles for a short time interval while the particle is in the volume of detection. However, it is possible to increase the acquisition rate of the camera only when a smaller area of the detector is in use (ROI). This use can be practical to estimate the diffusion coefficient of smaller nanoparticles better.

4.3.5 Conclusion

These first results with an improved signal to noise ratio and a large field of view open the path to the promising systematic characterization of AAV viruses that are of importance for the pharma industry.

We would like to mention that at 30nm and below, the field is fully located on the particle, and the $diameter^3$, d^3 dependency of the interferometric signal could be reached within the experimental error and the uncertainty on the AAV, [24, 25] and MS2 virus size (between 20 and 25nm for the AAV) as can be seen in fig4.18.

However, it is possible to increase the acquisition rate of the camera, even though the region of interest (ROI) will be smaller in that case. This modification can be practical for a better estimation of the diffusion coefficient of smaller nanoparticles. In terms of power incident on the sample plane, we have been able to reach more than 500mW, and thus we have enough power to increase the attenuation in the back focal plane and saturate the camera for faster acquisition speed.

Bibliography

[1] Scott Prahl. https://omlc.org/cgi-bin/mie_angles.cgi?diameter=0.01&lambda_vac=0.455&n_medium=1.33&nr_sphere=1.45&ni_sphere=0&n_angles=100&density=0.1. 68

[2] Zhongya Qin, Congping Chen, Sicong He, Ye Wang, Kam Fai Tam, Nancy Y Ip, and Jianan Y Qu. Adaptive optics two-photon endomicroscopy enables deep-brain imaging at synaptic resolution over large volumes. *Science advances*, 6(40):eabc6521, 2020. 69

[3] James G McNally, Chrysanthe Preza, José-Angel Conchello, and Lewis J Thomas. Artifacts in computational optical-sectioning microscopy. *JOSA A*, 11(3):1056–1067, 1994. 69

[4] Michael Pircher and Robert J Zawadzki. Review of adaptive optics oct (ao-oct): principles and applications for retinal imaging. *Biomedical optics express*, 8(5):2536–2562, 2017. 69

[5] Donald T Miller and Kazuhiro Kurokawa. Cellular-scale imaging of transparent retinal structures and processes using adaptive optics optical coherence tomography. *Annual review of vision science*, 6:115–148, 2020. 70

[6] Peng Xiao, Mathias Fink, and A Claude Boccara. Full-field spatially incoherent illumination interferometry: a spatial resolution almost insensitive to aberrations. *Optics letters*, 41(17):3920–3923, 2016. 70

[7] Ugo Tricoli and Rémi Carminati. Modeling of full-field optical coherence tomography in scattering media. *JOSA A*, 36(11):C122–C129, 2019. 70

[8] Amaury Badon, Victor Barolle, Kristina Irsch, A Claude Boccara, Mathias Fink, and Alexandre Aubry. Distortion matrix concept for deep optical imaging in scattering media. *Science advances*, 6(30):eaay7170, 2020. 70

[9] Victor Barolle, Jules Scholler, Pedro Mecê, Jean-Marie Chassot, Kassandra Groux, Mathias Fink, A Claude Boccara, and Alexandre Aubry. Manifestation of aberrations in full-field optical coherence tomography. *Optics Express*, 29(14):22044–22065, 2021. 70

[10] James C Wyant and Katherine Creath. Basic wavefront aberration theory for optical metrology. *Applied optics and optical engineering*, 11(part 2):28–39, 1992. 74

[11] Kane Yee. Numerical solution of initial boundary value problems involving maxwell's equations in isotropic media. *IEEE Transactions on antennas and propagation*, 14(3):302–307, 1966. 75

[12] Bo Zhang, Josiane Zerubia, and Jean-Christophe Olivo-Marin. Gaussian approximations of fluorescence microscope point-spread function models. *Applied optics*, 46(10):1819–1829, 2007. 77

[13] Ching-Ya Cheng, Yi-Hung Liao, and Chia-Lung Hsieh. High-speed imaging and tracking of very small single nanoparticles by contrast enhanced microscopy. *Nanoscale*, 11(2):568–577, 2019. 81

[14] Jaime Ortega Arroyo, Daniel Cole, and Philipp Kukura. Interferometric scattering microscopy and its combination with single-molecule fluorescence imaging. *Nature protocols*, 11(4):617–633, 2016. 81

[15] Tim Stangner, Hanqing Zhang, Tobias Dahlberg, Krister Wiklund, and Magnus Andersson. Step-by-step guide to reduce spatial coherence of laser light using a rotating ground glass diffuser. *Applied Optics*, 56(19):5427–5435, 2017. 81

[16] Joran Deschamps, Andreas Rowald, and Jonas Ries. Efficient homogeneous illumination and optical sectioning for quantitative single-molecule localization microscopy. *Optics express*, 24(24):28080–28090, 2016. 81

[17] Daniel Schröder, Joran Deschamps, Anindita Dasgupta, Ulf Matti, and Jonas Ries. Cost-efficient open source laser engine for microscopy. *Biomedical Optics Express*, 11(2):609–623, 2020. 81, 84

[18] Egidijus Auksorius, Dawid Borycki, Piotr Wegrzyn, Ieva Žičkienė, Karolis Adomavičius, Bartosz L Sikorski, and Maciej Wojtkowski. Multimode fiber as a tool to reduce cross talk in fourier-domain full-field optical coherence tomography. *Optics Letters*, 47(4):838–841, 2022. 81

[19] Brandon Redding, Michael A Choma, and Hui Cao. Speckle-free laser imaging using random laser illumination. *Nature photonics*, 6(6):355–359, 2012. 82

[20] David Dulin, Stephane Barland, Xavier Hachair, and Francesco Pedaci. Efficient illumination for microsecond tracking microscopy. *PloS one*, 9(9):e107335, 2014. 82

[21] Egidijus Auksorius, Dawid Borycki, Patrycjusz Stremplewski, Kamil Liżewski, Slawomir Tomczewski, Paulina Niedźwiedziuk, Bartosz L Sikorski, and Maciej Wojtkowski. In vivo imaging of the human cornea with high-speed and high-resolution fourier-domain full-field optical coherence tomography. *Biomedical Optics Express*, 11(5):2849–2865, 2020. 82

[22] Shevlin Fergal. High-frequency homogenization of laser illumination through stationary multimode optical fiber. *The 11th Laser Display and Lighting Conference (LDC2022)*, 2022. 83

[23] Daniel Cole, Gavin Young, Alexander Weigel, Aleksandar Sebesta, and Philipp Kukura. Label-free single-molecule imaging with numerical-aperture-shaped interferometric scattering microscopy. *ACS photonics*, 4(2):211–216, 2017. 85

[24] Liam Cole, Diogo Fernandes, Maryam T Hussain, Michael Kaszuba, John Stenson, and Natalia Markova. Characterization of recombinant adeno-associated viruses (raavs) for gene therapy using orthogonal techniques. *Pharmaceutics*, 13(4):586, 2021. 88

[25] Nicholas J Szerlip, Stuart Walbridge, Linda Yang, Paul F Morrison, Jeffrey W Degen, S Taylor Jarrell, Joshua Kouri, P Benjamin Kerr, Robert Kotin, Edward H Oldfield, et al. Real-time imaging of convection-enhanced delivery of viruses and virus-sized particles. *Journal of neurosurgery*, 107(3):560–567, 2007. 88

Chapter 5

Label free optical transmission tomography for biosystems: intracellular structures and dynamics and in vivo tests

Contents

In this chapter, we would like to introduce a new Full-Field Optical Tomography method (publication under review), working in Transmission with a sectioning ability of a few micrometers linked to the numerical aperture of the microscope objective. We call it FFOTT, and the sectioning has been discovered by observing dynamical effects (as we usually do with Full-Field Optical Coherence Tomography (FFOCT)) induced by intracellular movements. However, it could also be induced by modulation of the sample/objective distance, as we will see in the submitted paper included in this chapter.

5.1 Static and Dynamic Full-Field Optical Coherence Tomography

Our laboratory has proposed a new, en-face version of the scanning popular Optical Coherence Tomography technique (OCT). First, let us point out that our interferometric approach uses a spatially incoherent source and a Linnik configuration, as seen in fig 5.1. Optical sectioning is obtained when the optical path between the beam splitter and the slice of interest is equal to the path between the beam splitter and the reference mirror. The sectioning value is linked to the spectral coherence length of the source and is typically from 1 to 10 micrometers for an incoherent LED.

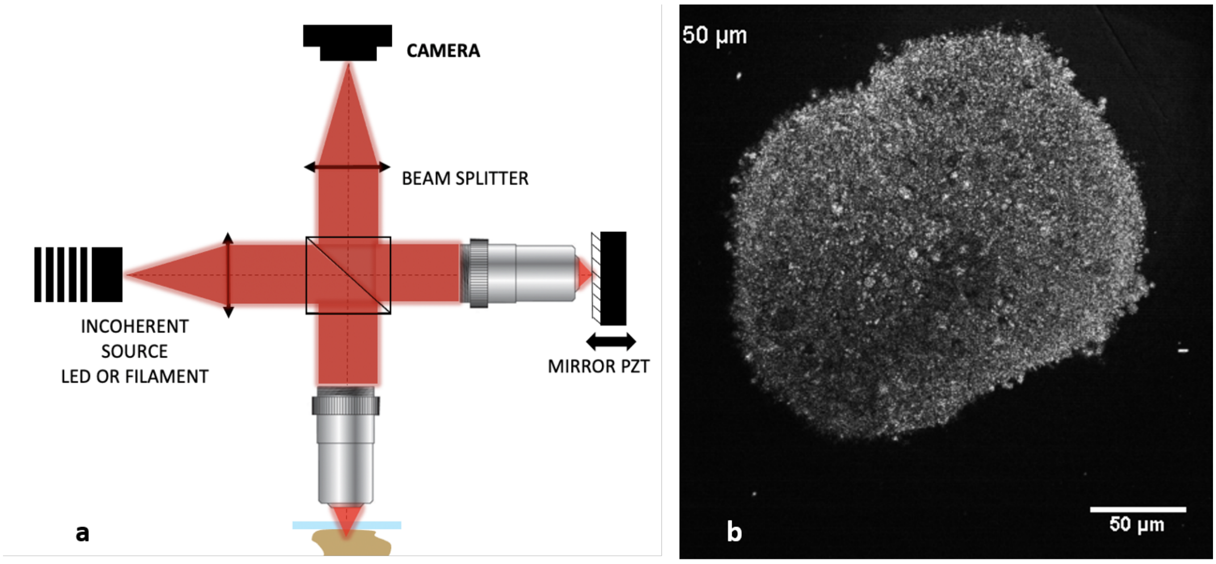

Figure 5.1: **FFOCT setup and tomographic images 50μm deep in the sample. a** represents a scheme of a typical FFOCT setup using a Linnik interferometer, and **a** shows an image of retinal organoids (using a piezo motor to induce path modulation in the reference arm)[1].

More recently, our laboratory introduced a new way of revealing cell activity: we block the sample modulation and let the intracellular organelles modulate the path difference in the sample arm, as shown in fig 5.2. Therefore, using the fluctuations of the interferometric signal, we retrieve the 2D dynamic activity of the sample when processing the acquired images.

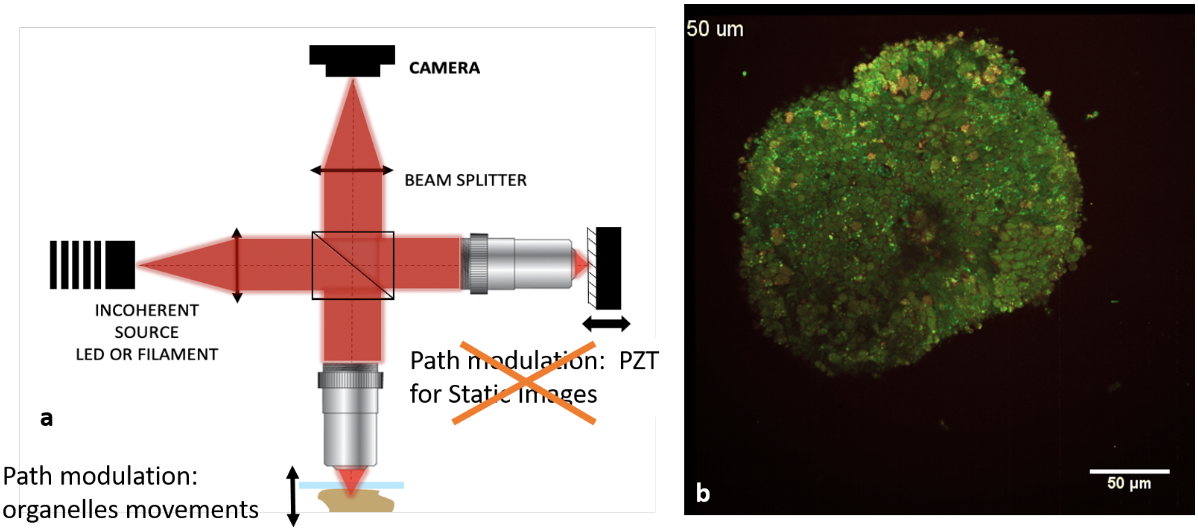

Figure 5.2: **Dynamic FFOCT setup and tomographic images $50\mu m$ deep in the sample.** **a** represents a scheme of a typical D-FFOCT setup, and **a** shows an image of retinal organoids (based on the organoids movement in the sample) [1].

5.1.1 Introduction

It is well-known that an object positioned outside of the optical microscope's focus stays visible and produces a blurred image. This presents a major problem for microscopy: an image of interest from a thin depth-of-focus slice can be completely hindered by the superimposed blurred background from the out-of-focus sample volume. With a goal to suppress the background and reveal only the relevant in-focus signals, multiple techniques were developed. These are frequently referred to as 'optical sectioning' methods. These methods are numerous and show great diversity in physical and engineering principles that underlie them; therefore, we will restrain ourselves to the most common methods. Optical sectioning methods can be classified into general types: methods physically blocking the out-of-focus light before detection, like confocal microscopy [2], methods filtering the out-of-focus light in post-processing [3], light sheet methods illuminating a single in-focus plane perpendicular to the detection [4], structured illumination methods [5], phase contrast methods highlighting the refractive index changes [6], optical coherence tomography methods that obtain cross-sectional [7] and en face sections [8] using the interference of light of low temporal coherence.

One of the earliest and the most widespread optical sectioning methods is confocal microscopy (CM) [9], which uses a pinhole mask to physically block the out-of-focus light from reaching the detector. Interestingly, it was noticed that a further improvement in optical sectioning (and axial resolution) could be achieved by looking at the brightness of the scatterer [10]. More precisely, the visible intensity of the scatterer can be linearly correlated to its position by subtracting several images along the point-spread-function (PSF) slope. This approach of optical profiling is called differential confocal microscopy (DCM) and can also be used in a two-camera configuration (one before and one after the focus) [11]. Differential spinning disk (DSD) [5] confocal microscopy is another method that relies on two image subtraction. However, the images are different in the illumination patterns. Modern confocal systems use a combination of physical (block) and numerical filtering (image subtraction) to improve the background rejection and, therefore, the optical sectioning.

Although with a different principle, image subtraction is also used in full-field optical coherence tomography (FF-OCT) [8, 12]. FF-OCT uses an interferometer coupled with a low temporal coherence light source to produce interference between the reference light from the mirror and backscattered light from a thin section of the sample. The interference phase is modulated by moving the reference mirror with a piezo-electric motor. The difference between the consecutive phase-shifted images doubles the interference signal and rejects the background, thus producing an optical section. FF-OCT works directly in wide-field and does not require point-by-point scanning typical for confocal systems. Another particularity of FF-OCT and OCT techniques, in general, is that the thickness of the optical section is independent of the depth of field and can be much smaller than the latter (determined by the spectral bandwidth of the light source). Many applications were found for FF-OCT, including biopsy diagnostics [13], visualization of cell organoid dynamics [1, 14], in vivo retinal [15], and corneal imaging [16].

Up to now, FF-OCT was only used in backscattering configuration. In most cases, confocal microscopy uses a reflection configuration, although an elegant transmission geometry was also proposed [17].

On the contrary, the optical phase contrast methods are primarily transmission types. Transmission geometry natively enables interference between the light waves scattered by the sample and the waves transmitted without scattering (zero-order diffraction). By using one of the phase-contrast techniques, such as the classical one from Zernike [6, 18], differential interference contrast (DIC) microscopy [19] or defocusing microscopy [20] it is possible to convert phase variations caused by the light propagating through the thickness of the sample, into the intensity detectable by the camera. Although the optical sectioning is modest, the resulting image provides a contrasted view of the sub-cellular structures.

This chapter introduces a new optical sectioning method that works in transmission. The method takes advantage of the Gouy phase shift [21] - the well-known π phase shift that the light wave experiences in the optical focus. Gouy phase shift modulating the interference signal of freely moving nanoparticles across the focus was shown using coherent [22] and incoherent light sources [23]. Here we study overall still samples, so, instead of relying on the random Brownian motion, we modulate the position of the focus using the piezo-electric motor. Hence, the phase of the scattered light oscillates, causing a signal variation. Because the Gouy phase shift is localized at the focus of the objective, only the infocus light is modulated while the out-of-focus light stays unchanged. Processing images with different phases rejects the background and enhance the light from the depth-of-focus, thus producing an optical section. In this way, the optical sectioning is achieved by combining physical and numerical rejection of out-of-focus light (small depth-of-field of focusing optics combined with processing of phase-shifted images). In order to emphasize the transmission nature of the method and the fact that it works in full-field, we call it full-field optical transmission tomography (FF-OTT). First, we provide a basic theoretical framework for FFOTT. Then we test its performance by imaging single-cell diatoms and ex vivo samples. Finally, we demonstrate the ability of FF-OTT to image the metabolic dynamic signals in living cells.

5.2 Basic model of full-field optical transmission tomography

5.2.1 Working principle and optical set-up

The Gouy phase shift (GS) is a well-known π phase shift that a converging wave experiences as it passes through its focus. GS is a general property of all waves (light, sound, etc.) and applies to any converging/diverging waveform [24]. Despite its widespread nature, the possible physical origins of GS were proposed only recently, rooting back to the fundamental uncertainty principle [25] and Huygens principle [26].

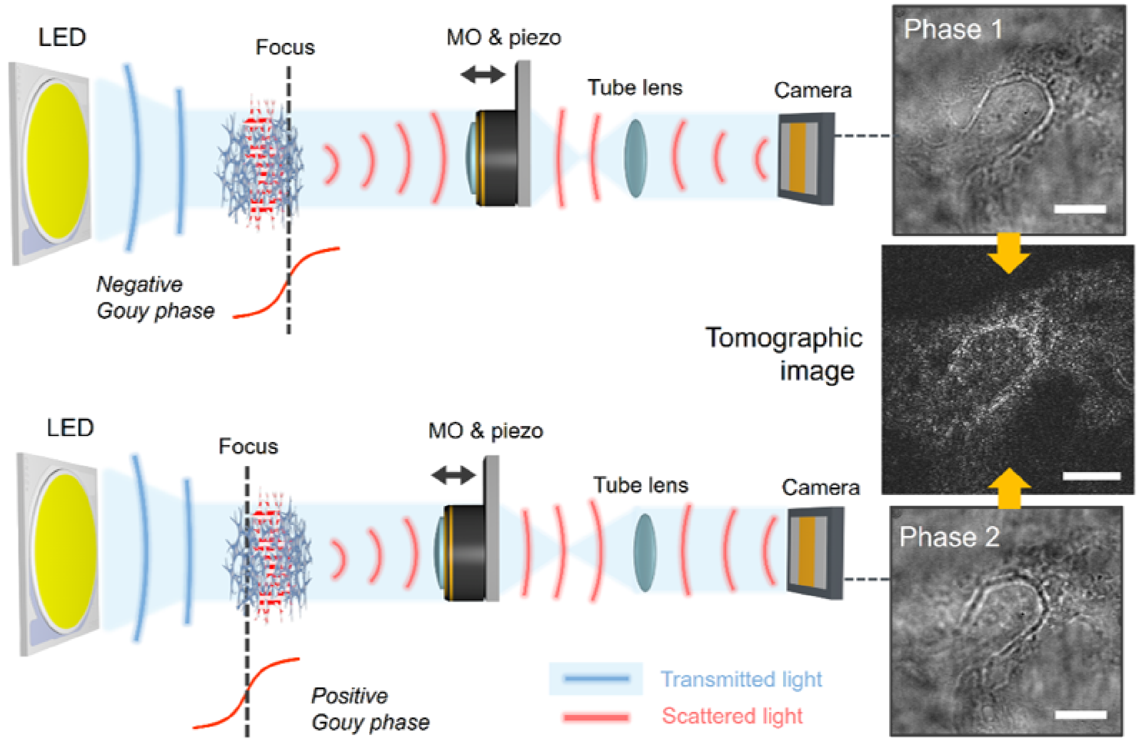

Figure 5.3: **Principle of FF-OTT: FF-OTT is based on interference of an illuminating wave and a wave scattered by the sample.** Shifting position of the microscope objective (MO) modulates the Gouy phase of the scattered wave. Subtraction of the 2 phase-shifted images removes the out-of-focus background, thus producing the tomographic image. The sample is a stromal keratocyte cell with visible nuclei from the ex vivo cornea. Scale bars are 10 µm.

Phase changes are not visible to the conventional light detectors that measure intensity. However, one can convert phase variations into intensity variations using interference of the transmitted light wave with the wave scattered by the sample. The transmission interferometer is shown in fig5.3. Light from the spatially incoherent source, such as a light-emitting diode (LED), is sent onto the sample. The sample scatters part of the incoming wave, and part is directly transmitted through the sample (zero-order diffraction) without scattering. The transmitted wave passes through the microscope objective, focusing close to its back focal plane, and gets projected onto the camera by the tube lens. On the opposite, the scattered wave is a diverging wave collected by the numerical aperture (NA) of the microscope objective, thus exhibiting the GS. The scattered wave gets focused on the camera and interferes with the transmitted light. In order to modulate the interference intensity of the scatterer, the microscope objective is mounted on the piezo-electric motor. Not every scatterer of the sample will exhibit sufficient GS, but only the scatterers within the DOF of the microscope objective (see the simulation below). By processing the images corresponding to different phases, one can reject the out-of-focus background and recover the optical section – the so-called FF-OTT tomographic image. Below, FF-OTT is analyzed theoretically using a paraxial Gaussian beam approximation and experimentally by imaging nanoparticles.

5.2.2 Simulation and experiment with still nanoparticles

Basically, in our experiments, the incoming wave illuminates the sub-wavelength scatterers such as the organelles in a cell volume generating a scattered field that is able to interfere with the incoming wave. We analyze the experiment using the Gaussian beam model, which provides particularly simple equations.

The two fields interfere producing intensity detected by the camera:

$$\mathrm{I_{total}} = |\mathrm{E_S}|^2 + |\mathrm{E_T}|^2 + 2\cdot \mathrm{Re}\left\{\mathrm{E_S}\cdot \mathrm{E_T^*}\right\} \tag{5.1}$$

The real interference term:

$$\mathrm{Re}\left\{\mathrm{E_S}\cdot \mathrm{E_T^*}\right\} = \mathrm{E_{S0}}\cdot \mathrm{E_{T0}}\cdot \frac{\mathrm{z/z_0}}{1+(\mathrm{z/z_0})^2} \tag{5.2}$$

Where z_0 is the Rayleigh length, essentially equivalent to half of the depth-of-field. ES0 is the amplitude of the electric field.

Here we used a trigonometry relation to express the formula in terms of axial position instead of the waist value. In case of a small scattering particle, the interference term is hindered by a strong homogeneous background, and the scattered intensity is negligible. The goal of FF-OTT is to remove the homogeneous background and isolate the interference term only. Around the focus, where $z/z_0 << 1$ the expression of the interference term can be simplified:

$$\mathrm{Re}\left\{\mathrm{E_S}\cdot \mathrm{E_T^*}\right\} = \mathrm{E_{S0}}\cdot \mathrm{E_{T0}}\cdot \frac{z}{\mathrm{z_0}} \tag{5.3}$$

Hence, close to the focus the interference term evolves linearly with the axial distance to the focus, opening a possibility for tomography. The tomographic image is typically reconstructed by subtracting two images with a slightly different focus in this linear regime. Therefore, the background signal disappears and the tomographic signal turns:

$$I_{tomo} = I_{total1} - I_{total2} = 2E_{S0} \cdot E_{T0} \cdot \left[\frac{z}{z_0} - \frac{z-P}{z_0} \right] = 2E_{S0} \cdot E_{T0} \cdot \frac{P}{z_0} \tag{5.4}$$

with P being the piezo shift. It is interesting to note that the tomographic intensity can be increased by maximizing the piezo shift between the two images, as long as we stay within the linear part around the focus. A general rule of thumb, confirmed by a simulation, is that the linear region roughly corresponds to the half of the depth-of-field.

We simulated Equ5.2 using parameters: $NA = 0.5, n = 1.51$ (immersion oil), $\lambda = 455$ nm. The results are shown in fig5.4 a. One can see that the Gouy phase affects the intensity of the interfering waves. Intensity experiences an abrupt linear change within half of the $DOF = z_0 = 1.5\mu m$ and shows only a limited change outside of focus. The simplest way to get optical sectioning consists in subtracting the two successive images with the different phases leading to an enhanced signal from the area around focus and suppression of the background. The optical sectioning effect is illustrated in fig5.4 b. Sectioning can be achieved with any phase modulating step within the linear region. Smaller modulating step ($< z_0$) within this region improves optical sectioning by stronger suppression of the out-of-focus signals. On the other hand, the larger modulating step ($> z_0$) provides limited suppression of the background signals near the focus, as can be seen by the tails of the curve in fig5.4 b.

As an experimental test for this model, we recorded an axial point-spread-function (PSF) of a small dielectric TiO_2 particle (diameter $< \lambda$). At the same time, the size was large enough (100 nm) to ensure a sufficient optical signal. The experiment used 100X oil immersion ($n_{oil} = 1.51$) microscope objective (AmScope, PA100X-INF-IRIS) with NA set to 0.5. The lateral resolution of the system ($2w_0 = 0.5\mu m$) was greater than the particle size. The camera was oversampled (1 pixel corresponds to $0.07\mu m$), giving us the possibility to quantitatively explore the particle profile and brightness. The position of the objective was modulated with a piezo motor (NV 40/3 CLE, piezosystem Jena). Illumination from the blue (455nm) LED (M455L4, Thorlabs) was detected by the camera (PhotonFocus, MV-D1024E-160-CL-12) with a high full well capacity of $200000e-$. Results are shown in Figs5.4 c and d . One can see that intensity and the particle's brightness change depending on its position before or after the focus. By moving the piezo motor with 100 nm step, we get an intensity curve on the particle that resembles the theoretical one in fig5.4 a. At the same time, the intensity of the background stays largely unchanged.

Interestingly, the effect of transparent objects showing light or dark contours under the microscope in different ways varying with change of focus [6] was known long before Zernike used it to create a phase-contrast microscope in the 1930s [18]. More recently, this effect was used in electron microscopy [27] and optical microscopy of transparent homogeneous samples [20]. The wave curvature (defocus) was sufficient for such objects to explain the phase shift between the transmitted and scattered waves. Here, like in OCT, we explore objects that scatter light due to their internal heterogeneous microstructures. Our study suggests that for such micro-scattering objects, the Gouy shift also plays a role in the phase contrast of these methods. Furthermore, the intensity curve will result from the interplay of the Gouy and defocus effects for complex samples.

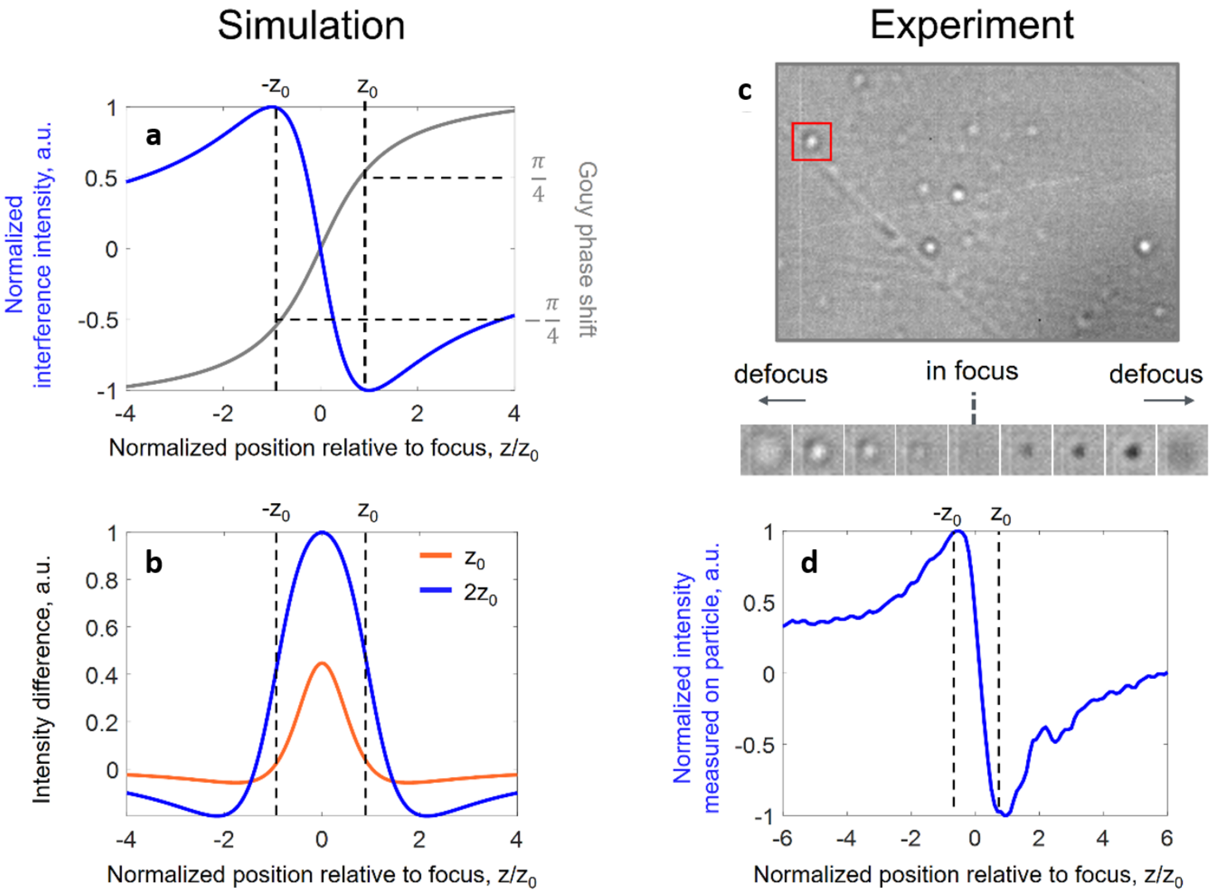

Figure 5.4: **FF-OTT simulation and experiment with nanoparticles**. **a** represents the Gouy phase shift and its effect on the intensity of interference light in the focus. DOF = 2z0 = 1.5 µm. **b** shows optical sectioning effect depending on the phase step of the piezo motor. The curves are obtained by subtracting two phase-shifted blue curves in **a and c**: image on the camera with defocused nanoparticles visible. **d** represents the experimental change of nanoparticle intensity depending on the position relatively to the optical focus

5.3 Experimental results

5.3.1 Diatoms

Diatoms are single-cell algae that are of importance for environmental studies. An extended discussion about the biology of diatoms can be found in [28] and the references therein. We used an experimental configuration similar to the one mentioned above. An optical slice can be retrieved by subtracting the two phase-shifted images. Alternatively, the objective can be moved sinusoidally, as in the integrated-bucket FF-OCT [29], to perform a lock-in detection and increase the sensitivity to small scatterers. Each image was acquired in 3 ms camera exposure time at 135 frames per second, resulting in a 15 ms acquisition time for one tomographic frame. Results are shown in fig5.5 FF-OTT suppresses the fuzzy background that is present in the direct camera images.

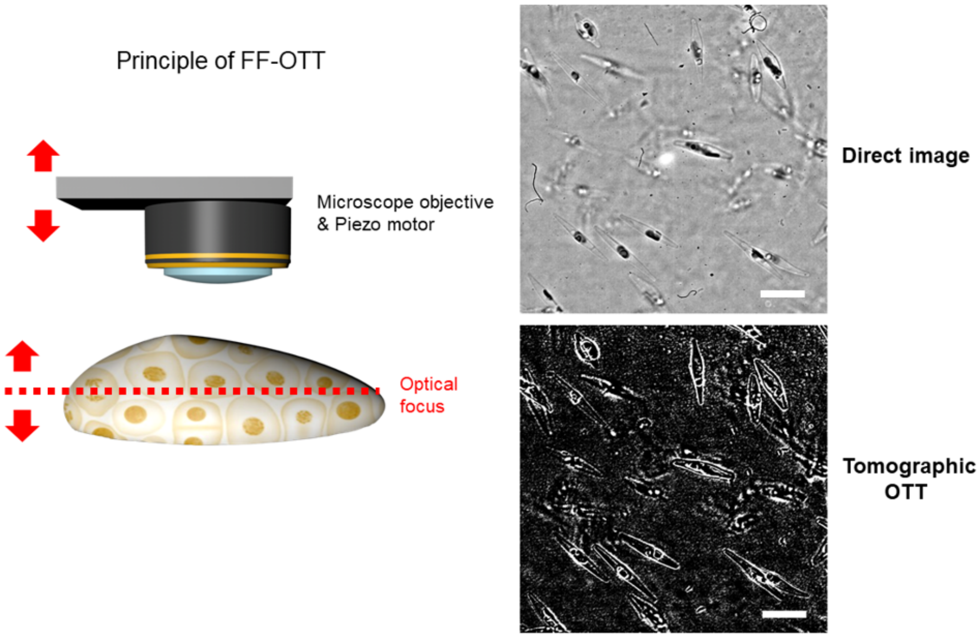

Figure 5.5: **FF-OTT in the study of diatoms.** Direct image refers to a transmission image acquired by the camera without additional processing. Tomographic OTT image was reconstructed from two direct images shifted by a half micrometer. The scale bars are 15 μm.

5.3.2 Ex-vivo cornea

The cornea is the most forefront transparent tissue that constitutes the eye. Therefore, its exploration is of great interest to medicine as it is a transplantable tissue. Furthermore, the multi-layer composition of the cornea makes its exploration with tomographic techniques particularly interesting and informative. In order to explore the cell organization, we used an optical system with a smaller magnification but a larger frontal distance. The microscope objective was water immersion ($n_{water} = 1.33$) 60X NA = 1.1 (NA = 0.5-0.6 filled) (LUMFI, Olympus). The theoretical lateral and axial resolutions were 0.6 and 1.4 µm, while the FOV was about 180 µm. Ex-vivo porcine and macaque corneas were obtained from the partner research institution (Institut de la Vision, Paris) as recuperated waste tissue from an unrelated experiment. They were dissected from the ocular globes within the two hours post-mortem and were imaged within the same day using FF-OTT. In order to limit the spherical aberration due to refractive index mismatch, we first imaged the epithelium and stroma at the front and then flipped the cornea to view the endothelium and stroma at the back.

Corneal images revealed different structures, including epithelial cells (40 µm) with nuclei (10 µm), stromal keratocyte cells with nuclei (15 µm), and endothelial cell mosaic (20 μm), as shown in fig5.6. However, the structures showed similar dimensions in FF-OCT and confocal microscopy [16, 30].

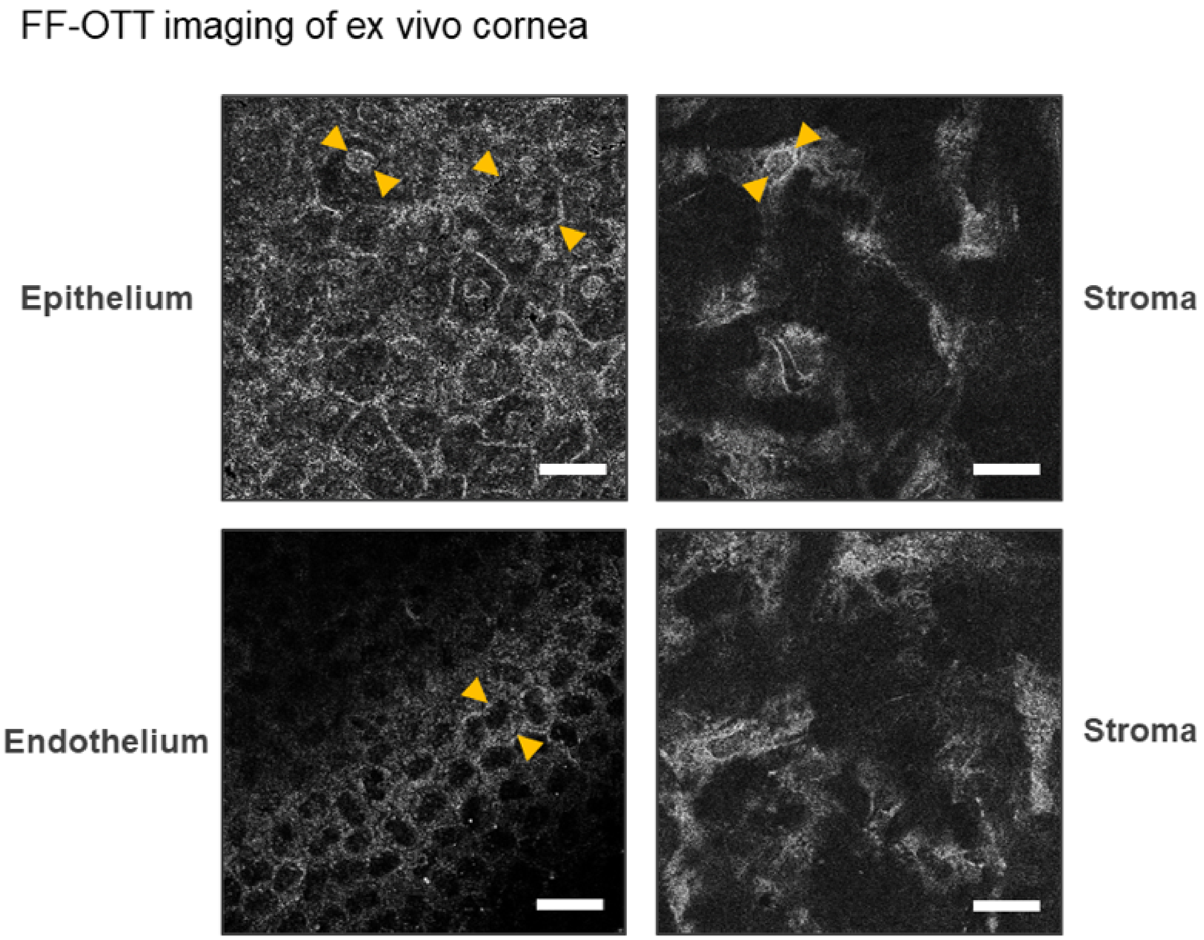

Figure 5.6: **FF-OTT images of ex vivo human cornea.** The stromal and endothelial images were acquired from the macaque cornea, while the epithelial image was taken from the porcine sample (epithelium in the macaque cornea deteriorated). Arrows highlight the epithelial cell nuclei (10 mum), epithelial cell cytoplasm (40 mum), stromal keratocyte cell nuclei (15 mum), and endothelial cell (20 µm).

5.3.3 Dynamic FF-OTT

One peculiar feature of FF-OTT is that it can also be used to study the metabolic dynamics of the cells. In this context, instead of moving the microscope objective, one can rely on the natural movements of the subcellular organelles. Thanks to the linearity of the axial interferometric response in FF-OTT, the axial displacements of the live scatterers are transferred into the intensity differences. The intensity fluctuation images contain information that can be used to compute the optical section as before and contain information to evaluate the active transport of the scatterers inside the cell. The dynamic FF-OTT signal also exhibits optical sectioning because the intensity strongly depends on the axial response only around the focal plane. This method is a transmission analog of another label-free method - dynamic FF-OCT that is being used in back-scattering [1, 14].

An extended analysis of dynamic FF-OTT application to diatoms can be found in a biology-oriented paper [28], while in this work, we demonstrate the promise of the method for imaging 2D cell cultures and 3D retinal layers. We first illustrate the dynamic FF-OTT method by studying the behavior of HeLa cells (93021013-1VL, Merck) grown on a coverslip in a Petri dish. The cells were positioned in the best focus of the FF-OTT device. Here we used a high resolution 100X oil immersion FF-OTT device mentioned above. FF-OTT acquired a time-lapse stack of 256 direct camera images in 3 seconds. The brightness of each pixel of the stack fluctuates with a certain average frequency and frequency bandwidth, reflecting the movements of the organelles located in that pixel. By assigning each variable to a respective channel in the HSV color map (H - avg. frequency, S – frequency bandwidth, V – brightness), one can create a colored dynamic FF-OTT image, fig. 5.7. The red color corresponds to the fast frequencies in these images, thus the fast-moving organelles.

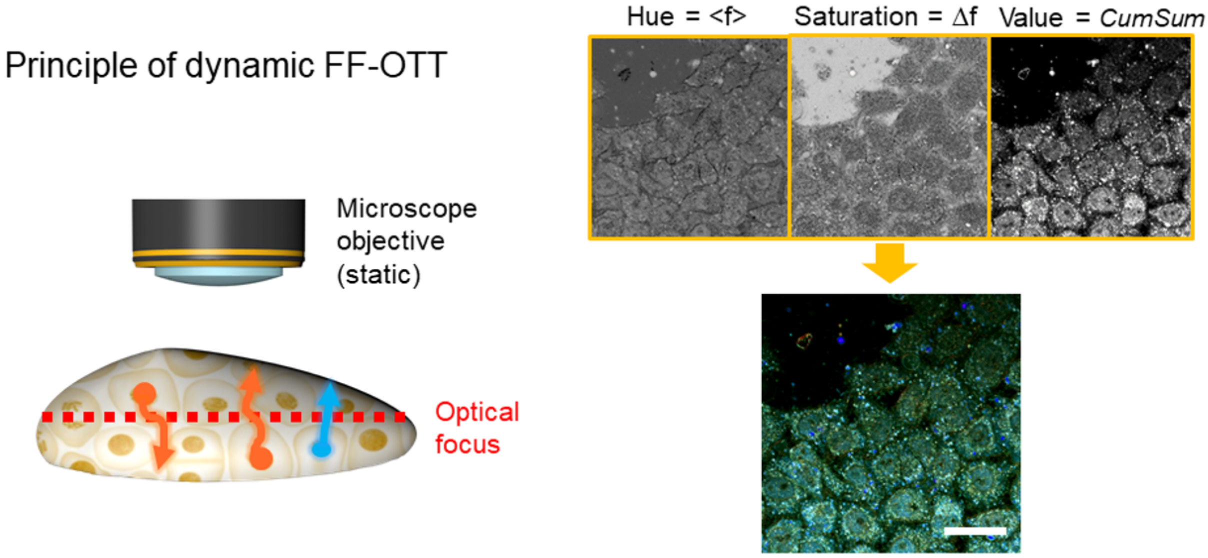

Figure 5.7: **Dynamic FF-OTT principle.** Instead of moving the optical focus, one can rely on natural movements of sub-cellular organelles around the optical focus for phase shifting. The stack of 256 direct images contains sufficient information to reconstruct a tomographic image with the cell metabolism encoded in color (blue = slow, red = fast). This is done by looking at the time evolution of each pixel of the stack and by measuring the average frequency of modulation <f.>, frequency range f, and cumulative sum (CumSum). Then HSV image is created by assigning these parameters to each channel. The scale bar is 20 μm.

In order to confirm that the color signal originates from the cell metabolism, we applied the sample the D-oxy-glucose, which inhibits glycolysis and stops part of the energy supply. The evolution of dynamic FF-OTT images is shown in fig**??**. As expected, the cytoplasm interferometric signal decreases as a function of time [31]. However, we also noticed a 2 to 5 times increase in dynamic signal from the nuclei. In order to better characterize these dynamics, we compared the standard deviation and the cumulative sum, following the method developed by Scholler [31]. We found that the normalized cumulative sum was about the same as the standard deviation (ratio 1.3) before adding the D-oxy-glucose, and it increased to a ratio of 2.5 after the addition. This result suggests that the random movement of scatterers within the nuclei is likely to be associated with a drift that makes it anomalous rather than a pure Brownian motion. Indeed, anomalous movements have already been described in the nucleus, and D-oxy-glucose has been shown to inhibit protein transport from the cytoplasm to the nucleus [32].

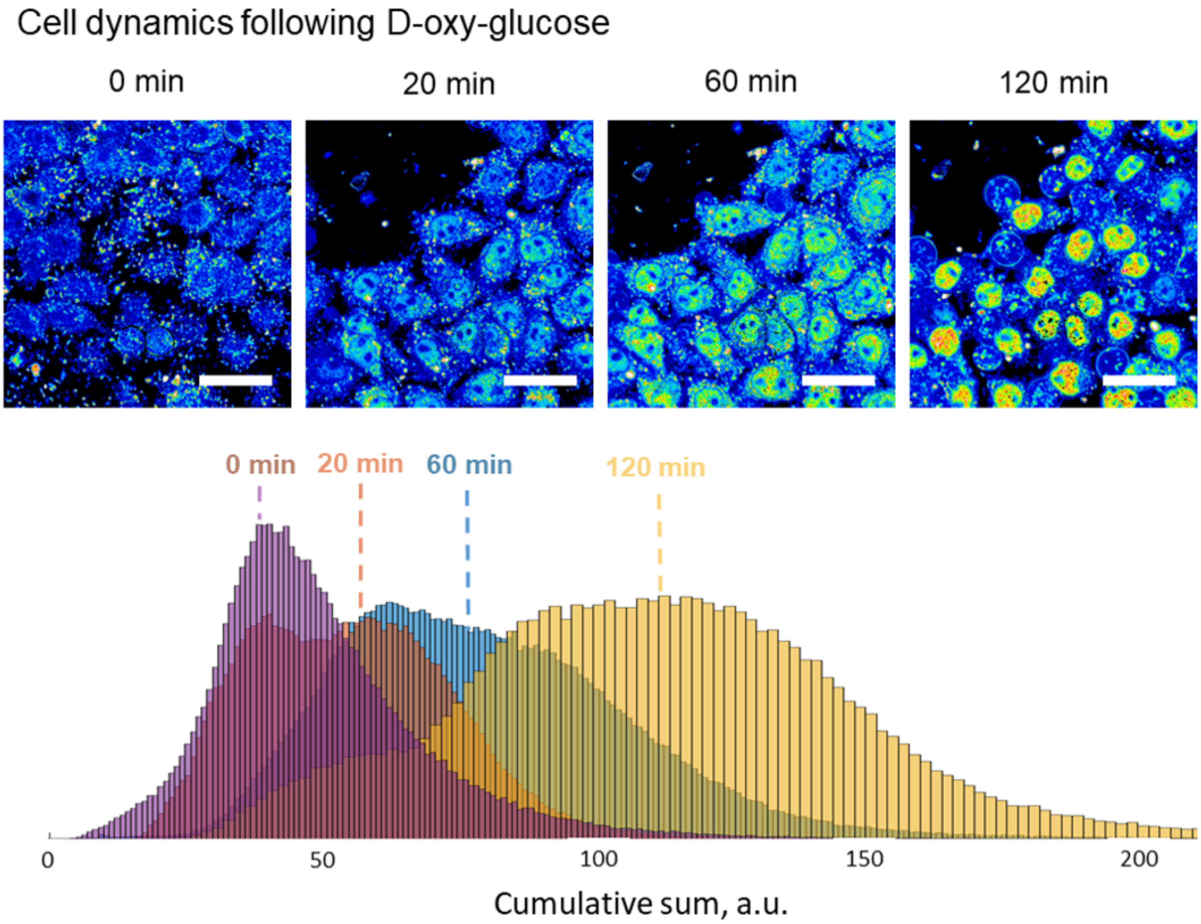

Figure 5.8: **Dynamic FF-OTT application, imaging HeLa cells metabolism.** The introduction of D-oxy-glucose partly blocks the cell energy supply resulting in the expected reduced dynamic signal from the cytoplasm and increased signal from the nuclei, as seen by FF-OTT. The histogram is calculated by measuring the cumulative sum signal at each pixel within the nuclei. The method did not require any fluorescent biomarkers. Scale bars are 20 μm.

Dynamic FF-OTT can be performed in cell cultures and thick samples like ex vivo pig retina. The retina was obtained from the partner research institution (Institut de la Vision, Paris); it was dissected from the ocular globe within two hours post-mortem and was imaged on the same day. The tissue was deposited on a simple coverslip and immersed in PBS. The drift in the liquid was causing occasional motion artifacts in the images. The light traveled through the total thickness of the retina while the ganglion cell layer, close to the retina's surface, was imaged. 256 images were acquired at each plane, separated by 2 µm, and one dynamic FF-OTT image was calculated at each plane. The direct intensity image, the static FF-OTT, and the dynamic FF-OTT images were combined to form a 3D image from a z-stack. The first layer of flat and large cells, possibly glial cells, is visible in dynamic FF-OTT, followed by a few planes, where large and small circular ganglion cells and their nuclei can be observed together with large axons in static FF-OTT. The retinal ganglion cells exhibit smaller amplitude but faster dynamics than the first class (blue) cells. Finally, the inner plexiform layer with many point-like synapses was visible, with the first few bipolar cells from the inner nuclear layer. Altogether, many different cells and features of the retina can be investigated by combining static and dynamic FF-OTT. We show in fig5.9 the retina image 50μm deep in the sample.

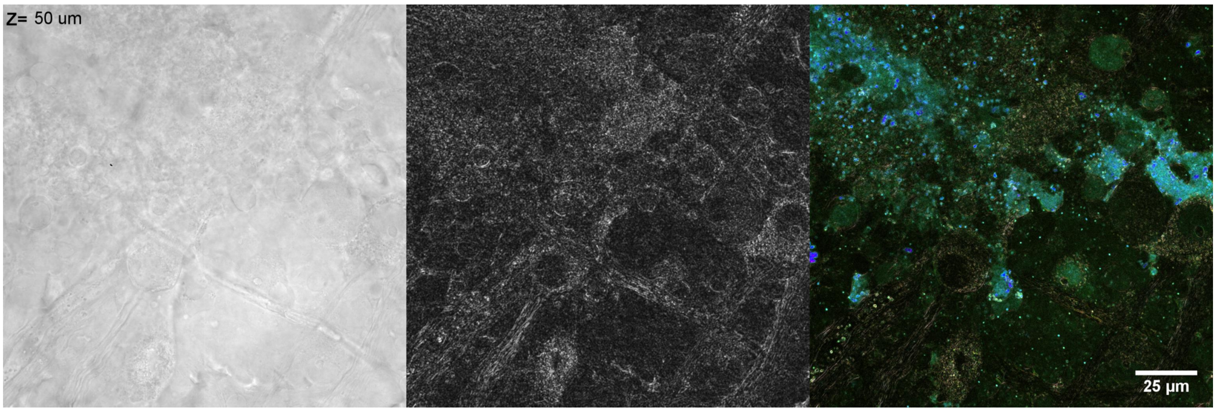

Figure 5.9: **Images of pig retina.** Comparison between the direct image, static tomographic image by shifting the piezo motor, and dynamic tomographic image of a pig retina using the intrinsic movement of the organelles in the sample, 50 μm deep in the sample.

5.4 Discussion, conclusion and perspectives

FF-OTT introduces a new optical sectioning method that exploits the effect of Gouy phase shift. The optical sectioning of about depth-of-field is achieved by combining the physical (high numerical aperture) and numerical (phase shifting) rejection of out-of-focus light. One of the main advantages of the method is the particularly simple setup. The common-path interferometer design with a single microscope objective does not require high precision mechanics and is immune to mechanical/thermal misaligning. FF-OTT can be used to get a distribution of microorganisms (e.g., algae) and to section through ex vivo samples. The method is particularly interesting for imaging ex vivo cornea samples, as it shows similar features as FF-OCT and confocal microscopy while using a much simpler device. As such, FF-OTT is promising for the diagnostics of corneal grafts.

Among the limitations of the method, we should mention the finite damping of the out-of-focus light (see the wings of the curve in fig5.4 b) compared to the strong interferometric damping in OCT. Indeed, the OCT sectioning (axial PSF) is usually linked to the Fourier transform close to the Gaussian source spectrum and quickly converges to zero. For FF-OTT, as shown in fig5.4 b, we need to use an axial modulation smaller than half the depth of field to get acceptable damping of the axial PSF wings. Compared to FF-OCT, the axial resolution in the new method is determined by the numerical aperture of the optics used and not the spectral bandwidth of the light source, which limits FF-OTT to the use of relatively high NA objectives. Another distinctive feature of FF-OTT is that it uses a common-path interferometer, eliminating the mismatch between the optical focus and the coherence plane present in FF-OCT [33]. However, the lack of an independent reference arm means that both the sample and reference signals are damped when propagating through thick, strongly absorbing, or scattering media. Part of this disadvantage is compensated because biological tissues are mostly “forward scatterers” due to the size of cells and nuclei (scattering by the structures larger than hundred nanometers is highly anisotropic in the forward direction). Lastly, in contrast to FF-OCT, the new method does not produce the optical interference fringe artifacts typically observed in cells cultures on glass or plastic slides or in regular cell mosaics, such as corneal endothelium [34]. The most peculiar feature of FF-OTT is its ability to visualize the metabolic cell dynamics without fluorescent labels. In this sense, FF-OTT can produce images similar to the dynamic backscattering-based FF-OCT [1, 14] while using a much simpler and robust optical design.

Although our simple theoretical model shows agreement with the experiment, the understanding of FF-OTT would greatly benefit from a more rigorous theoretical analysis in the future. This model should consider the high-NA optics (not completely valid for Gaussian beams) and the different numerical apertures for the transmitted and scattered waves. More precisely, the NA of the transmitted beam is determined by the LED illumination angle, while the NA of the scattered wave depends on the size of the scatterers. Finally, the scattering from the real samples is complex - even the scattering electric field from the 100 nm particles is located in a larger region than the particle itself. Therefore, the angular distribution and the geometrical parameters of the scattered electric field should be considered.

Bibliography

[1] Jules Scholler, Kassandra Groux, Olivier Goureau, José-Alain Sahel, Mathias Fink, Sacha Reichman, Claude Boccara, and Kate Grieve. Dynamic full-field optical coherence tomography: 3d live-imaging of retinal organoids. *Light: Science & Applications*, 9(1):1–9, 2020. 94, 95, 96, 102, 106

[2] José-Angel Conchello and Jeff W Lichtman. Optical sectioning microscopy. *Nature methods*, 2(12):920–931, 2005. 95

[3] Wes Wallace, Lutz H Schaefer, and Jason R Swedlow. A workingperson's guide to deconvolution in light microscopy. *Biotechniques*, 31(5):1076–1097, 2001. 95

[4] John M Girkin and Mariana Torres Carvalho. The light-sheet microscopy revolution. *Journal of Optics*, 20(5):053002, 2018. 95

[5] Jerome Mertz. Optical sectioning microscopy with planar or structured illumination. *Nature methods*, 8(10):811–819, 2011. 95

[6] Frits Zernike. How i discovered phase contrast. *Science*, 121(3141):345–349, 1955. 95, 96, 99

[7] David Huang, Eric A Swanson, Charles P Lin, Joel S Schuman, William G Stinson, Warren Chang, Michael R Hee, Thomas Flotte, Kenton Gregory, Carmen A Puliafito, et al. Optical coherence tomography. *science*, 254(5035):1178–1181, 1991. 95

[8] Emmanuel Beaurepaire, A Claude Boccara, Martial Lebec, Loïc Blanchot, and Hervé Saint-Jalmes. Full-field optical coherence microscopy. *Optics letters*, 23(4):244–246, 1998. 95, 96

[9] Marvin Minsky. Memoir on inventing the confocal scanning microscope. *Scanning*, 10(4):128–138, 1988. 95

[10] Chau-Hwang Lee and Jyhpyng Wang. Noninterferometric differential confocal microscopy with 2-nm depth resolution. *Optics communications*, 135(4-6):233–237, 1997. 95

[11] Jiubin Tan and Fusheng Wang. Theoretical analysis and property study of optical focus detection based on differential confocal microscopy. *Measurement science and technology*, 13(8):1289, 2002. 95

[12] Arnaud Dubois. *Handbook of full-field optical coherence microscopy: Technology and applications*. CRC Press, 2016. 96

[13] Olivier Thouvenin, Clement Apelian, Amir Nahas, Mathias Fink, and Claude Boccara. Full-field optical coherence tomography as a diagnosis tool: Recent progress with multimodal imaging. *Applied Sciences*, 7(3):236, 2017. 96

[14] Clement Apelian, Fabrice Harms, Olivier Thouvenin, and A Claude Boccara. Dynamic full field optical coherence tomography: subcellular metabolic contrast revealed in tissues by interferometric signals temporal analysis. *Biomedical optics express*, 7(4):1511–1524, 2016. 96, 102, 106

[15] Pedro Mecê, Jules Scholler, Kassandra Groux, and Claude Boccara. High-resolution in-vivo human retinal imaging using full-field oct with optical stabilization of axial motion. *Biomedical optics express*, 11(1):492–504, 2020. 96

[16] Viacheslav Mazlin, Peng Xiao, Jules Scholler, Kristina Irsch, Kate Grieve, Mathias Fink, and A Claude Boccara. Real-time non-contact cellular imaging and angiography of human cornea and limbus with common-path full-field/sd oct. *Nature communications*, 11(1):1–14, 2020. 96, 101

[17] Changhuei Yang and Jerome Mertz. Transmission confocal laser scanning microscopy with a virtual pinhole based on nonlinear detection. *Optics letters*, 28(4):224–226, 2003. 96

[18] Frits Zernike. Phase contrast, a new method for the microscopic observation of transparent objects. *Physica*, 9(7):686–698, 1942. 96, 99

[19] Walter Lang. *Nomarski differential interference-contrast microscopy.* Carl Zeiss Oberkochen, 1982. 96

[20] U Agero, LG Mesquita, BRA Neves, RT Gazzinelli, and ON Mesquita. Defocusing microscopy. *Microscopy research and technique*, 65(3):159–165, 2004. 96, 99

[21] Léon Georges Gouy. *Sur une propriété nouvelle des ondes lumineuses.* Gauthier-Villars, 1890. 96

[22] Jaesuk Hwang and WE Moerner. Interferometry of a single nanoparticle using the gouy phase of a focused laser beam. *Optics Communications*, 280(2):487–491, 2007. 96

[23] Martine Boccara, Yasmina Fedala, Catherine Venien Bryan, Marc Bailly-Bechet, Chris Bowler, and Albert Claude Boccara. Full-field interferometry for counting and differentiating aquatic biotic nanoparticles: from laboratory to tara oceans. *Biomedical optics express*, 7(9):3736–3746, 2016. 96

[24] Anthony E Siegman. *Lasers.* University science books, 1986. 97

[25] Simin Feng and Herbert G Winful. Physical origin of the gouy phase shift. *Optics letters*, 26(8):485–487, 2001. 97

[26] Taehwa Lee, Yeonjoon Cheong, Hyoung Won Baac, and L Jay Guo. Origin of gouy phase shift identified by laser-generated focused ultrasound. *ACS Photonics*, 7(11):3236–3245, 2020. 97

[27] Radostin Danev, Bart Buijsse, Maryam Khoshouei, Jürgen M Plitzko, and Wolfgang Baumeister. Volta potential phase plate for in-focus phase contrast transmission electron microscopy. *Proceedings of the National Academy of Sciences*, 111(44):15635–15640, 2014. 99

[28] Houda Bey, Florent Charton, Helena Cruz de Carvalho, Shun Liu, Richard G Dorrell, Chris Bowler, Claude Boccara, and Martine Boccara. Dynamic cell imaging: application to the diatom phaeodactylum tricornutum under environmental stresses. *bioRxiv*, 2021. 100, 102

[29] Arnaud Dubois, Laurent Vabre, Albert-Claude Boccara, and Emmanuel Beaurepaire. High-resolution full-field optical coherence tomography with a linnik microscope. *Applied optics*, 41(4):805–812, 2002. 100

[30] Viacheslav Mazlin, Peng Xiao, Eugénie Dalimier, Kate Grieve, Kristina Irsch, José-Alain Sahel, Mathias Fink, and A Claude Boccara. In vivo high resolution human corneal imaging using full-field optical coherence tomography. *Biomedical optics express*, 9(2):557–568, 2018. 101

[31] Jules Scholler. Motion artifact removal and signal enhancement to achieve in vivo dynamic full field oct. *Optics Express*, 27(14):19562–19572, 2019. 103

[32] Alexandra Zidovska, David A Weitz, and Timothy J Mitchison. Micron-scale coherence in interphase chromatin dynamics. *Proceedings of the National Academy of Sciences*, 110(39):15555–15560, 2013. 104

[33] S Labiau, G David, S Gigan, and AC Boccara. Defocus test and defocus correction in full-field optical coherence tomography. *Optics letters*, 34(10):1576–1578, 2009. 105

[34] Viacheslav Mazlin, Kristina Irsch, Michel Paques, Jose-Alain Sahel, Mathias Fink, and Claude A Boccara. Curved-field optical coherence tomography: large-field imaging of human corneal cells and nerves. *Optica*, 7(8):872–880, 2020. 106

General conclusion and perspectives

5.4.1 General Conclusion

In this thesis, we employed a simple Full Field interferometry microscopy working in transmission to achieve single-particle tracking and high-resolution dynamic and static Full-Field Optical Transmission Tomography on a single-cell scale. The main advantage of these methods is their high level of robustness and performance while keeping a low complexity experimental setup using an LED incoherent illumination.

We have detected, tracked, and counted different types of nanoparticles and viruses as small as 50nm. We performed these measurements using different viruses, enveloped viruses, and bacteriophages. We also have been able to distinguish between different types of particles having similar sizes using the interferometry amplitude coupled to the diffusivity properties of the nanoparticles. In addition, we distinguished between empty T5-capsids and capsids loaded with DNA. We also studied the interaction between viruses and specific antibodies or non-purified serum to monitor and follow the evolution of the reaction. Here, we went a step beyond, and we were able to estimate the affinity of antibodies in a quantitative way using a new approach based on the analysis of the modified Brownian motion and the variation of the number of particles.

We then wanted to increase the interferometric contrast and sensitivity. Thus, we investigated the perturbation of the electric field near the focus using a simple FDTD simulation. We aimed to study the influence of the radiation pattern depending on the size of the particles. We also employed a simple analytical model to understand the impact of the Gouy phase shift, the defocus, and the tilted illumination. These simulations are used to qualitatively understand the interferometric signal. We realized that the size of the interferometric spots is not limited by the numerical aperture of the system (for high numerical aperture>1).

In order to optimize the signal-to-noise ratio, we have developed a wide field speckle-free illumination using a high-power laser to increase the interferometric signal. Here, we employed a high frequency (MHz) deformable mirror coupled to a square core optical fiber to achieve such illumination and to have sufficient intensity to attenuate the reference in the back focal plane of the objective lens while saturating the camera. As a result, we have been able to track small viruses (MS2, AAV) of (27, 20) nm in diameters when increasing the interferometric contrast by a factor of more than 10.

Finally, we introduced a new tomography approach to perform optical sectioning insolid or semi-solid structures by shifting the position of the focal plane of the objective lens. We applied this approach to environmental and ex-vivo corneal samples. We used a piezoelectric motor to acquire two consecutive images. We also performed tomographic images by relying on the intrinsic movement of the biological samples. Here we imaged the internal metabolic of Hela cells when adding Deoxy-glycose, in which a high metabolic activity is detected in the nucleus of cells, and a decrease of the metabolic activity is detected in the cytoplasm. This behavior is already described during apoptosis.

5.4.2 Perspectives

We investigated the hardware and software to perform single-particle tracking and achieve high-resolution dynamic and static FFOTT acquisitions while keeping a significantly low complexity experimental setup. In addition, we have demonstrated the ability to increase the interferometric by attenuating the low numerical aperture beam corresponding to the reference illumination using a simple dot attenuator. Therefore, we can reach very high interferometric sensitivity for an almost unlimited incident light power.

Differentiation of small viruses and nanoparticles

Like placing a dot attenuator in the back focal plane, an annular phase mask can be positioned in the pupil plane to extend the depth of field of the optical system [1]. Monitoring nanoparticles in a more considerable detection volume can be advantageous since it allows tracking particles for a longer time interval, and it can also be convenient for smaller concentrations of nanoparticles. We have shown in this work the ability of our approach to distinguish between different nanoparticles of similar size. An interesting addition would be to use microfluidics to physically separate between different populations of particles, such as empty and full viral particles. Therefore, real-time detection and tracking approaches are needed for such an application. We have explored an algorithm developed for object detection (YOLOv4) combined with a tracking algorithm (Deep sort) based on deep learning approaches. As preliminary results, we had a decent detection and tracking speed using the google collab GPU cloud without a high-performance computer (presented in appendix B). Furthermore, using the modification of the Brownian motion, we can study the structure of the outer surface of biotic nanoparticles and detect viruses or antibodies in biological samples.

Monitor internal metabolism of the cell and single particles in biological structures

An interesting approach is to combine the FFOTT to interferometric detection of single particles in a solution. Such an approach can be convenient for monitoring the effect of nanoparticles on biological structures, such as nanoparticles used for drug delivery, gene therapy (monitoring the infectivity of viruses), or quantification of the vesicles and other biotic nanoparticles. Here, by processing the images in 2 different steps. First, we can monitor the metabolic activity for slow dynamics. The second step consists of using a high acquisition rate to perform SPT. Therefore, by simply processing the data on different time scales, one can simultaneously perform dynamic FFOTT to image ex-vivo biological structures and track biotic nanoparticles.

FFOTT for eye diagnostics using retro illumination of the cornea

Furthermore, we have tried to apply the FFOTT approach to perform optical sectioning to image in-vivo samples. Thanks to its high performance and simplicity, we obtained some promising results in our first tests, relying on using the concept of retro illumination of the cornea (red eyes effect). So far, we have relied on the natural movements of the eye to perform tomographic images. Yet a considerable margin of improvements can be done by achieving high-speed modulation of the plane of focus. Such low complexity and high performance are required for a clinical device used for eye diagnostics.

Appendix A

simultaneous fluorescence and interferometric SPT

Characterization and Discrimination of viruses and vesicles by bimodal simultaneous detection: scattering and fluorescence

HOUDA BEY[1*], SAMER ALHADDAD[1], MARTINE BOCCARA[1,2*], ROMAIN SAUSSET[3], MARIANNE DE PAEPE[3], OLIVIER THOUVENIN[1], CLAUDE BOCCARA[1*], IGNACIO IZEDDIN[1*]

[1] Institut Langevin, ESPCI Paris, CNRS, PSL University. 1 rue Jussieu, 75005 Paris
[2] Atelier de Bioinformatique, UMR 7205 ISYEB Sorbonne Universités, Univ Paris 06, CNRS, MNHN, EPHE, 45 rue Buffon, 75005 Paris, France
[3] Université Paris-Saclay, INRAE, AgroParisTech, Micalis Institute, 78350 Jouy-en-Josas, France

Abstract: In order to optimize discrimination and characterization of complex mixtures of nanoparticles, we develop, a new optical imaging microscope that combines the advantages of transmission interferometry and fluorescence. This work presents results for a rapid and reliable detection of viruses and membrane vesicles in aqueous medium. This system by detecting scattered light as well as fluorescence allowed to track single particles and to analyze their Brownian motion as well as their scattering level. We present the specificity of this approach to detect individual particles in range from 40 nm up to 200 nm using simultaneously the two detections. We demonstrated that, within a few second recording, we count and quantify the size distribution of all nanoparticles present in complex samples and discriminate particles of different refractive index such as virus and membrane vesicles.

1. Introduction

The detection, concentration quantification and size determination of viruses is a main challenge for aquatic environments and biomedicine developers [1-3]. Among nanoparticles, phages are bacterial viruses with sizes between 20 and 200 nm and are considered to be the most abundant biological entities on earth [4].The abundance of phages in aquatic ecosystems and their effect on bacterial host explains the present bloom of phage studies [4,5]. Membrane vesicles have been isolated in many different environments [6] and they may play an important role in the interaction bacteria-phages [7]. In addition to classical microbiology andmolecular biology techniques [8], the determination of viruses characteristics in the submicron range has been performed with a wide range of physical methods, including transmission electron microscopy [9], flow cytometry [10] atomic force microscopy (AFM) [11], light scattering techniques [12], Single Particle Zeta Potential [13] or nanoparticle tracking analysis (NTA) [14]. NTA allows real-time detection and counting of viral particles in minutes, based on dynamic light scattering by laser-illuminated optical microscopy [15]. All the methods presented above have their applications when considering homogenous suspensions of viruses or vesicles. In addition to these technics, the most popular method for viral quantification is to label the genetic material of viruses and visualize them under an epifluorescence microscope [16]. However, most of these different methods are not used to quantify uncharacterized, complex samples such as soil or feces.

In the past few years, interferometric techniques have gained much interest for the analysis of individual metal particles, polymer nanoparticles or viruses, as they offer high-sensitivity detection of unlabeled nanosized objects [17]. We developed a new microscope to use a combination of light scattering and interferometry to analy**z**e complex mixtures of nanoparticles of different refractive index [18]. With this set up we have been able to differentiate viruses from membrane vesicles in TARA ocean samples. However preliminary analyses revealed that the great quantity of membrane vesicles in intestinal samples challenges the discriminative capacity of using only the scattering information.

Inspired by this challenge, we developed a new high-resolution imaging device that allows to get a bimodal simultaneous detection of scattering and fluorescent signals. The device uses a spatially incoherent source to illuminate the field of view, associated to a stable common path interferometer where the scattered beam interferes with the illuminating beam that irradiates the nanoparticle, we added a fluorescent channel to track virus particles labelled with a nucleic acid fluorophore (SYBR Gold that yielded bright and stable fluorescent signals detected by a cooled CMOS camera). In this work we first validate our multimodal microscopy system that combines the advantages of both, common-path interferometry and fluorescence microscopy, using calibrated fluorescent beads. We then compared quantification and size determination of viruses. Finally we showed that we can discriminate viruses from membrane vesicles in mixtures of different compositions.

2. Materials and Methods

2.1 Beads and viruses

FluoSpheres carboxylate-modified polystyrene beads of various size (40nm, 100nm, 200nm), are fluorescent beads in the yellow-green spectral wavelength (Excitation: 505 nm/Emission: 515 nm). The stock concentrations are given by manufacturer (Thermo fisher ref: F8888) are shown in **Table 1**. The beads were diluted in phosphate-buffered saline (PBS) (Sigma-Aldrich) and sonicated for 15 minutes prior to use.

The DNA of Bacteriophages (SPP1, T4 and T7) was labelled with SYBR Gold (Thermo Fisher Scientific -ref: S11494, 1000x).

Concentration of infectious particles from purified phages were determined by plaque assay (PFU plaque forming units or infectious particles): SPP1 ($4.4x10^9$ PFU mL^{-1}), T4 ($2.4x10^8$ PFU mL^{-1}) and T7 ($7.6x10^8$ PFU mL^{-1}). The Purified bacterial vesicles concentration has been determined with the interferometry microscopy set up. Samples of viruses were diluted in TE buffer (10 mM Tris-HCl and 1 mM EDTA, pH 7). Virus and vesicles aqueous suspensions was prepared at different ratios $r = [\text{Virus}] / [\text{Vesicles}]$ (Vi:Ve) where r= 50:50 and 10:90. The mixture was then stained with Sybr Gold. We used a stock dilution for Sybr Gold (1:1000000). For observations, we mixed 5µl of Sybr Gold Stock dilution) with 5µl of the different dilutions of the viruses.

2.2 Multimodal System Setup

The system for multimodal imaging is schematically presented in **Fig.1**. For this study, the camera for Fluorescence signal and the camera for scattering signal were optically co-aligned and electronically synchronized so that multimodal images were collected simultaneously. Videos were recorded with a custom written Matlab program. The light source used is a LED with a central wavelength of 470nm (M470L4, Thorlabs, Newton, NJ, USA). The choice of the light source for a multimodal system is one of the most important parameters. First, it must be spatially incoherent to avoid speckle artefacts; moreover the optical power must be high enough to obtain an image close to the saturation level of the camera in order to maximize the signal-to-noise ratio in our shot noise limited detection. The scattering signal was recorded with a CMOS camera (Photonfocus). The field of view recorded by the camera is ~ 97µm x 97 µm. This setup for scattering was combined with a fluorescence channel using the same LED source for excitation. In order to avoid the superposition of the excitation light and the fluorescence light we filter the light through an excitation filter with a band pass filter centered on 475 nm and with a bandwidth of 50 nm (Semrock FF02-475 / 50-25), then the light is directed to the sample and after this, light reaches an oil immersion objective. The fluorescence light is reflected by a dichroic mirror (DM: 506nm/25) to collect the fluorescence signals while the scattering signal is detected in transmission common path interferometry (IT). The fluorescence emitted was filtered with another bandpass filter centered at 540 nm (Semrock FF01-540 / 50-25), then imaged using a CMOS camera (ORCA-Hamamatsu), for a field of view of ~ 97µm x 97 µm. The samples are imaged by the same infinite conjugate microscope objective (OLYMPUS 100X NA=1.25) followed by two different tubes lenses which allow the object to be focused on both cameras with the same pixel sizes. For our experiments, the sample drop (volume of approximately 8µ) is placed on a glass coverslip (100µm thick and 30mm diameter). The tube lens (TL1-Ø 200 mm) is placed in front of the camera of the scattering channel, and the tube lens (TL2-Ø125 mm) is placed in front of the fluorescence camera. We used two different tube lenses which allows to get at the end about the same pixel size in the two fluorescence and scattering channels, because the pixel sensor size of the CMOS camera is 10.6µm while the fluorescent camera (ORCA-Hamamatsu) pixel sensor size is 6.5µm. Each image recorded by the camera is a superposition of static elements (e.g. cleaning residues on the walls of the coverslip) and dynamic images of particles animated by the Brownian motion. In order to get rid of the static part of the image which would obscure the observation of nanoparticles, we average the signals from the 200 images recorded on the IF camera; the dynamic part is not likely to be detected in this averaged image because of the larger background signals. We then subtract the static background of each image. Thanks to this averaging process, no additional noise is introduced into the sequence of images.

2.3 Particle tracking analysis

For single particle tracking analysis, we used MTT (Multiple Target Tracking)[20] software. This software that is usually used to locate fluorescent particles in each image, was adapted to detect nanoparticles by light scattering. In an optical microscope, a point-like particle forms a diffraction-limited image of width approximately equal to λ/(2NA), where λ is the wavelength of the light and NA is the numerical aperture of the objective. The spots positions can be determined with high accuracy using MTT software that identifies the center of the local distribution [20]. Its principle is to find intensity peaks clearly higher than the background noise, when the maximum signal is found, the detected spots are matched by a Gaussian function adapted to the diffraction spot size. Locating and reconstructing particles tracks consists of several processes: the positions of a scattering particle are reconnected to construct a trajectory of nanoparticles; in addition to providing nanoscale resolution, single particle tracking (SPT) has the ability to discriminate between the different modes of movement of the particles being tracked. In most cases, tracking involves a two-step process: first, objects are segmented independently in each frame, and second, detected objects are linked frame by frame to define the object track. The trajectories were then used to calculate a diffusion coefficient for each track using the equation with the 2 dimensions:

$$D = \frac{\sqrt{\left\langle (\Delta x)^2 \right\rangle}}{4\Delta t \varepsilon} (1)$$

Where: D is the diffusion coefficient. $< (\Delta x)^2 >$: is the mean square displacement. Δt is the time between two successive positions of the particles, ε is a correction factor to account for a non-zero exposure time. The Stokes diameter (Diam) (size of particle) was then calculated using:

$$Diam = \frac{k_B T}{3\pi D\eta} (2)$$

Where T is the temperature (in Kelvin), k_B is Boltzmann constant D is the mean diffusion coefficient and η is the viscosity of the solution.

3. Results

3.1 Simultaneous detection

We developed a multimodal system combining scattering with a very simple and stable fluorescence imaging system that can address several critical biology concerns (**Fig.1a**). The scattering system relies on the scattering cross-section (that is a function of the refractive index of the scattering particle). In principle, Interferometric Microscopy works by amplifying the weak scattered light by viruses via interference with the reference wave that is used to illuminate the particle (common path interferometry). The intensity detected I_d (Equation 3) in scattering is described by:

$$I_d = \left| E_r + E_s \right|^2 = I_r + I_s + 2\sqrt{I_r I_s} \cos\Phi (3)$$

Where, I_r is the reference intensity, I_s is the scattered intensity, Φ designates a phase shift between the reference and the scattered beams (mainly determined by the Gouy phase shift here [21]).

We used two different cameras for the 2 detection channels. Indeed shot noise limited interferometry requires a camera with a high full well capacity that usually exhibit a large dark noise level) whereas fluorescence detection requires a low dark level. By recording a time series of images (200 frames), we simultaneously detect the same particles using the scattering camera and the fluorescence camera for beads size 100nm (see **Fig.1b** and the video in supplementary visualization 1) for beads 200nm and 100nm. However, we did not observe fully identical trajectories in the two channels as the signal-to-noise ration is larger in fluorescence than in interferometry and longer trajectories could be recorded.

We measured the number of fluorescent particle using different dilutions according to the initial concentration given by the manufacturer. We observed a good correlation between the number of counted particles and the results expected from dilutions. Concentration values are linear over a wide range of sample dilutions and show excellent agreements with calculated concentration values given by the manufacturer. However we observed two different alignments one for large nanoparticles 100nm and 200nm and one for the smaller particles (40nm in diameter) (**Fig.2**). Particle number estimate can be written as a straight line: Number of all tracked particles= K x Theoretical concentration after dilutions (number of particles/mL), K is the linear slope. To estimate the concentration, multiply the number of all particles tracked by the linear slope (K). For nanoparticles of 100nm or more, an average linear slope equal to $4x10^{-7}$ is used and for the smallest particles of 40nm a linear slope equal to $6x10^{-8}$.

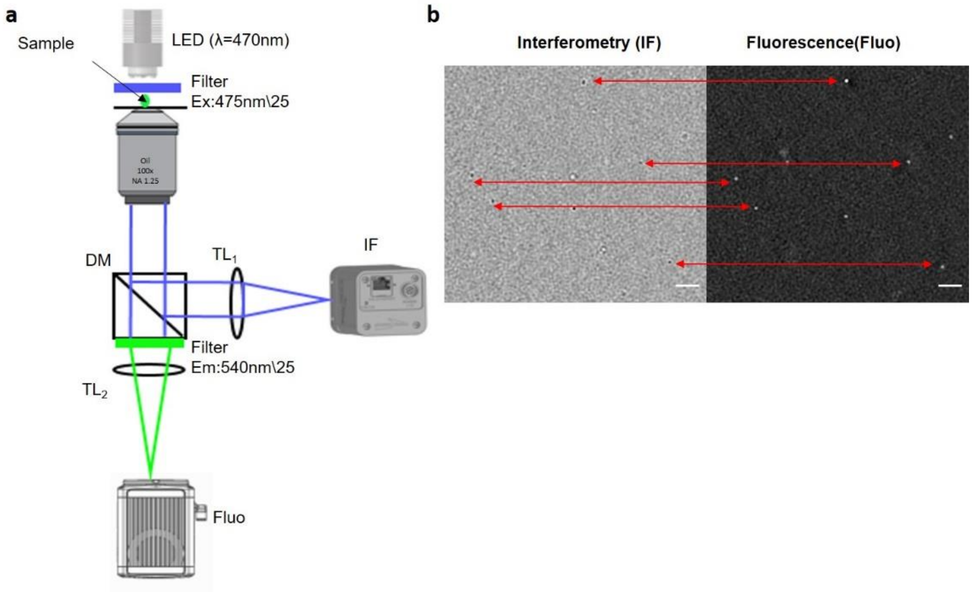

Fig.1: Experimental set-up and signal processing: a) Principle of the Multimodal system combining interferometry Microscopy and Fluorescence Microscopy. An incoherent source 470 nm illuminates the sample under study that both scatters light and fluoresces. This LED emits light over a broad spectrum that partially overlaps the fluorescence spectrum. We therefore filter the light through an excitation filter (Ex: 475nm/25), then the light is directed to the sample through an oil immersion objective. This light is reflected in a dichroic mirror (DM: 506nm/25) to collect the

fluorescence signals while the scattering signal is detected in transmission by interferometry (IT). The fluorescence of a green-shifted wavelength is re-filtered by an emission filter (Em: 540nm/25). By recording a time series of images (200 frames) we simultaneously follow the particle movements using the IF (interferometry) camera and fluorescence camera. b) Nanoparticles of size 100nm detected by scattering camera and fluorescence camera at the same time. Scale bars are 5µm

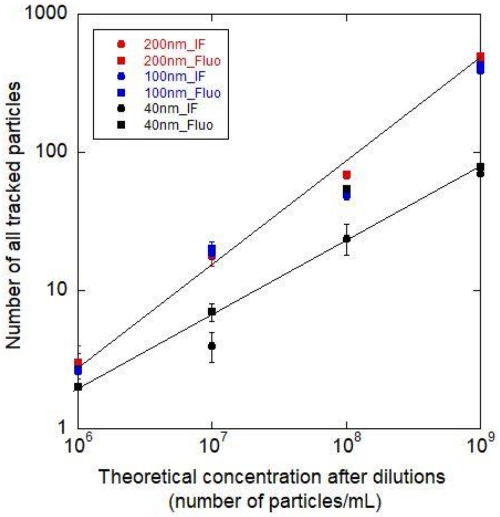

Fig.2: Computed number of particle for different concentration and different sizes.

Gaussian mixtures play an important role in the multimodal distribution of one-dimensional data. The fitting of Gaussian mixture models [22] allows to obtain different separate modes, the proportion of the nanoparticle size estimation and the proportion of nanoparticles aggregation (**Fig.3**). We fitted the amplitude data using the Gaussian Mixture Modeling distributions.

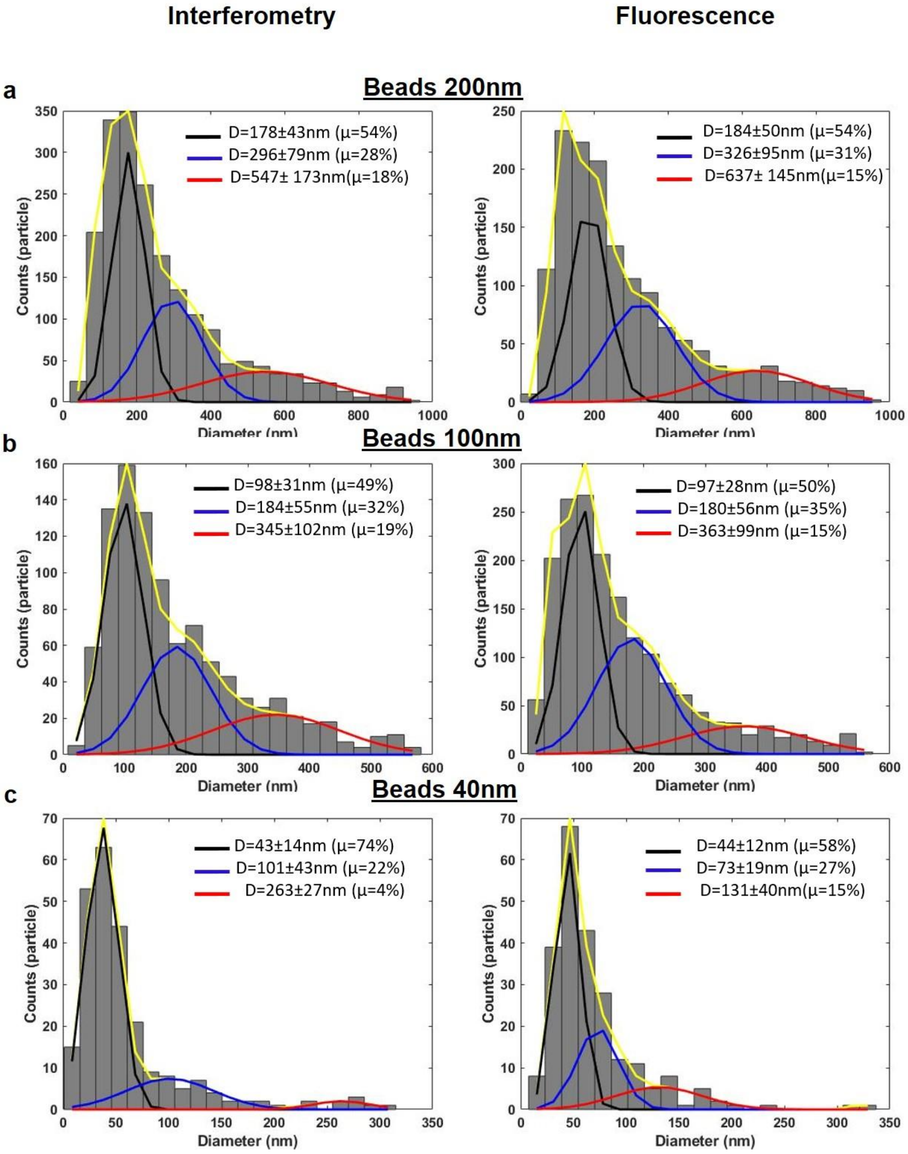

Fig.3: Comparison of diameter determination by Brownian motion analysis between Interferometry (IF) and Fluorescence (Fluo). We fitted the amplitude data using the Gaussian Mixture Modeling (GMM) distributions [22]. The bins of the histogram are divided into three colors, where the black part shows the proportion of the nanoparticle size estimation, the blue and red part shows the proportion of aggregates, which depends on the combined location errors of the two or three point spread function (PSF). The yellow curve shows the estimated total distribution, which is the sum of the black, Blue, and Red Gaussians. a) Distribution of estimated diameter for nanoparticles 200nm (930 particles in IF and 953particles in Fluo). b) Distribution of estimated diameter for nanoparticles 100nm (636 particles in IF and 674 particles in Fluo). c) Distribution of estimated diameter for nanoparticles 40nm (142 particles in IF and 170 particles in Fluo).

The mean diameters ± standard deviations (**Fig 3**) of the 40, 100 and 200nm fluoSpheres carboxylate-modified polystyrene (NPs) were determined with our multimodal system. The distribution of sizes values in scattering (IF) and fluorescence channel (Fluo) observed with our set up was found in agreement with the sizes given by the manufacturer (Thermo fisher). These results confirms the size determination of the fluoSpheres (NPs) using electron and confocal microscopy [23]. These observations validated our multimodal system for detecting and characterizing nanometer particles and encouraged us to analyze suspensions of known viruses and vesicles, and investigate the detection of particles of different refractive index in mixtures.

Table 1: Analysis of the sizes and concentration of fluorescent microspheres (latex particles) in the two channels (IF: Interferometry, Fluo: Fluorescence)

		IF		**Fluo**	
Beads	**Theoretical concentration after dilution (P^{a}/ml)**	**Conc (P x10^{9} x ml^{-1})**	**Diameter (nm)**	**Conc (P x10^{9} x ml^{-1})**	**Diameter (nm)**
200nm	**1x10^{9}**	**1.1±6**	**178 ±43**	**1.3±3**	**184 ±50**
100nm	**1x10^{9}**	**0.97±5**	**98 ±31**	**1.1 ±4**	**97 ±28**
40nm	**1x10^{9}**	**1.1±8**	**43 ±14**	**1.2±10**	**44 ±12**

[a] P: nanoparticles

3.2 *Characterization of known viruses and discrimination of particles of different refractive index in mixtures*

We first used purified viruses, of different morphology such as T4 phage, (rigid tail), SPP1 phage (flexible tail), T7 phage (small tail)[24]. Viruses were labelled with Syber Gold.

We first measured the phage T4 concentration in scattering channel and fluorescence channel, we then measured the phage T7 concentration in both cases we used calibration curve described in figure 2). With our setup, we are looking at infectious and not infectious physical particles and we detect more particles than with the titration method (PFU)

phages	**PFU mL^{-1}**	**diameter IF**	**Nb tracks**	**Concentration IF**	**diameter` fluo**	**Nb tracks**	**Concentration fluo**
T4	2.4x10^{8}	105±8nm	130	6**x10**^{8}±11	100±8 nm	150	7**x10**^{18}±8
T7	7.6x10^{8}	59±20nm	110	3.2**x10**^{9}±11	62±17 nm	120	3.5**x10**^{9}±10
SPP1	4.4x10^{9}	61±19	123±13		58±18	140±11	

The values of the phage diameter estimation (T4 and T7 and SPP1) are consistent with the sizes of the viruses determined by electron microscopy [24].

We then wanted to show the reliability of the multimodal system for the discrimination between particles of different refractive index such as viruses and membrane vesicles in a mixture. In this work, we used bacteriophages SPP1 with purified membranes vesicles. We first analyzed the SPP1 viruses and vesicles alone (See the distributions in supplementary 3 and **table2**). Then we carried out two ratios of viruses (Vi) and vesicles (Ve) (Vi=50: Ve=50) (See the distributions in supplementary 4) and (Vi=10: Ve=90). **Table 2** and **Fig.4** show that the distribution of populations and demonstrate that we can discriminate between SPP1 and membranes vesicles when using a 50:50 ratio as well as a 10:90 ratio. We observed by florescence that 89% the particles corresponded to single viral particles and 11% to viral aggregates. By Interferometric microscopy we observed 11% SPP1 (single particles) and 54% vesicles (single particles) and 35% of aggregates of which 1 or 2% are from viral origin (total viruses 12-13%) and about 85% of vesicles (single particles+ aggregates).

Table2: Characterization and discrimination of morphological properties of known viruses and complex mixtures

Material	Dimensions (nm)	Estimated of the percentage of particles		Number of tracked particles in the considered volume		Diameter (nm)	
		IF	Fluo	IF	Fluo	IF	Fluo
SPP1 (Vi)	Head: 60	ND	ND	123±13	140±11	61±19	58±18
Membrane Vesicles (Ve)		ND	ND	98±12	0	89±30	
SPP1:Vesicles Ratio (50:50)		100	50	Vi=42±4 Ve=40±1	Vi=38±3		
SPP1:Vesicles Ratio(10:90)		100	10	Vi=12±3 Ve=93±2	Vi=14±2		

* SPP1conc=4,4x10^{9} infectious PFU mL^{-1}

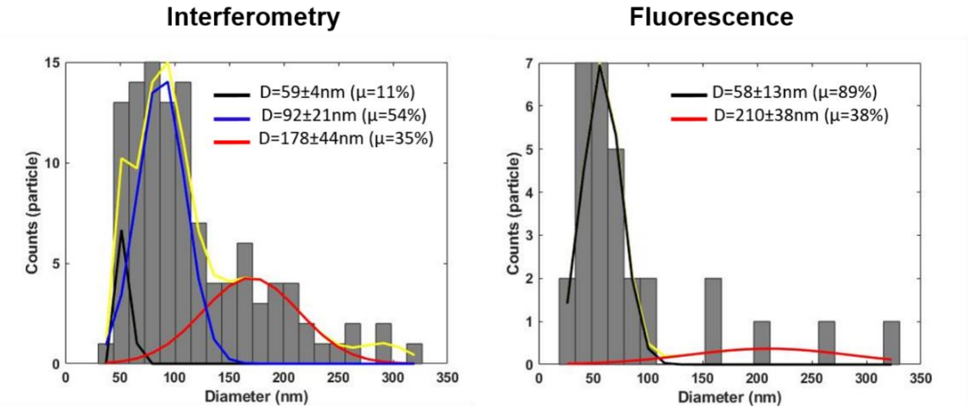

Fig.4: Discrimination viruses-membranes vesicles. The viruses in labelled with Sybr Gold. Each sample was evaluated using the multimodal system described in fig1 using fluorescent detection and light scatter modes. Percentages of particle tracking who experienced discrimination are presented in histogram of particle sizes viruses-membranes vesicles (ratio 10:90). Peak Gaussian fitting curve (black line) of SPP1, blue line of membranes vesicles, and red line the vesicles-viruses aggregation

4. Discussions and Conclusions

Here we describe a new multimodal imaging system combining the informations extractef from of light scattering and from fluorescence microscopy in order to detect and count viruses and to discriminate particles of different refractive index (here virus and membrane vesicles) quickly and easily. Our set up have a small cuvette to analyze very small sample volumes (we have successfully tested 8µL) and we were able to count nanoparticles in the 40-200 nm diameter ranges. Our experimental study examined the size of phage with various sizes and morphologies (T4, T7, and SPP1). In addition, we show that we can count membrane vesicles with our methodology and discriminate between viruses and vesicles household. The method described here can thus be applied to analyze samples from a variety of environments such as the soil or the intestines. Our methodology for functionalizing viral particles has several advantages over existing virus detection techniques. Our analysis provides a simple and rapid method to quantify and discriminate whole viral particles, which is particularly important in vaccine production or detection of Inflammatory bowel disease. Our method is also a quick way to assess viral aggregation, and our results suggest that viruses in the gut tend to aggregate independently in solution [25].

Funding. This research was supported by financial support from ANR PRIMAVERA. Samer Alhaddad is beneficiated of a PhD grant funding from PSL University. Romain Sausset is beneficiated of a PhD grant funding from MYRIADE Company. HB got a postdoctoral fellowship from the Dim elicit Influare in viscerae

Acknowledgments.

We warmly thank Paulo Tavares from Institute for Integrative Biology of the Cell for the SPP1 phage that we used in this study. Also, we thank Dr Viviane Ravet from Université de Clermont Ferrand for purified bacterial vesicles that we used in this study.

Supplemental document. See Visualization 1, the distributions in supplementary 1, the distributions in supplementary 2 and the distributions in supplementary3 for supporting content.

Supplementary 1: Histogram of Maximum and mean Intensity for polystyrene beads of various size (40nm, 100nm, 200nm).

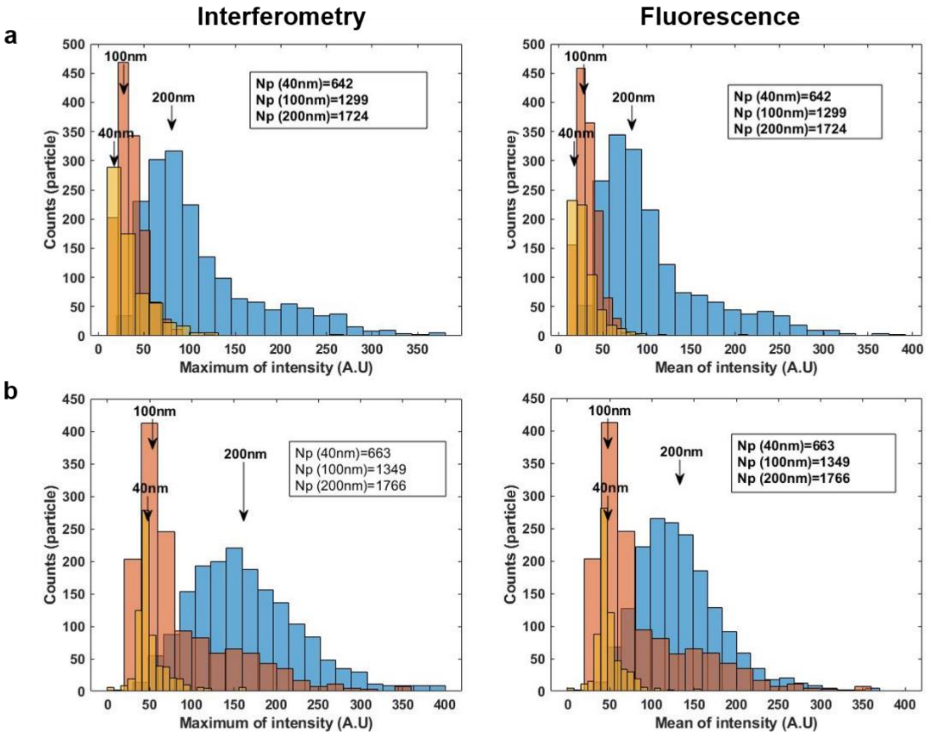

Supplementary 2: Histogram of diameter estimated SPP1 and membrane vesicles.

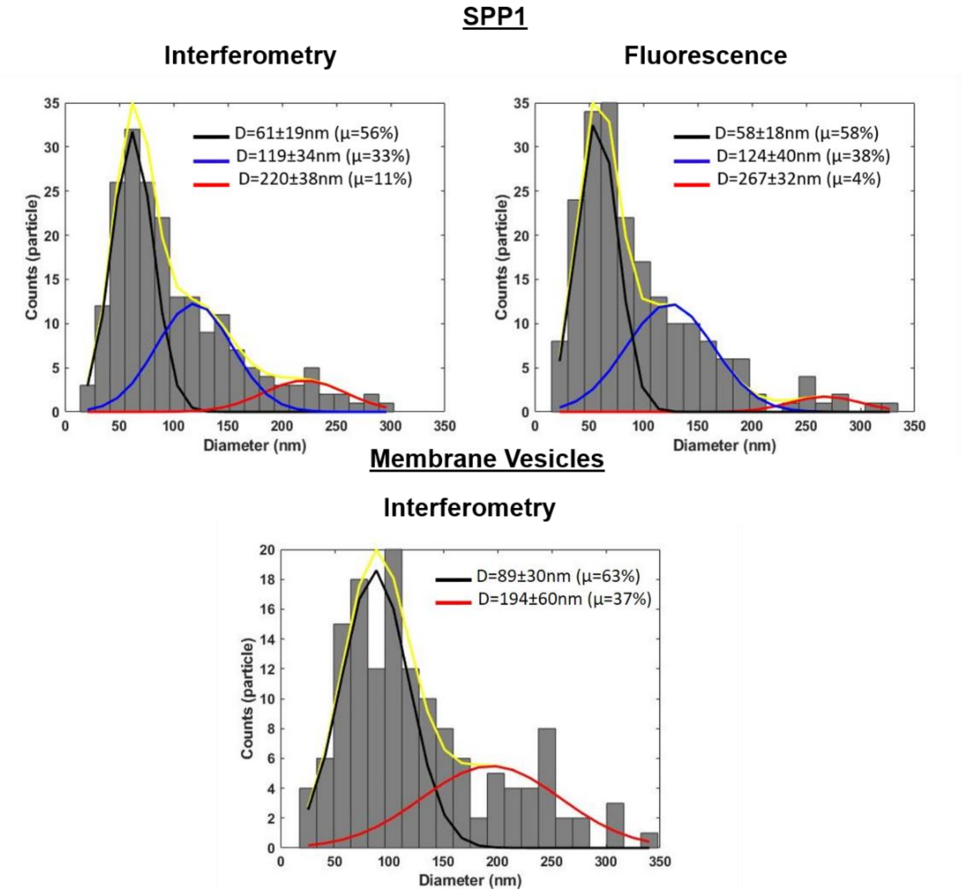

Supplementary 3: Histogram of particle sizes viruses-membranes vesicles (ratio 50:50).

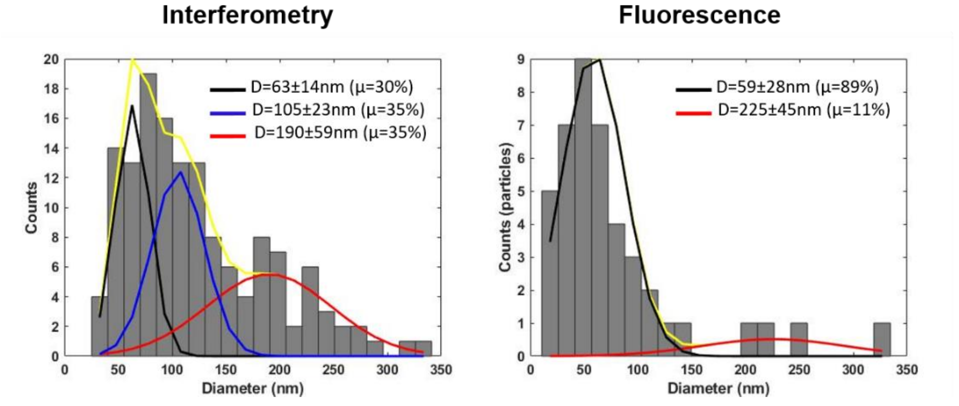

References

1. G.G.N. Thushari, J.D.M. Senevirathna, Plastic pollution in the marine environment,Heliyon, 6(8),2405-8440(2020).
2. Garcia-Romero, N., et al., Extracellular vesicles compartment in liquid biopsies: Clinical application. Mol Aspects Med, 2018. 60: p. 27-37 DOI: 10.1016/j.mam.2017.11.009.
3. Metzner, C.; Zaruba, M. On the Relationship of Viral Particles and Extracellular Vesicles: Implications for Viral Vector Technology. Viruses 2021, 13, 1238. https://doi.org/10.3390/v13071238
4. C.A.Suttle, "Marine viruses-major players in the global ecosystem," Nat. Rev. Microbiol (5), 801–812 (2007).
5. Télesphore Sime-Ngando, T.(2014) Environmental bacteriophages: viruses of microbes in aquatic ecosystems. Front Microbiol 5:355.
6. Soler, N., Krupovic, M., Marguet, E. et al. Membrane vesicles in natural environments: a major challenge in viral ecology. ISME J 9, 793–796 (2015).
7. Tzipilevich, E., Michal Habusha, M.,and Ben-Yehuda, S. (2017) Acquisition of Phage Sensitivity by Bacteria through Exchange of Phage Receptors. Cell, 168: 186-199.
8. Kaletta J, Pickl C, Griebler C, Klingl A, Kurmayer R, Deng L. (2020) A rigorous assessment and comparison of enumeration methods for environmental viruses. Sci Rep. 10(1):18625.
9. Brum, J., Schenck, R. & Sullivan, M. Global morphological analysis of marine viruses shows minimal regional variation and dominance of non-tailed viruses. ISME J 7, 1738–1751 (2013).
10. Brussaard, C. P. D. Optimization of procedures for counting viruses by flow cytometry. Appl. Environ. Microbiol. 70, 1506–1513 (2004).
11. JL.Huff, MP. Lynch, S.Nettikadan, JC.Johnson, S. Vengasandra, E.Henderson, "Label-free protein and pathogen detection using the atomic force microscope," J Biomol Screen **9**(6), 491–7(2004).
12. I.Makra, P.Terejánszky, RE. Gyurcsányi, "A method based on light scattering to estimate the concentration of virus particles without the need for virus particle standards," MethodsX 2, 91–9(2015).
13. R.Vogel,A.K. Pal, S.Jambhrunkar, et al," High-Resolution Single Particle Zeta Potential Characterisation of Biological Nanoparticles using Tunable Resistive Pulse Sensing," Sci Rep 7, 17479 (2017).
14. Filipe, V., Hawe, A. & Jiskoot, W. Critical evaluation of nanoparticle tracking analysis (NTA) by NanoSight for the measurementof nanoparticles and protein aggregates. Pharm. Res. 27, 796–810 (2010).
15. Anderson, B. et al. Enumeration of bacteriophage particles: comparative analysis of the traditional plaque assay and real-time QPCR- and nanosight-based assays. Bacteriophage 1, 86–93 (2011).
16. Suttle, C. A. & Fuhrman, J. A. (2010).Enumeration of virus particles in aquatic or sediment samples by epifluorescence microscopy. Man. Aquat Viral Ecol. 15, 145–153
17. M. Boccara, Y.Fedala, C.Venien-Bryan, M. Bailly-Bechet, C.Bowler, A.C Boccara, "Full-field interferomet ry for counting and differentiating aquatic biotic nanoparticles: from laboratory to Tara Oceans,"Biomed Opt Express, **7**(9), 3736–46(2016).
18. Yurt, A., Daaboul, G. G., Connor, J. H., Goldberg, B. B., & Ünlü, M. S. (2012). Single nanoparticle detectors for biological applications. Nanoscale, 4(3), 715-726
19. Pauline J Kolbeck, Willem Vanderlinden, Gerd Gemmecker, Christian Gebhardt, Martin Lehmann, Aidin Lak, Thomas Nicolaus, Thorben Cordes, Jan Lipfert, Molecular structure, DNA binding mode, photophysical properties and recommendations for use of SYBR Gold, Nucleic Acids Research, Volume 49, Issue 9, 21 May 2021, Pages 5143–5158, https://doi.org/10.1093/nar/gkab265
20. Sergé, A., Bertaux, N., Rigneault, H. et al. Dynamic multiple-target tracing to probe spatiotemporal cartography of cell membranes. Nat Methods 5, 687–694 (2008).
21. S.Feng, H. G. Winful, "Physical origin of the Gouy phase shift," Optics Letters, 26, 485(2001)
22. Lerch, F., Ultsch, A. & Lötsch, J. Distribution Optimization: An evolutionary algorithm to separate Gaussian mixtures. Sci Rep 10, 648 (2020).
23. Mutzke E, Chomyshyn E, Nguyen KC, Blahoianu M, Tayabali AF. Phagocytosis-coupled flow cytometry for detection and size discrimination of anionic polystyrene particles. Anal Biochem. 2015 Aug 15;483:40-6.
24. Owens, Flores, Di Serio F, Li S, Pallás V, Randles J, Sano V (2012) Virus taxonomy: Ninth Report of the International Committee on Taxonomy of Viruses. In. pp 1221–1234
25. Prudent, V., Demarre, G., Vazeille, E. *et al.* La souche bactérienne liée à la maladie de Crohn LF82 assemble des communautés de type biofilm pour se protéger des attaques phagolysosomales. *Commun Biol* **4,** 627 (2021). https://doi.org/10.1038/s42003-021-02161-

Appendix B

Machine learning for single particle detection and tracking

Deep learning for Single-particle detection, localization, and tracking:

In this appendix, we have implemented a deep learning approach to perform single particle detection localization and tracking at a fast frame rate in order to achieve real-time single-particle tracking. This concept relies on **GPU usage** to accelerate the training, detection, and tracking process. We present a brief walk-through of the different steps of the development of the **Single Particle Tracking process**. We first describe the **training process** needed to optimize the network weights, here we show an example of the training of single particles. In the next step, we employ the optimized weight to run the You Only Look Once, **YOLOv4** detection approach developed initially by[Yolov4: Optimal speed and accuracy of object detection]. **For real-time detection**, we have used **Deep sort**, which is a framework that allows the tracking of the position of the detected object in real time. To accelerate the process we benefited from the limited GPU facilities provided by **google COLAB**.

The use of YOLOv4

YOLO algorithm has initially been developed for the detection of different objects that can be encountered in our everyday life, such as people, cats, bikes, cars, etc… It has been released in 2016 and the algorithm has improved significantly in terms of accuracy and speed in terms of frame rate. The first implementation of this algorithm has been performed thanks to the coco training set, which consists of 80 different classes of objects presented in labeled images[Microsoft coco: Common objects in context]. The usual images consist of everyday images with an associated text file indicating the exact position of each object in terms of pixels as well as the class of each object in every image.

The training process:

One main advantage of the YOLO algorithm is mainly because of its adaptability. Instead of the use of the usual pre-trained weights used usually for the detection of 80 everyday life classes, YOLO can be trained for the detection of any desired objects by simply modifying the training set used to train the network.

For the detection of single particles, we are interested in the detection of **PSF spots**. **The shape and the intensity of the PSF**, depend mainly on the axial position of the particles in the field of view, because of the Gouy phase shift and defocus. Therefore, we can see dark and bright PSF spots varying in terms of size of the spot. In order to localize the PSF spots, we perform standard PSF sub-pixel localization by fitting the interferometric PSF spots **using 2D Gaussian fit** in order to retrieve the central position of each particle and estimated the width of the spot. By doing so, we construct our labeled training sets consisting of the images as well as a text file indicating the position of the objects of interest in each image. Then we use these images to **train the network**, here we would like to note that to train the YOLO algorithm, we need both the images as well as their labels: x, y position, width, height, and the class of the objects in each image). **Fig1** Show an example image of interferometric PSF spots and their respective labels in a text file for each image.

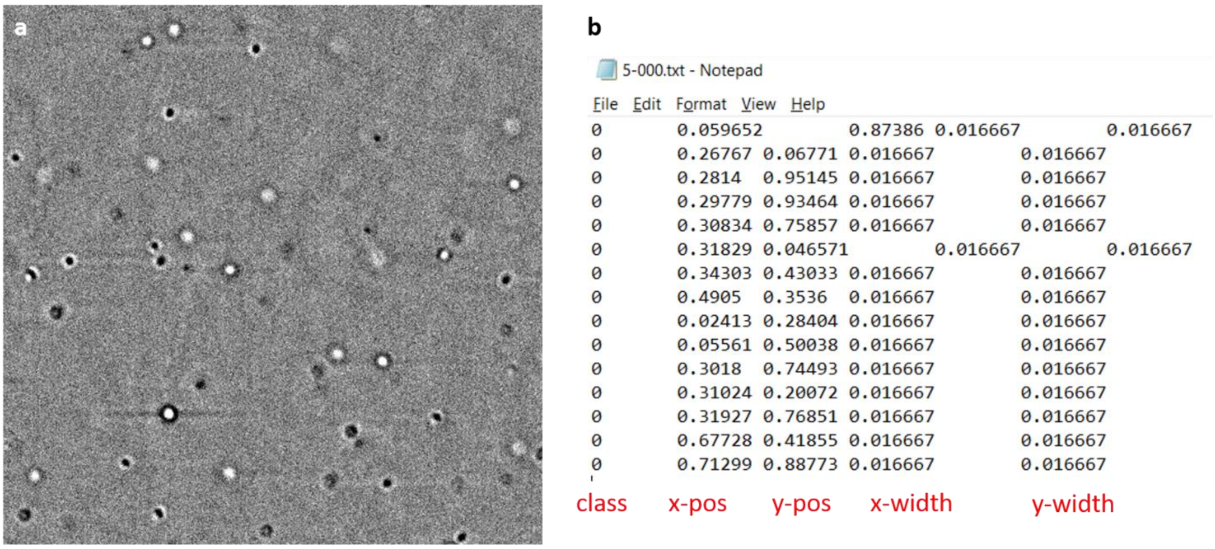

```
0       0.059652        0.87386 0.016667        0.016667
0       0.26767 0.06771 0.016667        0.016667
0       0.2814  0.95145 0.016667        0.016667
0       0.29779 0.93464 0.016667        0.016667
0       0.30834 0.75857 0.016667        0.016667
0       0.31829 0.046571        0.016667        0.016667
0       0.34303 0.43033 0.016667        0.016667
0       0.4905  0.3536  0.016667        0.016667
0       0.02413 0.28404 0.016667        0.016667
0       0.05561 0.50038 0.016667        0.016667
0       0.3018  0.74493 0.016667        0.016667
0       0.31024 0.20072 0.016667        0.016667
0       0.31927 0.76851 0.016667        0.016667
0       0.67728 0.41855 0.016667        0.016667
0       0.71299 0.88773 0.016667        0.016667
```

Figure1: PSF training set. a shows the individual interferometric spots altering in shape of intensity depending on their axial position in the sample regarding the focus plane of the objective lens. b represents a screen capture of the label text file of the image of single spots presented in a. the label text file contains the class of the localized objects, x, y position and width and height of each object in the image.

In practice, in order to run the training process, some modifications to the usual configuration files have to be made depending on the training sets and number of classes. The training process can be quite slow usually and costly in terms of computation time (about days of training) when relying on standard CPU. Thereby, we performed the training process using **GPU facilities**, and we then have been able to reduce the training time to a few hours. Different parameters have to be taken into consideration to optimize the performance of the detection of PSF spots. In brief, the learning should present a decrease in the estimated error for an increasing time of training. The error estimation will define the precision of the localization. However, increasing the training process can induce an overtraining problem that limits the ability of the algorithm to detect unseen images and generalize for unseen images.

PSF detection and tracking:

Once we finish with the training process, we retrieve the weights file that has been optimized during the training process and employ this weight file to perform the detection of unseen images of single interferometric PSFs.

Different ways of implementing the detection algorithm can be used. In our case, we employed Deep sort to track the movement of the position of the particles between consecutive frames. It consists of a Simple Online and Real-time Tracking with a Deep Association Metric **(Deep SORT),** a high-performance multiple object tracking based on YOLO detection [Simple online and real-time tracking with a deep association metric]. This framework has proved its robustness as well as its efficiency in different applications such as detection such tracking vehicles, pedestrians and many others. This framework has been used for tracking multiple objects of different classes simultaneously. Different tracking approaches can be exploited using this framework, the key point of such an approach is its robustness which can be advantageous for single particles tracking, especially that the nanoparticles can go in/ out the volume of detection repeatedly.

In practice, Deep-sort is an easy-to-use framework in which simple modifications of the configuration files and using the trained optimized weights are only needed to perform single-particle tracking of virus particles in water. The main challenge with such detection is the computation cost, as mentioned first, our aim is to reach real-time single particles tracking microscopy. Using a standard computer using CPU only, we have been able to detect particles with a relatively low tracking speed of about 0.5 frames/second for a field of view of 40um*40um. However, the detection speed can be increased by a factor of 40 by using basic GPU facilities. By a visual inspection, we can see that the trajectories are consistent for the detected single particles as can be seen in **fig2**.

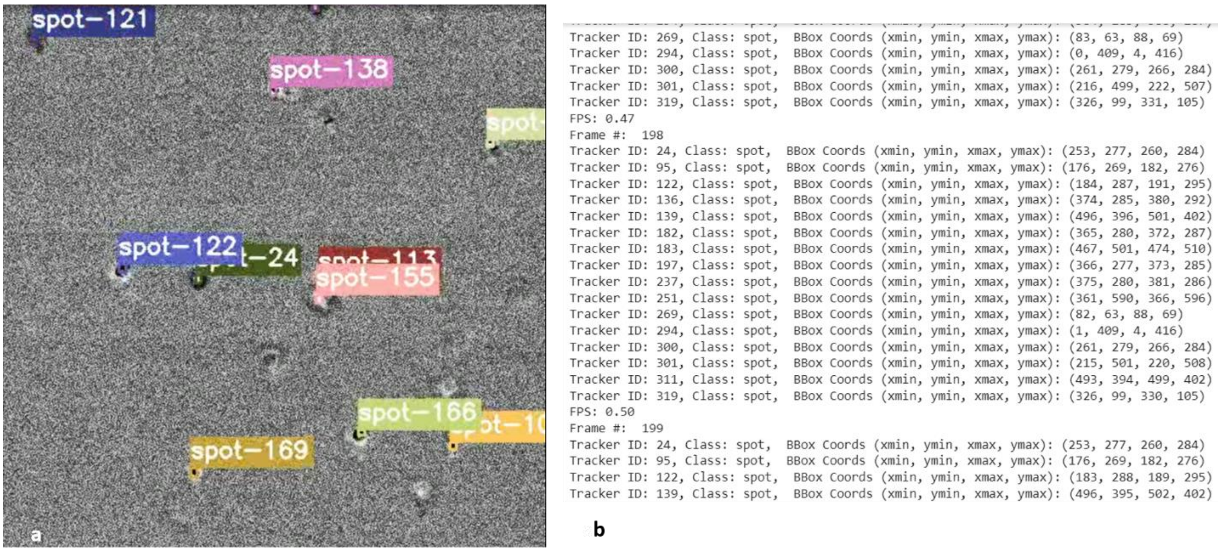

```
Tracker ID: 269, Class: spot,  BBox Coords (xmin, ymin, xmax, ymax): (83, 63, 88, 69)
Tracker ID: 294, Class: spot,  BBox Coords (xmin, ymin, xmax, ymax): (0, 409, 4, 416)
Tracker ID: 300, Class: spot,  BBox Coords (xmin, ymin, xmax, ymax): (261, 279, 266, 284)
Tracker ID: 301, Class: spot,  BBox Coords (xmin, ymin, xmax, ymax): (216, 499, 222, 507)
Tracker ID: 319, Class: spot,  BBox Coords (xmin, ymin, xmax, ymax): (326, 99, 331, 105)
FPS: 0.47
Frame #:  198
Tracker ID: 24, Class: spot,  BBox Coords (xmin, ymin, xmax, ymax): (253, 277, 260, 284)
Tracker ID: 95, Class: spot,  BBox Coords (xmin, ymin, xmax, ymax): (176, 269, 182, 276)
Tracker ID: 122, Class: spot,  BBox Coords (xmin, ymin, xmax, ymax): (184, 287, 191, 295)
Tracker ID: 136, Class: spot,  BBox Coords (xmin, ymin, xmax, ymax): (374, 285, 380, 292)
Tracker ID: 139, Class: spot,  BBox Coords (xmin, ymin, xmax, ymax): (496, 396, 501, 402)
Tracker ID: 182, Class: spot,  BBox Coords (xmin, ymin, xmax, ymax): (365, 280, 372, 287)
Tracker ID: 183, Class: spot,  BBox Coords (xmin, ymin, xmax, ymax): (467, 501, 474, 510)
Tracker ID: 197, Class: spot,  BBox Coords (xmin, ymin, xmax, ymax): (366, 277, 373, 285)
Tracker ID: 237, Class: spot,  BBox Coords (xmin, ymin, xmax, ymax): (375, 280, 381, 286)
Tracker ID: 251, Class: spot,  BBox Coords (xmin, ymin, xmax, ymax): (361, 590, 366, 596)
Tracker ID: 269, Class: spot,  BBox Coords (xmin, ymin, xmax, ymax): (82, 63, 88, 69)
Tracker ID: 294, Class: spot,  BBox Coords (xmin, ymin, xmax, ymax): (1, 409, 4, 416)
Tracker ID: 300, Class: spot,  BBox Coords (xmin, ymin, xmax, ymax): (261, 279, 266, 284)
Tracker ID: 301, Class: spot,  BBox Coords (xmin, ymin, xmax, ymax): (215, 501, 220, 508)
Tracker ID: 311, Class: spot,  BBox Coords (xmin, ymin, xmax, ymax): (493, 394, 499, 402)
Tracker ID: 319, Class: spot,  BBox Coords (xmin, ymin, xmax, ymax): (326, 99, 330, 105)
FPS: 0.50
Frame #:  199
Tracker ID: 24, Class: spot,  BBox Coords (xmin, ymin, xmax, ymax): (253, 277, 260, 284)
Tracker ID: 95, Class: spot,  BBox Coords (xmin, ymin, xmax, ymax): (176, 269, 182, 276)
Tracker ID: 122, Class: spot,  BBox Coords (xmin, ymin, xmax, ymax): (183, 288, 189, 295)
Tracker ID: 139, Class: spot,  BBox Coords (xmin, ymin, xmax, ymax): (496, 395, 502, 402)
```

Figure2: Deep sort Single Particle Tracking. **a** represents an image of the detected trajectories with their corresponding ID. The tracking relies on the use of the trained PSF spots as shown in fig1. **b** shows a screen capture of the text output of the position of the detected spots as well as the width and height of the tracked spots, to note that the tracking process can be done at a speed of 0.5fps using CPU only.

The use of GPU facilities using Google COLAB:

As mentioned in the previous paragraphs, the use of GPU can be efficient for faster training, detection, localization, and tracking. All these different steps have been performed on a standard laptop using free **GPU access provided by Google.** Google Colab provides limited access to GPU facilities. This platform allows to execution of python codes in a like Jupiter notebook format which is user-friendly and easy to implement on a standard computer.

As shown in **fig 2**, for the proof of concept, we have been able to detect, localize and track single PSF particles in real-time for a field of view of 25*25um2 with a tracking speed about 30fps. Although we have been able to perform single-particle tracking a huge margin of optimization can be considered for a real time detection. Such as optimization of the training process and the tracking algorithm used by Deep-sort. The tracking speed depends mainly on the performance of the GPU in use and also on the Deep sort implementation for YOLO detection. Different approaches can be considered depending on the needed accuracy and speed in use. Many advantages are interesting in the implementation of the deep learning approach to perform single particle tracking microscopy. It allows tracking particles in real-time and does not require a high-performance computer and also is quite versatile in which you can track different types of different objects using “any” device that can have internet connection. Thus, this implementation is particularly interesting for heterogeneous samples and mostly for real-time 3D localization in a later stage.

Last, the implementation of deep learning SPT was a proof of concept of the ability to do single particle tracking microscopy in a fast and robust manner. Although that we have encouraging preliminary results. The first implementation of this approach has been done at the beginning of my second year of Ph.D. and the detection, localization, and tracking algorithms have improved massively in terms of faster and more robust algorithms, such as YOLOR [arXiv preprint arXiv:2105.04206]. The improvement the detection and tracking algorithms have reached an improvement of 2 orders of magnitude in terms of speed with much better accuracy (about 3 folds). There is still plenty of room of improvement but, in this work we stopped at the point of the proof of concept of this approach.

RÉSUMÉ

Le manuscrit de thèse concerne certains aspects de la microscopie optique sans marqueur de petits objets diffusant la lumière tels que des virus ou des structures subcellulaires. La géométrie adoptée est celle de la transmission plein champ. Il utilise l'interférence entre les ondes incidentes et diffusées pour amplifier les signaux faibles.

À l'aide d'algorithmes de suivi de particules uniques, nous avons détecté des virus et des nanoparticules diélectriques de SiO2 aussi petites que 50 nm en utilisant une lumière incohérente. En combinant le signal interférométrique avec la diffusion brownienne propriétés de particules individuelles, nous avons pu suivre la modification de la diffusivité des nanoparticules à l'échelle de la minute. Ensuite, une cascade de réactions se produit, conduisant à la création d'agrégats. Cette approche permet d'estimer une constante d'association d'équilibre attribuée à l'affinité des anticorps.

Le signal interférométrique était insensible aux aberrations sphériques induites par le décalage d'indice de réfraction lors de l'utilisation d'objectifs à haute ouverture numérique à immersion dans l'huile. Cependant, les données expérimentales montrent que la NA de l'ouverture numérique élevée n'est pas pleinement utilisée. Nous avons expliqué ce phénomène à l'aide d'un modèle théorique simple et de simulations en champ proche pour comprendre le déphasage de Gouy et l'impact de la défocalisation près du foyer. De plus, pour détecter des virus plus petits, nous avons utilisé un miroir à membrane déformable à haute fréquence (supérieure à 1 MHz) et une fibre optique carrée à homogénéiser pour obtenir un éclairage à champ large sans chatoiement. Cette approche nous a permis d'atténuer le faisceau de référence pour détecter de petits virus de (MS2, AAV) de (27,20)nm.

Enfin, nous explorons une nouvelle méthode prometteuse de microscopie interférométrique plein champ fonctionnant par transmission pour imager des objets solides ou semi-solides et révélant à la fois les structures des objets observés et la dynamique intracellulaire.

MOTS CLÉS

Détection de virus sans marquage, Interférométrie de diffusion, Suivi de particles uniques, Diffusion browni-enne, Diffusion brownienne, Tomographie et dynamique.

ABSTRACT

The thesis manuscript concerns some aspects of optical label-free microscopy of small light-scattering objects such as viruses or subcellular structures. The geometry adopted is that of full-field transmission. It utilizes the interference between the incident and scattered waves to amplify weak signals.

Using Single-particle tracking algorithms, we have detected viruses and dielectric nanoparticles of SiO2 as small as 50nm using incoherent light. By combining the interferometric signal with the Brownian diffusion properties of single particles, we have been able to track the modification of the diffusivity of nanoparticles on the scale of the minute. Then a cascade of reactions occurs, leading to the creation of aggregates. This approach allows estimating an equilibrium association constant attributed to the affinity of antibodies.

The interferometric signal was insensitive to spherical aberrations induced by the refractive index mismatch when using oil immersion high numerical aperture objectives. However, experimental data show that the NA of the high numerical aperture is not fully used. We explained this phenomenon using a simple theoretical model and near-field simulations to understand the Gouy phase shift and defocus impact near the focus. Furthermore, to detect smaller viruses, We used a high-frequency (higher than 1MHz) deformable membrane mirror and a square optical fiber to homogenize to obtain a speckle-free wide-field illumination. This approach allowed us to attenuate the reference beam to detect small viruses of (MS2, AAV) of (27,20)nm.

Finally, we explore a new promising method of full-field interferometric microscopy operating by transmission to image solid or semi-solid objects and revealing both the structures of the objects observed and the intracellular dynamics.

KEYWORDS

Label-free virus detection, Scattering interferometry, Single particle tracking, Brownian diffusion, Antibody affinity, Tomography and dynamics.